der Bundeswehr
Universität München

A contribution to methods of developing elastomeric aircraft door seals based on FEM analysis, Design of Experiments and Parametric Optimisation

Bruno Franke Goularte

Vollständiger Abdruck der von der Fakultät für Luft- und Raumfahrttechnik der Universität der Bundeswehr München zur Erlangung des akademischen Grades eines

Doktor-Ingenieurs (Dr.-Ing.)

genehmigten Dissertation

Gutachter: Univ.-Prof. Dr.-Ing. habil. Alexander Lion
Zweitgutachter: Univ.-Prof. Dr.-Ing. habil. Stéphane Lejeunes

Die Dissertation wurde am 19.01.2023 bei der Universität der Bundeswehr München eingereicht und durch die Fakultät für Luft- und Raumfahrttechnik am 26.07.2023 angenommen. Die mündliche Prüfung fand am 08.08.2023 statt.

Acknowledgements

I would first like to thank my family and friends who supported me throughout this academic journey. There are many names, so I must start with my parents: Ailton José dos Santos Goularte and Iria Alvina Franke Goularte. Thank you for giving me the initial conditions to pursue my dreams. During all this time, it is impossible not to mention or define someone who has been more important than my wife and friend Lays Guimarães Jaeger. We met in the first years that I was studying mechanical engineering in Brazil. Even after the exchange period in France, she accompanied and helped me to pursue our dreams in Germany. Without her I would never have completed on my own this work.

As for the academic foundation required for the existence of this doctoral work, I would like to make some special dedications. At the Federal University of Rio Grande do Sul (UFRGS) where everything started, I am grateful to the Applied Mechanics Group (GMAp) and to professor Herbert M. Gomes for initiating me in the scientific career. Together with École Centrale de Marseille (ECM) and CNRS, I would like to thank the Laboratory of Mechanics and Acoustics (LMA) and professor Stéphane Lejeunes who gave me the opportunity to discover the world of Continuum Mechanics. This was my first contact with aerospace engineering, which opened doors for me to work in civil aviation, structural analysis and in the academic field. More recently, I have a strong appreciation for the Bundeswehr University München (UniBw) and the Institute of Mechanics (LRT4), whose professors Alexender Lion and Micael Johlitz gave me the dream opportunity to do my PhD project in partnership with AIRBUS.

I believe that this work deserves a special credit to people who were directly or indirectly connected to my work either in presence or by homeoffice. Vivianne and Thomas Kaspar were essential to keep me cheerful in my days locked in the lab, either talking in Portuguese or learning Bavarian. Markus Adler and Hanno Niemann were the ones who asked me the right questions when I thought I had all the answers about seals. Design of Experiments was a strategy that emerged in the last year to find out the causes thanks to his commitment to support me on the AIRBUS side. Last but not least, I would like to thank André and Joe (Vinicius) for making this work take longer than it normally would to be finished. Many barbecues at the Isar river in Munich and a lot procrastination because of these two gentlemen.

Thanks, merci, danke and obrigado!

Bremen, in August 2023 Bruno Franke Goularte

Kurzfassung

Elastomerwerkstoffe sind heute in technischen Anwendungen fest etabliert und werden u.a. für Lager, Schläuche, Reifen und Dichtungen verwendet. Geometrisch komplexe Profile aus verschiedenen faserverstärkten und thermisch stabilen Elastomeren werden mit Hilfe anderer Polymerwerkstoffe für die Herstellung von Flugzeugtürdichtungen verwendet. Ihr Zweck ist es, die Innenkabine des Flugzeugs gegen die Witterungsbedingungen abzudichten, wobei die Dichtungswirkung möglichst unbeeinflusst von äußeren Störeinflüssen sein soll. Je nach Flughöhe unterscheiden sich der Differenzdruck im Flugzeugrumpf und die Temperatur von Flug- zu Bodenbedingungen. Diese Unterschiede beeinflussen die lokalen Beanspruchungen der Türdichtungen und verändern damit die erforderlichen speziellen Konstruktionslösungen. Das Hauptziel dieser Arbeit ist es, eine geeignete Methode zur Quantifizierung und zum Verständnis der Variablen hinter der Dichtungsleistung für die Designentwicklung mit Hilfe kommerzieller CAE-Tools bereitzustellen.

Basierend auf dem Großdehnungsformalismus der Kontinuumsmechanik wird die Charakterisierung der Materialeigenschaften als erster Schritt verwendet, um das Verhalten einer Elastomerdichtung auf physikalisch konsistente Weise zu betrachten. Da Elastomere und Polymere zur Klasse der thermo-viskoelastischen Materialien gehören, können auch Änderungen in der Kontaktspannungsverteilung aufgrund von Relaxation auftreten. Indem das Einsatzprofil eines Langstreckenflugzeugs vom Boden bis zu den Flugbedingungen festgelegt wird, werden die Analyseschritte in einer Abfolge von statischen, dynamischen und temperaturbeeinflussten Lösungen aufgebaut. Zu Simulationszwecken werden 2D-Modelle nach Extrapolationstechniken verwendet, um eine repräsentative Maschengröße mit der FEM anzunehmen. Ausgehend von einem konzeptionellen aufblasbaren Dichtungsentwurf, der für Passagier- und Frachttüren verwendet wird, werden die Simulationen in einer virtuellen Umgebung für Berechnungsexperimente parametrisiert. Trotz der fehlenden Validierung der Analysemethoden auf Komponentenebene ermöglicht die Versuchsplanung (Design of Experiments, DOE) die Bewertung der Eingaben, die mit den Leistungsindikatoren der Dichtung in Bezug auf Leckage, Kollaps, Kraft, Sicherheitsfaktoren und Restverschiebung korreliert sind. Diese Indikatoren hängen von den Modellergebnissen wie Spannung, Verschiebung und Anpressdruck ab, die auf der Grundlage der Wahl des "besten" Designs durch parametrische Optimierung geändert werden.

Die Ergebnisse zeigen, dass es mit zwei Algorithmen möglich ist, aus leicht unterschiedlichen Entwurfskandidaten oder -varianten die optimale Lösung zu finden: NSGA-II und LSRGR. Eine Zielfunktion, die den Luftaustritt reduziert und gle-

ichzeitig die Reaktionskraft beim Schließen der Tür minimiert, wird durch drei kritische Belastungsbedingungen abgedeckt, die durch relative Verschiebungen des Schließers bestimmt werden. Leistungsvergleiche werden schließlich mit der DOE-Reanalyse von 500 Lastfällen berechnet, die ursprünglich durch das Optimierte Latin Hypercube Sampling (LHS) von 11 Eingaben erzeugt wurden.

Abstract

Elastomer materials are now firmly established in technical applications and are used, among others, for bearings, hoses, tyres, and seals. Geometrically complex profiles comprised of various fibre-reinforced and thermally stable elastomers are used with the aid of other polymer materials for the manufacture of aircraft door seals. Their purpose is to seal the interior cabin of the aircraft against the atmospheric conditions, whereby the sealing effect should be as unaffected as possible by external disturbing influences. Depending on the flight altitude, the differential pressure in the fuselage of the aircraft and the temperature are distinct from flight to ground conditions. These differences influence the local stresses of the door seals and thus modify the required special design solutions. The main purpose of this work is to provide a suitable methodology to quantify and understand the variables behind the seal performance for design development with the help of the commercial CAE tools.

Based on the large strain formalism of continuum mechanics, the characterization of the material properties is used as the initial step to consider the behaviour of an elastomeric seal in a physically consistent manner. Since elastomers and polymers belong to the class of thermo-viscoelastic materials, changes in the contact stress distribution may also occur due to relaxation. By establishing the mission profile of a long-range aircraft from ground to flight conditions, the analysis steps are built in a sequence of static, dynamic, and temperature-influenced solutions. For simulation purposes, 2D models are used after extrapolation techniques to assume a representative mesh size using the FEM. From a conceptual inflatable seal design used for passenger and cargo doors, the simulations are parametrised in a virtual environment for computational experiments. Despite the lack of validation of the analysis methods on a component level, Design of Experiments (DOE) provides the assessment of the inputs that are correlated to the seal performance indicators related to leakage, collapse, force, safety factors, and residual displacement. These indicators depend on model outputs such as stress, displacement, and contact pressure which are modified based on the choice of the 'best' design through Parametric Optimisation techniques.

The results show that it is possible to extract the optimal solution from slightly different design candidates or variants by combining the capabilities of two algorithms: NSGA-II and LSRGR. An objective function that reduces air leakage, while minimising the reaction force when the door closes, is covered by three critical loading conditions governed by relative displacements of the striker. Performance comparisons are ultimately computed with the DOE re-analysis of 500 load cases that were initially generated by the optimal Latin Hypercube Sampling (LHS) of 11 inputs.

Contents

1. Introduction **1**
- 1.1. Background . . . 2
- 1.2. Objectives and structure . . . 4
- 1.3. State of the art . . . 7

2. Fundamentals **9**
- 2.1. Continuum mechanics . . . 9
  - 2.1.1. Kinematics . . . 10
  - 2.1.2. Strain measures . . . 11
  - 2.1.3. Rate of deformation . . . 13
  - 2.1.4. Stress tensors . . . 15
- 2.2. Balance equations . . . 16
  - 2.2.1. Mass balance . . . 16
  - 2.2.2. Linear momentum balance . . . 17
  - 2.2.3. Angular momentum balance . . . 18
  - 2.2.4. Energy balance (1^{st} law of thermodynamics) . . . 18
  - 2.2.5. Entropy balance (2^{nd} law of thermodynamics) . . . 19
- 2.3. Materials theory . . . 21
  - 2.3.1. Isotropic hyperelasticity . . . 23
  - 2.3.2. Finite linear viscoelasticity . . . 27
- 2.4. Introduction to optimisation . . . 34
  - 2.4.1. Gradient-based methods . . . 36
  - 2.4.2. Design of Experiments (DOE) . . . 37
  - 2.4.3. Genetic Algorithms (GA) . . . 39

3. Material investigations **40**
- 3.1. Uniaxial coupon tests . . . 42
  - 3.1.1. Quasi-static loadings . . . 43
  - 3.1.2. Relaxation process . . . 48
- 3.2. Modelling assumptions . . . 50
  - 3.2.1. About the seal hardness . . . 50
  - 3.2.2. The influence of temperature . . . 52

4. Seal FEM analysis **53**
4.1. Premises of the model . . . 54
4.1.1. Boundary conditions . . . 55
4.1.2. Analysis steps . . . 58
4.2. Element suitability . . . 61
4.3. Seal performance . . . 66
4.3.1. Reaction force . . . 66
4.3.2. Leakage criterion . . . 68
4.3.3. Seal collapse . . . 71
4.3.4. Safety factor . . . 72
4.3.5. Residual displacement . . . 73
4.4. Summary of seal performance analysis . . . 74

5. Design of Experiments **75**
5.1. Sampling . . . 77
5.2. DOE analysis . . . 80
5.2.1. Data correlation . . . 81
5.2.2. Interpretation of the results . . . 84
5.3. Outcomes . . . 85
5.3.1. Load case 1: R_x nominal max compression . . . 86
5.3.2. Load case 2: U_x positive min compression . . . 86
5.3.3. Load case 3: M_x negative min compression . . . 86

6. Parametric Optimisation **87**
6.1. Non-dominated Sorting Genetic Algorithm . . . 89
6.1.1. Optimisation rounds . . . 90
6.1.2. Design candidates . . . 93
6.2. Large-Scale Generalised Reduced Gradient . . . 94
6.2.1. Design refinement . . . 95
6.2.2. Design comparisons . . . 96
6.3. 'Best' seal design . . . 98
6.3.1. Design discussion . . . 100
6.3.2. Method considerations . . . 103

7. Summary and outlook **105**

List of Figures **108**

List of Tables **110**

References **111**

A. Appendix 1 **120**

Abbreviations and notations

The following list presents the abbreviations and notations used for tensor algebra:

Abbreviations

CAE	Computer-aided engineering
FEM	Finite Element Method
CAD	Computer-Aided Design
DOE	Design of Experiments
OLHT	Optimised Latin Hypercube Technique
OPT	Parametric Optimisation
FPP	Fluid Pressure Penetration
MSE	Mean Squared Erros
GCI	Grid Convergence Index
OWD	Over Wing Door
PAX	Passenger Door
CARGO	Compartment Door
UMAT	User-defined Material
DLOAD	User-defined Distributed Load
WLF	Williams-Landel-Ferry
CEL	Coupled Eler Lagrangian
CFD	Computational Fluid Dynamics
FAA	Federal Aviation Administration
DIN	Deutsche Institut für Normung
CPU	Central Processing Unit
GPGPU	General Purpose Graphics Processing Unit
NSGA-II	Non-dominated Sorting Genetic Algorithm
LSGRG	Large Scale Generalised Reduced Gradient
LHS	Latin Hypercube Sampling

General notation for tensors

$a, b, ...$	Zero order tensor (scalar)
$\mathbf{a}, \mathbf{b}, ...$	Tensors 1st order (vector)
$\mathbf{A}, \mathbf{B}$,...	Tensors 2nd order (dyad)

Special tensor operations

$\mathrm{Grad}(\bullet) = \frac{\partial(\bullet)}{\partial \mathbf{X}}$	Gradient with respect to the reference configuration
$\mathrm{Div}(\bullet) = \mathrm{Grad}(\bullet) : \mathbf{I}$	Divergence with respect to the reference configuration
$\mathrm{grad}(\bullet) = \frac{\partial(\bullet)}{\partial \mathbf{x}}$	Gradient with respect to the current configuration
$\mathrm{div}(\bullet) = \mathrm{grad}(\bullet) : \mathbf{I}$	Divergence with respect to the current configuration
$\mathbf{A} \cdot \mathbf{B} = A_{ij} B_{jk}$	Simple scalar product between two 2nd order tensors
$\mathbf{A} : \mathbf{B} = A_{ij} B_{ij}$	Twofold scalar product between 2nd order two tensors
$(\mathbf{A} \cdot \mathbf{B})^T = \mathbf{B}^T \cdot \mathbf{A}^T$	Transpose of a tensor product
$(\mathbf{A} \cdot \mathbf{B})^{-1} = \mathbf{B}^{-1} \cdot \mathbf{A}^{-1}$	Inverse of a tensor product

Special continuum mechanical quantities

$\mathbf{I} = \delta_{ij}\, \mathbf{e_i} \otimes \mathbf{e_j}$	Identity tensor 2nd order
$\mathbf{x}$	Position vector in the current configuration
$\mathbf{X}$	Position vector in the reference configuration
$\mathrm{d}\mathbf{a}$	Area element in the current configuration
$\mathrm{d}\mathbf{A}$	Area element in the reference configuration
$\mathrm{d}v$	Volume element in the current configuration
$\mathrm{d}V$	Volume element in the reference configuration
$\mathbf{F}$	Deformation gradient
$\mathbf{R}$	Rotation tensor
$\mathbf{U}$	Left tensor of pure deformation
$\mathbf{V}$	Right tensor of pure deformation
$\mathbf{B}$	Left Cauchy-Green tensor
$\mathbf{C}$	Right Cauchy-Green tensor

$\mathbf{E}$	Green-Lagrangian deformation tensor
$\mathbf{A}$	Euler-Almansi deformation tensor
$\mathbf{a}$	Finger strain tensor
$\mathbf{e}$	Piola strain tensor
$\boldsymbol{\varepsilon}$	Infinitesimal engineering strain
$\mathbf{v}$	Spatial velocity field
$\mathbf{L}$	Spatial velocity tensor
$\mathbf{D}$	Spatial deformation velocity tensor or rate of deformation
$\mathbf{W}$	Spin tensor
$\dot{\mathbf{E}}$	Rate of the Green-Lagrangian deformation tensor
$\mathbf{t}$	Traction force vector in the current configuration
$\mathbf{T}$	Traction force vector in the reference configuration
$\boldsymbol{\sigma}$	Cauchy stress tensor
$\boldsymbol{\tau}$	Kirchhoff stress tensor
$\mathbf{P}$	First Piola-Kirchoff tensor
$\mathbf{S}$	Second Piola-Kirchoff tensor
$\tilde{\mathbf{t}}$	Convected stress tensor
J	Jacobian Determinant
$\psi(\mathbf{x}, t)$	Phyisical quantity in the master balance
ψ	Helmholtz free energy per unit mass
ρ and ρ_0	Material density
$\varphi(\mathbf{x}, t)$	Flux term in the master balance
$\sigma(\mathbf{x}, t)$	Storage term in the master balance
$\hat{\psi}(\mathbf{x}, t)$	Production term in the master balance
$\mathcal{P}_{ext}$	Power of external forces
$\mathcal{K}$	Kinetic energy
$\mathcal{P}_{int}$	Internal stress power
$\mathcal{E}$	Total internal energy
$\mathcal{Q}$	Thermal power
$\mathcal{S}$	System entropy
$\mathcal{T}_{ext}$	Heat exchanged by the system

e	Internal energy per unit mass
r	Supply of energy per unit mass
θ	Thermodynamic temperature
η	Entropy per unit mass
$\mathcal{A}_i$ and α_i	Internal variables
$\mathbf{q}$	Heat flux vector in current configuration
$\mathbf{Q}$	Heat flux vector in reference configuration
λ	Stretch
p, p_H or p_H^*	hydrostatic pressure
σ_{eq} and σ_∞	Equilibrium stress
σ_{ov}	Overstress

Material and model parameters

C_{ij} and D_i	Parameters of the generalised Mooney-Rivlin model
$\hat{\eta}$	Dynamic viscosity
$\hat{E}$	Young's modulus
μ_A and μ_B	Shear moduli from Model A and B
τ_A and τ_B	Relaxation times from Model A and B
G	Shear modulus
G_0	Instantaneous modulus

FEM analysis inputs

C_{10} , C_{02} and D_1	Hyperelastic coefficients (n=2)	[MPa]
g_i	Normalised shear modulus	[-]
τ_i	Relaxation times	[sec.]
C_1 and C_2	WLF coefficients	[-]
θ_0	Reference temperature	[C°]
ρ_0	Material density	[tom/mm^3]
k	Material conductivity	[W/(m.K)]
SH_A	Shore hardness A	[-]

μ	Friction coefficient	[-]
S_1, S_2 and S_3	Slave seal surfaces	[-]
M_1	Master striker surface	[-]
U_x and U_y	Relative striker displacement	[mm]
R_x and R_y	Rigging tolerances	[mm]
P_x and P_y	Pressure displacements	[mm]
M_x and M_y	Manoeuvre displacements	[mm]
C_y	Closure striker displacement	[mm]
T_1, T_2 and T_3	Flight mission temperatures	[C°]
ΔP	Differential pressure	[MPa]

FEM analysis outputs

CPRESS	Contact pressure	[MPa]
PPRESS	Fluid pressure	[MPa]
RF	Reaction force	[N/m]
S	True stress	[MPa]
LE	Logarithmic strain	[-]
U	Final displacement	[mm]
Force	Linear force	[daN/m]
Leakage	Leakage index	[-]
Collapse	Collapse index	[-]
Residual	Residual displacement	[mm]

1. Introduction

Door seals are components found in civil aircrafts to maintain the air pressure inside the cabin under breathable human conditions. When commercial planes started being used for longer distances during the late 1930s, flying at higher altitudes was a solution to reduce the drag at a high cruising speed, while saving fuel consumption in a rarefied atmosphere. On the other hand, cabin pressurisation through bleed-air-conditioned systems was necessary to ensure passenger and crew comfort, which was accomplished by trading part of the energy generated by the engines. Even though these systems are increasingly being replaced by electrically powered compressors in modern jets, door seals are still important to fill the gaps between the fuselage cut-outs and the door skin to avoid air leakage, noise, and cabin depressurisation during flight. The variety of doors of commercial planes is the initial challenge to developing efficient seal designs. Generally, doors are used for different operations, such as passenger boarding, disembarking, baggage loading and unloading, routine inspections, and emergency evacuation. However, fuselage cut-outs are considered undesirable from the structural point of view once they modify the loading path through the stiffened panels. Even though the doors' surroundings are reinforced to withstand the cabin differential pressure and manoeuvres from flight loading events, relative displacements between the seal and the contact interface should be considered to effectively size the seal. Door rigging tolerances may have an impact on the seal's compression given the size of a seal cross-section. Nevertheless, material plays a central role in designing and requires modern modelling techniques to address the challenges involved.

Ideally, sealing components are designed from rubber-like materials with fibre reinforcements to harness the cabin pressure in their favour and prevent air leakage. Due to the stable mechanical characteristics under large strain and operating temperatures, a silicone matrix is preferably chosen by the seal manufacturers. Technically called elastomers, these polymers are well suited for seal solutions due to the nearly incompressible nature of rubber that provides sufficient contact pressure under compressive loads. Since silicone belongs to the class of thermoviscoelastic materials, contact pressure distributions may change through creep and relaxation processes, which are influenced by temperature. Complex profiles are usually created with injection moulding techniques according to the production experience of manufacturers. Despite not being significant structural items, seal system issues may impair aircraft operations, thereby adding costs and incurring project delays. Thus, computational aided tools are envisaged to support seal development by integrating the Finite Element Method (FEM) with the Design of Experiments (DOE) and Parametric Optimisation.

1.1. Background

In the development of a commercial aircraft, the door seals must be compliant with the requirements of other adjacent structures concerning airworthiness. The specification of an appropriate door mechanism for the right cut-out size is the foremost priority for the fuselage. Subsequently, the door and its surrounding components must be sized under limit loads from the structural analysis. Once there is a consensus on the design of the door structures, the seal development concept can be started. From this point, it is possible to gauge the minimum number of geometric features that the door seal must exhibit against the relative displacements between the fuselage and the door skin. It is up to the seal developers to develop a design that is in accordance with the door kinematics which guarantees minimum air leakage while remaining stable during flight. Overall, seals are devices used to prevent or limit the leakage of fluids, often under high differential pressure. An ideal door seal system should be as static as possible, which is often impractical since the aircraft has an elastic body. Due to the structural loads that the aircraft is subjected to as a result of manoeuvres combined with the cabin pressure, the fuselage deform in the longitudinal and circumferential directions. Figure 1.1 illustrates the running loads distributed along the aircraft, causing relative motions on the door surroundings.

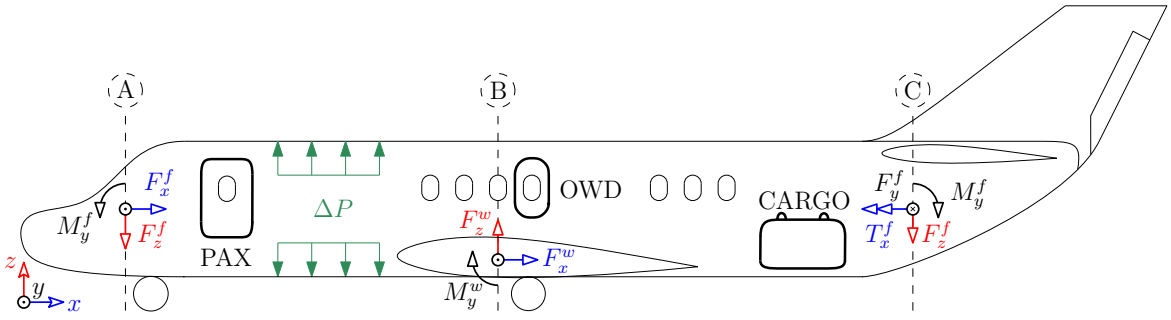

Figure 1.1. – Running loads of an aircraft.

The cabin differential pressure (ΔP) is assumed to be homogeneously distributed along the pressurised sections of the fuselage. However, most of the structural loads arising from flight and ground events are not equally distributed over the wing and fuselage stations, e.g. in the A, B, and C sections. In addition, the size of each door, such as the Over Wing Door (OWD), Passenger Door (PAX), and Cargo Compartment (CARGO), requires different sealing interface solutions. Any clearances between mating surfaces are susceptible to letting the fluid molecules follow the pressure gradient and air can pass through the open contact boundaries originating from the leakage. This issue may be triggered during flight manoeuvres if the seal stability is not maintained. In critical scenarios, higher air flow can gradually evolve from aerodynamic noise to cabin depressurisation. Since seal systems do not have redundancies, meaning that there is no secondary seal to cover possible failures, robust solutions are necessary.

According to the required design space and the limit loadings of door closure, a lip seal or a hollow design is typically considered in consonance with the door kinematics and the rigid striker interface, as illustrated by the cross-sections in Figure 1.2. Each design philosophy has its advantages and disadvantages, depending on the specific door applications. Although lip designs are simpler to manufacture they tend to deliver higher compressive reaction forces to the same seal length compared to hollow solutions. Lip seals are commonly used for smaller cut-outs, e.g. OWD, that are mostly not in operation. Hollow seal designs, on the other hand, are used when door cut-outs are wider, e.g. PAX and CARGO, and are frequently manipulated by the crew. By adding vent-holes to the seal wall, the air pumped inside the cabin is also used to inflate the cavity of the hollow. Furthermore, inflatable seals cover larger design spaces to compensate for the relative displacements from the striker, while reacting with lower forces during operations.

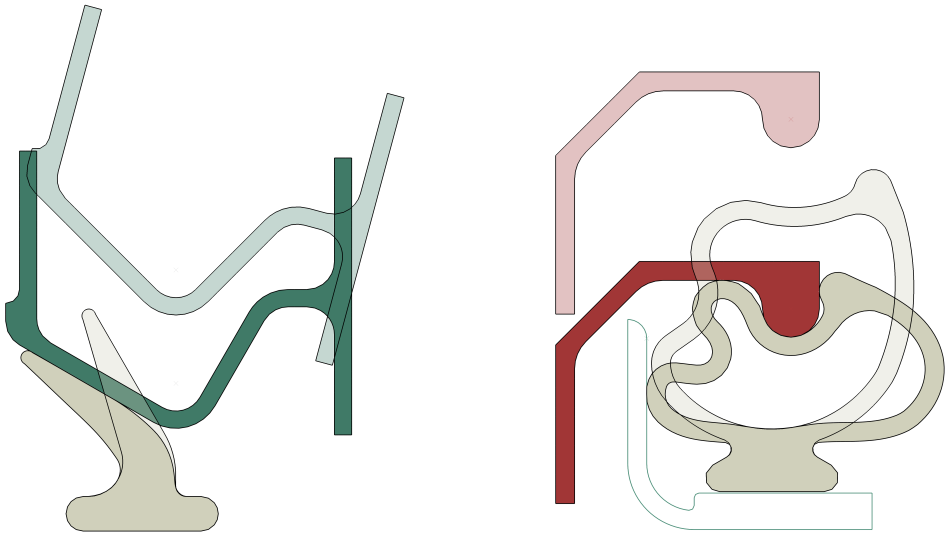

Figure 1.2. – Seal and striker design philosophies: lip (left) and hollow (right).

Although the cabin pressure load may be equally distributed along the fuselage stations, it is not symmetrical for the sealing cross-section. When the contact forces are not high enough to keep the seal stable, the profile is prone to slide under the striker, thereby culminating in structural instabilities. Both the rigid contact structures and the elastomeric seal should be compatible to avoid collapse. The seal should provide sufficient structural stiffness to prevent air leakage issues while respecting the operational loads. If the design is oversized, it may increase the resultant forces required by the closure and latching mechanism, thereby adding more weight to the aircraft door system. Doors that are manually operated by the crew must respect certain limitations due to daily operations and the minimum air leakage should be qualified in different environmental and rigging conditions for pressure acceptance.

Considering the short time frame to certify a civil aircraft, trial and error is often a pragmatic choice for door seal development. However, it can open an expensive path to unexpected failures of these systems. Generally, manufacturers support the seal conception through their prototyping technologies, e.g. injection moulding or extrusion, and mostly rely on the expertise they gained from previous concepts. Due to the lack of methods and validations, CAE tools are rarely explored in the industrial context of seals. Instead, ground qualification testing is rather considered, which is mandatory for verifying the pressurised compartment loads due to the cabin airtightness of large planes [1]. With the door in a latched position, these tests demonstrate whether the seal can keep the cabin pressure under allowable air leakage rate levels by adding safety factors from the aircraft release valve [2]. Since the test takes place under ground-controlled conditions for a couple of hours, the material response is not completely covered by the time interval of long flights. The atmospheric temperature and fuselage displacements of the flight spectra are not captured by full-scale tests, which are expensive to run even for the component level. Additionally, fleet deviations from rigging tolerances are not simply caught by controlled test conditions. Each seal can vary within the manufacturer's specifications from the hardness to the mechanical properties that can directly affect the seal's performance. From causing cabin noise to more serious hazards such as hypoxia and barotrauma, defective door seals have been highlighted by safety agencies as being the root cause of cabin depressurisation in airline operations [3, 4]. If the internal stress state of a seal changes the contact pressure between the seal and the fuselage interface is also affected, which can negatively influence the sealing effect. In an ideal door seal system, the contact distributions between the seal and door striker should be as independent as possible from all disturbing factors and only then can the seal operate optimally in every possible scenario.

1.2. Objectives and structure

The starting point for this research is to analyse, quantify, and understand the main influences that could affect the seal's performance. For this purpose, a characterisation of seal specimens is performed through uniaxial quasi-static and relaxation tests on a Zwick-Roell machine. The simplifying hypothesis is that elastomeric seals are isotropic and significantly influenced by their hyperelastic and viscoelastic response, in view of their dimensions, loadings, and temperature conditions. Although the seal samples extracted from actual parts have internal fabric layers and anti-friction coatings on the outside, these are assumed to be incorporated by the overall material response. Only the straight sections of the door seals are of interest, disregarding any geometric effects of radii cut-outs, which allows simplifications of the models in the plane-strain state. Hence, simple door seal interfaces are explored using commercial CAE tools. Under these assumptions, FEM simulations are quickly carried out for design conditions, thereby allowing for the exploration of sealing solutions.

The foundation provided by continuum mechanics is indispensable for modelling the non-linear behaviour of elastomers. Material modelling is substantiated by parameter identification from coupon tests within the strain range of interest for aircraft doors. The fading memory characteristic of the filled elastomers is considered to be governed by that of the silicone matrix, which is supported by the finite linear viscoelasticity theory. From the rheological model approach, the choice of a sufficient number of parallel Maxwell elements delivers the time-dependent behaviour observed in relaxation tests. By deriving the relationship between dual variables of strain and stress, the constitutive equations of a nearly incompressible material are obtained. Therefore, a fit between model predictions and the test results is conducted by comparing different material models. Both hyperelastic and viscoelastic parts are solved separately with uniaxial analytical solutions in Wolfram Mathematica by the optimisation algorithm *NMinimise*. Further influences arising from silicone hardness and temperature are examined based on the literature in Chapters 2 and 3.

Although the FEM is at the core of this work, user-defined material models (UMAT) are not addressed in this research. Instead, existing free energy models which are already implemented in ABAQUS [5] were envisaged to ensure simple analysis automatisation. Notably, the possibility of choosing between Mooney-Rivlin polynomial order models according to the need for representing hyperelastic behaviour stands out. Through a sufficient number of terms in a Prony series, the viscoelastic model is feasible for large-strain solutions. Additionally, the temperature-dependent shift factor of the Willams-Landel-Ferry (WLF) equation is also implemented, thereby relating the relaxation time to two material constants and the glass transition temperature. Nevertheless, FEM models must be in accordance with material theory and be satisfactorily discretised according to a mesh convergence criterion. For this, model output variables that describe the seal performance are extrapolated for the grid refinement criterion. The analysis of the seal performance obtained by FEM results is post-processed for certain outputs, i.e., nodal forces, element stresses, and displacements. Reaction loads per seal length, air leakage criteria based on contact pressures, and structural stability are explained in Chapter 4.

Chapter 5 presents a suitable methodology to investigate the controllable influencing variables on the seal performance outputs through DOE. In this case, the management tool ISIGHT is employed to manage a pre-defined number of FEM simulations for multiple variables sampled by the Optimised Latin Hypercube technique. In total, 11 variables including striker relative displacements and atmospheric temperature during different stages of flight, seal hardness, and the coefficient of friction are considered. By establishing a range of expected limits for the seal boundary conditions, the FEM models are parametrised to cover possible scenarios that can arise during aircraft missions. Spearman correlation tables are employed to highlight the input impacts with regard to the seal performance indicators and select critical loading conditions. Statistically grounded, the correlations that have the most significant effects on performance indicators are highlighted for design comparisons.

Among the functionalities of ISIGHT, an optimisation task is proposed to search for the best geometric features of the door seal design performed under the critical loading conditions found by DOE runs. With help of non-sorting genetic algorithms (GA), parametric design optimisation is conducted in an attempt to identify the factors that influence a seal's efficiency against leakage. This approach is elaborated since many design variables can be modified independently, which motivates a multi-objective optimisation subject to design constraints. After establishing the optimal solution, the concept and improved designs are compared based on the DOE load case selection. Figure 1.3 presents a diagram with all the tools, research points, and interactions culminating in a methodology to support the seal design development.

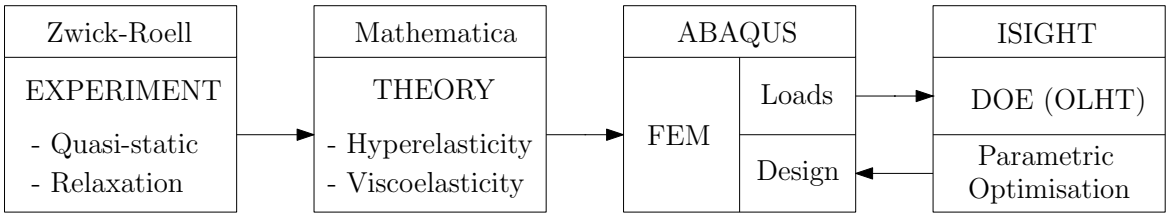

Figure 1.3. – Diagram with tools, analysis topics and working points.

Although this work lacks validation of the analysis method with the final test geometry, this contribution to the development of aircraft door seals may shed some light on the development of different elastomeric components that are subject to uncertain conditions. Numerical methods offer excellent accuracy to solve non-linear problems due to the increasing capacity and number of processors for calculations. It is understood, however, that the boundary problem of complex FEM models may make it hard to reach convergence within a reasonable analysis time. The simplification of the seal model as well as native solutions from the commercial software ABAQUS to represent boundary conditions, material behaviour, and analysis steps are explored within the capabilities offered by the tool. As previously mentioned regarding the development stages of an aircraft, it makes sense that interactive commercial solutions are in the foreground of product development. Despite not being relevant for door structures, elastomeric seals are complexly designed and should be mitigated in terms of failures by understanding and quantifying their mechanical response.

Therefore, the continuum mechanics formalism is the starting point to model the material behaviour in Chapter 2, providing hyperelasticity and linear viscoelasticity constitutive laws to explain the stress-strain relations of an elastomer. Reinforced silicone samples coming from seal applications of aircraft doors are used to fit the material models through mechanical experiments in quasi-static and relaxation tests. Model simplifications, such as material isotropy, dimensionality reduction, and temperature dependency, are justified to reduce the complexity of the non-linear simulations. The method of analysis for door seals is proposed for simple modelling representation to achieve quick computational experiments and further improve a concept design.

1.3. State of the art

Elastomers are recognised for their ability to store high levels of elastic deformation, making them an excellent candidate for sealing solutions. The flexible characteristic of natural rubber was first documented during the colonisation of South America by Europeans, who examined the possible uses of latex from *Haveea Brasiliensis* trees [6]. Subsequently, in the industrial era, different kinds of polymers were synthesised to improve the mechanical behaviour of rubber according to their chemical compounds. With the existence of new materials, standards have been set for the specific application of rubber qualification [7]. Silicone rubbers denoted by the letter Q, e.g. methyl silicone (MQ), vinyl methyl silicone (VMQ), phenyl methyl silicone (PMQ), and fluorosilicone (FVMQ), are slightly different at the molecular level, showing variations in their tensile strength and operating temperatures. In late 1938, with the Boeing 307 Stratoliner [8], the onset of pressurized commercial flights spurred the use of rubber's sealing capabilities. Given the rarefied atmosphere conditions at higher flight altitudes, silicone alternatives should maintain good resistance against contaminants, such as high concentrations of ozone and ice, and present a relatively low glass transition temperature [9, 10]. Withstanding flight cycles under differential pressure proved to be a major challenge for aluminium fuselage panels at that time, as recorded in the DH.106 Comet reports in 1953 which listed a total of 26 hull loss accidents, 13 of which were fatal [11]. In 1986, elastomers were implicated in a tragic milestone in aerospace history with the failure of an O-ring during the Challenger launch [12]. Hence, understanding the material response must be the foundation of a seal design.

Fundamentally, modelling the mechanical behaviour of an elastomeric seal requires a representative constitutive law based on the finite strain theory and a consistent thermodynamic framework [13, 14]. On a macroscopic scale, rubber is intrinsically influenced by its polymeric interactions on a molecular level. Many material models were developed to match the incompressible elastic behaviour of elastomers, whether by means of a phenomenological approach supported by continuum mechanics [15, 16] or by micromechanical formulation based on statistics [15, 16]. An overview from 1976 condenses various hyperelastic models of elastomers with respect to mechanical experiments under large deformations [17]. Thereafter, free-energy-derived models emerged, being modelled according to the description of deformations in space. Notably, Mooney-Rivlin [18] derived a general representation of polynomial functions of the first two invariants of the Cauchy-Green tensor which provided a consistent way to define material models that can model the non-linear relationships between stress and strain. Since then, the theory of large elastic rubber deformations has been implemented based on numerical methods in commercial FEM tools. Besides hyperelasticity, another aspect of filled rubbers that plays an important role is the time-dependency or dissipative behaviour, substantiated by linear viscoelasticity [19, 20, 21]. In this context, the stress-strain relationship has a dissipative component represented by a rheological approach based on generalised Maxwell models [22, 23].

A generalisation of the viscoelastic behaviour is fairly well-established and involves combining Maxwell's elements in parallel, which are represented by kernel energy functions or series of Prony [24]. Relaxation and creep responses are then represented by transient solutions for the time dependency. Furthermore, rubber is influenced by the ambient temperatures [25] together with visco-elastic properties based on the time-temperature superposition formulated by Williams, Landel and Ferry [26, 27]. Work references with FEM analysis were conducted to predict the seal and gasket joint deformations in contact with rigid metallic interfaces under temperature influence [28]. Assuming a hyper-viscoelastic constitutive law for a silicone seal, the model simulations are achievable using non-linear commercial FEM software [5, 29]. Incompressible material models are found that are either implemented as derived from strain tensor invariants, such as Neo-Hook and Mooney-Rivlin free-energy models [30, 31, 32], or from eigenvalues of the stretch tensor e.g. Ogden [33]. About modelling and optimisation, door seals are mostly explored by automotive applications to deal with the closure reaction forces [34]. Experimental investigations of elastic leakage [35] and fluid percolation [36] show, at different scales, how the seal performance depends on the contact pressure. More advanced simulation techniques such as Computational Fluid Dynamics (CFD) [37] and Coupled Euler Lagrangian (CEL) [38] were used to simulate fluid-structural interactions between liquid pressure and seal behaviour in post-leak conditions. Remarkably, for aircraft door seal applications, the FEM analysis performed by Zhao [39] features a simplistic approach to prescribe the cabin pressure load with a Fluid Pressure Penetration (FPP) interaction. On the shape optimisation level, parametric studies with swellable elastomeric seals highlight the potential of minimising leakage [40] by finding the interface which maximises contact pressures. Therefore, pre-defined contact interactions are favoured to model the seal pressure.

Different options are found in the literature to optimise structures using FEM analysis. A collection of statistical and mathematical techniques based on the Response Surface Methodology [41] and Topology Optimisation [42] are applicable for linear and continuous problems. However, under large discontinuities or strong non-linearities, these techniques are not able to minimise multi-objective functions by establishing feasible solutions. Alternatively, several computer simulations are recommended to evaluate the relation between influencing variables of the model using DOE [43] depending on the sampling technique. Correlations between model inputs and outputs are statistically substantiated by Spearman's rank coefficients [44] according to the number of experiments. Considering a virtual test stand, GA [45] are effective to solve problems with a large number of global-local maxima and minima when further combined with gradient-based techniques [46]. While there is no consensus regarding the best solution for the structural optimisation of non-linear problems, parametric techniques are very useful when the critical scenarios and design space are delimited [47, 48]. Current CAE tools such as ABAQUS and ISIGHT have the potential to combine nonlinear material modelling with optimisation algorithms, while opening the path to explore innovative design solutions for aircraft door seals.

2. Fundamentals

In this chapter, the fundamentals that cover material modelling and optimisation techniques are reviewed. Based on references from Sidoroff [13], Haupt [49, 50] and Holzapfel [14], continuum mechanics is formally introduced to describe the behaviour of elastomers under mechanical and thermal loadings. From a parametric approach, optimisation techniques applicable to engineering problems [51, 52] are presented to investigate door seals under the scope of DOE [53].

2.1. Continuum mechanics

When subjected to a loading process, the material body performs a movement in space. The concept of configurations is used to illustrate how these transformations happen in different time frames, whereby the reference configuration (C_0) is associated with the initial position of the body, without stress and strain history at time t_0. The motion of the material body can be expressed as a transformation into the current configurations (C_t) at a given time t. A material points P at an elementary volume is described in terms of the system coordinates ($\mathcal{O}$) by the position vectors $\mathbf{X}$ and $\mathbf{x}$, in C_0 and C_t, respectively, as shown in Figure 2.1.

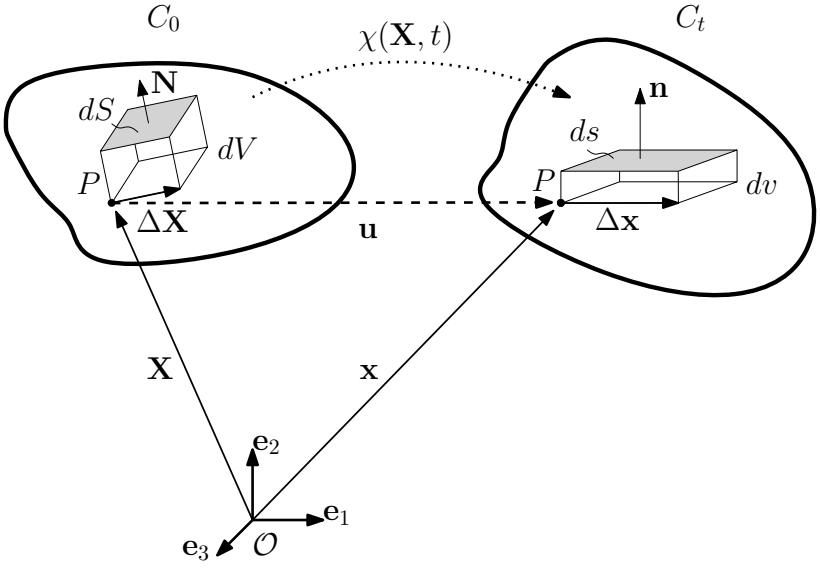

Figure 2.1. – Representation of the reference and current configurations.

2.1.1. Kinematics

By introducing the bijective transformation $\chi(\mathbf{X}, t)$, the position $\mathbf{x}$ of the material point P is written as a motion function of reference position $\mathbf{X}$ and time t:

$$\mathbf{x} = \chi(\mathbf{X}, t) \tag{2.1}$$

In a Lagrangian description, the coordinates of the vector $\mathbf{X}$ and the time t are selected as independent variables. In this case, the transformation $\chi(\mathbf{X}, t)$ describes the movement in relation to the reference configuration. Otherwise, $\chi^{-1}(\mathbf{x}, t)$ describes the vector X in a Eulerian description, with respect to the current configuration. To define the local transformation in the vicinity of P, considering the initial material line $\Delta\mathbf{X}$ on the reference and its image $\Delta\mathbf{x}$ on the current configuration, the tangent linear application is conventionally introduced:

$$\Delta\mathbf{x} = \frac{\partial\chi(\mathbf{X}, t)}{\partial\mathbf{X}} \cdot \Delta\mathbf{X} \tag{2.2}$$

For an infinitesimal distance, the deformation gradient $\mathbf{F}$ is introduced:

$$\mathrm{d}\mathbf{x} = \frac{\partial\chi(\mathbf{X}, t)}{\partial\mathbf{X}} \cdot \mathrm{d}\mathbf{X} = \mathbf{F} \cdot \mathrm{d}\mathbf{X} \tag{2.3}$$

while the displacement vector $\mathbf{u}$ is written to connect the position vectors of P:

$$\mathbf{u}(\mathbf{X}, t) = \mathbf{x}(\mathbf{X}, t) - \mathbf{X} \tag{2.4}$$

Through the derivation of Equation 2.4 with respect to the position vector $\mathbf{X}$, after rearranging the terms, $\mathbf{F}$ can be represented by the displacement vector $\mathbf{u}$, in the form:

$$\mathbf{F} = \frac{\partial\chi(\mathbf{X}, t)}{\partial\mathbf{X}} = \frac{\partial\mathbf{x}}{\partial\mathbf{X}} = \frac{\partial\mathbf{X}}{\partial\mathbf{X}} + \frac{\partial\mathbf{u}}{\partial\mathbf{X}} = \mathbf{I} + \mathrm{Grad}\mathbf{u} \tag{2.5}$$

where $\mathbf{I}$ is a second-order identity tensor. Intrinsically, the deformation gradient allows the configurations to be changed from C_0 to C_t, which establishes transformations for the volume and surface elements, by the Jacobian definition $J = \det(\mathbf{F})$:

$$\mathrm{d}v = J\mathrm{d}V \qquad \text{and} \qquad \mathbf{n}\mathrm{d}a = J\mathbf{F}^{-T} \cdot \mathbf{N}\mathrm{d}A \tag{2.6}$$

By definition, $\mathbf{F}$ describes the local motion around a material point P. For large deformations, it includes both rotations and pure distortions and hence it is not a good measure of strain. Thus, other deformation measures are introduced to only take the changes in shape into account, without keeping the rigid body rotations and displacements. From the deformation gradient, it is possible to extract the dilations and strain measures through a polar decomposition which helps to separate the rigid body motions from the total motion of the material body. Thus, different ways of measuring deformation are presented according to the finite strain theory.

2.1.2. Strain measures

Figure 2.2 shows how $\mathbf{F}$ is decomposed in two ways in a polar decomposition. The first transformation requires a deformation followed by a rotation, while the other starts with the rotation instead, and is followed by a different deformation.

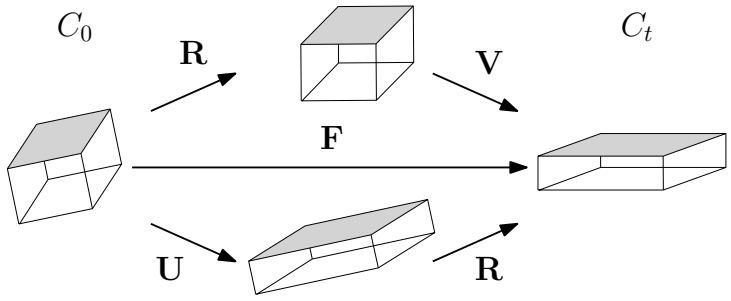

Figure 2.2. – Polar decomposition of the deformation gradient.

Both transformations in Figure 2.2 are equivalent, which yields the following relation:

$$\mathbf{F} = \mathbf{V} \cdot \mathbf{R} = \mathbf{R} \cdot \mathbf{U} \tag{2.7}$$

where $\mathbf{V}$ and $\mathbf{U}$ are respectively the right (in the Lagrangian description) and the left (in the Eulerian description) stretch tensors and $\mathbf{R}$ is an orthogonal rotation tensor. Each deformation tensor can be transformed into the other by forward and backward rotations as:

$$\mathbf{V} = \mathbf{R} \cdot \mathbf{U} \cdot \mathbf{R}^T \quad \text{and} \quad \mathbf{U} = \mathbf{R}^T \cdot \mathbf{V} \cdot \mathbf{R} \tag{2.8}$$

By considering the vectors $\mathrm{d}\mathbf{X}$ and $\mathrm{d}\mathbf{Y}$ in the reference configuration C_0 and their respective representations $\mathrm{d}\mathbf{x}$ and $\mathrm{d}\mathbf{y}$ in the actual configuration C_t, the following measure is introduced:

$$\mathrm{d}\mathbf{x} \cdot \mathrm{d}\mathbf{y} = (\mathbf{F} \cdot \mathrm{d}\mathbf{X}) \cdot (\mathbf{F} \cdot \mathrm{d}\mathbf{Y}) = \mathrm{d}\mathbf{X} \cdot \mathbf{F}^T \cdot \mathbf{F} \cdot \mathrm{d}\mathbf{Y} \tag{2.9}$$

where the right Cauchy-Green deformation tensor is written as:

$$\mathbf{C} = \mathbf{F}^T \cdot \mathbf{F} = \mathbf{U}^2 \tag{2.10}$$

In this way, the deformations are represented by the square of line elements in C_0. Alternatively, the deformation measure can also be expressed in C_t, as:

$$\mathrm{d}\mathbf{X} \cdot \mathrm{d}\mathbf{Y} = (\mathbf{F}^{-1} \cdot \mathrm{d}\mathbf{x}) \cdot (\mathbf{F}^{-1} \cdot \mathrm{d}\mathbf{y}) = \mathrm{d}\mathbf{x} \cdot \mathbf{F}^{-T} \cdot \mathbf{F}^{-1} \cdot \mathrm{d}\mathbf{y} \tag{2.11}$$

where the left Cauchy-Green deformation tensor is written as:

$$\mathbf{B} = \mathbf{F} \cdot \mathbf{F}^T = \mathbf{V}^2 \tag{2.12}$$

Usually, the strain measures relative to the undeformed material body are employed, by means of the difference of the scalar products. Thus, for the reference configuration, the Green-Lagrange finite strain tensor is introduced:

$$\mathbf{E} = \frac{1}{2}(\mathbf{C} - \mathbf{I}) \tag{2.13}$$

For the actual configuration, the Euler-Almansi tensor is expressed as:

$$\mathbf{A} = \frac{1}{2}(\mathbf{I} - \mathbf{B}^{-1}) \tag{2.14}$$

Both strain tensors can be transformed into one another through the so called *push forward* and *pull back* operations, respectively:

$$\mathbf{A} = \mathbf{F}^{-T} \cdot \mathbf{E} \cdot \mathbf{F}^{-1} \quad \text{and} \quad \mathbf{E} = \mathbf{F}^{T} \cdot \mathbf{A} \cdot \mathbf{F} \tag{2.15}$$

Additionally, by applying the last term of equation 2.5 for $\mathbf{F}$, it is possible to verify the difference between finite and infinitesimal strain approaches. To demonstrate it, the Green strain tensor $\mathbf{E}$ is expanded as:

$$\mathbf{E} = \frac{1}{2}(\mathrm{Grad}\mathbf{u} + \mathrm{Grad}^{T}\mathbf{u} + \mathrm{Grad}^{T}\mathbf{u} \cdot \mathrm{Grad}\mathbf{u}) \tag{2.16}$$

In the case of small strains, the non-linear term can be disregarded, which yields the classical definition of the engineering strain $\boldsymbol{\varepsilon}$:

$$\boldsymbol{\varepsilon} = \frac{1}{2}(\mathrm{Grad}\mathbf{u} + \mathrm{Grad}^{T}\mathbf{u}) \tag{2.17}$$

- **Principal scalar invariants**

Here the definitions of te principal invariants of a second-order tensor $\mathbf{Z}$ from the Cayley-Hamilton theorem are recalled:

$$\mathbf{Z}^3 - I_1\mathbf{Z}^2 + I_2\mathbf{Z} - I_3\mathbf{I} = \mathbf{0} \tag{2.18}$$

where the factors of the characteristic polynomial equation are written as:

$$I_1(\mathbf{Z}) = \mathrm{tr}(\mathbf{Z}) \tag{2.19}$$

$$I_2(\mathbf{Z}) = \frac{1}{2}(\mathrm{tr}(\mathbf{Z})^2 - \mathrm{tr}(\mathbf{Z}^2)) \tag{2.20}$$

$$I_3(\mathbf{Z}) = \det(\mathbf{Z}) \tag{2.21}$$

It is noticed that the third invariant is related to the Jacobian (J) employed in Equation 2.6 with regard to the deformation gradient $\mathbf{F}$:

$$I_3(\mathbf{F}) := J \tag{2.22}$$

2.1.3. Rate of deformation

Apart from the spatial relationship of the strain tensor, the rate at which the deformation gradient changes is also essential to model history dependent. The material velocity field $\mathbf{v}$ is expressed as the time derivative of the motion vector $\mathbf{x}$:

$$\mathbf{v} = \dot{\mathbf{x}} = \frac{\partial \mathbf{x}}{\partial t} \tag{2.23}$$

From Equation 2.4 it is possible to verify that $\mathbf{v} = \dot{\mathbf{u}}$ and hence the time derivative of the material deformation gradient $\mathbf{F}$ is given as:

$$\dot{\mathbf{F}} = \mathrm{Grad}\mathbf{v}(\mathbf{X}, t) = \frac{\partial \mathbf{v}}{\partial \mathbf{X}} \tag{2.24}$$

which is related to the spatial velocity gradient $\mathbf{L}$ with respect to the current configuration C_t by the following expression:

$$\mathbf{L} = \mathrm{grad}\mathbf{v}(\mathbf{x}, t) = \frac{\partial \mathbf{v}}{\partial \mathbf{x}} = \dot{\mathbf{F}} \cdot \mathbf{F}^{-1} \tag{2.25}$$

The spatial velocity gradient $\mathbf{L}$ describes the rate of change of a line element:

$$\dot{\mathbf{x}} = \dot{\mathbf{F}} \cdot \mathrm{d}\mathbf{X} = \dot{\mathbf{F}} \cdot \dot{\mathbf{F}}^{-1} \cdot \mathrm{d}\mathbf{x} = \mathbf{L} \cdot \mathrm{d}\mathbf{x} \tag{2.26}$$

which can be decomposed into symmetrical and anti-symmetrical parts, delivering, respectively, the Eulerian rate of deformation $\mathbf{D}$ and spin $\mathbf{W}$ tensors, by:

$$\mathbf{L} = \mathbf{D} + \mathbf{W} \qquad \text{where} \qquad \begin{cases} \mathbf{D} = \frac{1}{2}(\mathbf{L} + \mathbf{L}^T) = \mathbf{D}^T \\ \mathbf{W} = \frac{1}{2}(\mathbf{L} - \mathbf{L}^T) = -\mathbf{W}^T \end{cases} . \tag{2.27}$$

If the scalar product between two vectors $d\mathbf{x}$ and $d\mathbf{y}$ on C_t is derived in relation to time, the following expression is written in the Eulerian form:

$$\frac{\mathrm{d}}{\mathrm{d}t}(\mathrm{d}\mathbf{x} \cdot \mathrm{d}\mathbf{y}) = 2\mathrm{d}\mathbf{x} \cdot \mathbf{D} \cdot \mathrm{d}\mathbf{y} \tag{2.28}$$

In the same way, the material strain rate $\dot{\mathbf{E}}$ is described in the Lagrangian form:

$$\frac{\mathrm{d}}{\mathrm{d}t}(\mathrm{d}\mathbf{x} \cdot \mathrm{d}\mathbf{y}) = 2\mathrm{d}\mathbf{X} \cdot \dot{\mathbf{E}} \cdot d\mathbf{Y} \tag{2.29}$$

With 2.27, both rate tensors can be transformed into one another by:

$$\dot{\mathbf{E}} = \mathbf{F}^T \cdot \mathbf{D} \cdot \mathbf{F} \tag{2.30}$$

Or by the time derivative of Equation 2.13:

$$\dot{\mathbf{E}} = \frac{1}{2}\dot{\mathbf{C}} \tag{2.31}$$

In particular, $\mathbf{D}$ can be written as the Oldroyd rate of the Euler-Almansi tensor $\mathbf{A}$, which is represented by its objective Lie derivative:

$$\mathbf{D} = \overset{\triangle}{\mathbf{A}} = \dot{\mathbf{A}} + \mathbf{L}^T \cdot \mathbf{A} + \mathbf{A} \cdot \mathbf{L} \tag{2.32}$$

It is also related to the Green-Lagrange strain tensor $\mathbf{E}$ by employing the operation of *push forward* presented on Equation 2.15:

$$\overset{\triangle}{\mathbf{A}} = \mathbf{F}^{-T} \cdot \dot{\mathbf{E}} \cdot \mathbf{F}^{-1} \tag{2.33}$$

where the time derivatives do not depend on the reference configuration C_0. Similarly, by deriving Equation 2.12, it is also possible to obtain:

$$\dot{\mathbf{B}} = \mathbf{L} \cdot \mathbf{B} + \mathbf{B} \cdot \mathbf{L}^T \tag{2.34}$$

However, if a pre-deformation precedes a given state, the rigid body movements are not cancelled. Since $\dot{\mathbf{A}}$ and $\dot{\mathbf{B}}$ are not adequate strain rate measures, it is necessary to define a deformation gradient in an updated Lagrangian description, using:

$$\mathbf{F}(\tau) = \mathbf{F}_t(\tau) \cdot \mathbf{F}(t) \tag{2.35}$$

where $\mathbf{F}_t(\tau)$ is the relative deformation gradient subjected by the material between instants t and τ, which are denoted as the past and present configurations. This definition is important to establish the history-dependent constitutive relations of mechanical behaviour, which are explored at the end of this chapter. For the specific demonstration, the relative Green strain can be derived through:

$$\mathbf{C}_t(\tau) = \mathbf{F}_t(\tau)^T \cdot \mathbf{F}_t(\tau) \tag{2.36}$$

which is more appropriate to represent the strain histories as:

$$\mathbf{E}_t(\tau) = \frac{1}{2}(\mathbf{C}_t(\tau) - \mathbf{1}) = \mathbf{F}(t)^{-T}[\mathbf{E}(\tau) - \mathbf{E}(t)]\mathbf{F}(t)^{-1} \tag{2.37}$$

The polar decomposition is preserved in the case of relative configurations:

$$\mathbf{F}_t(\tau) = \mathbf{R}_t(\tau) \cdot \mathbf{U}_t(\tau) = \mathbf{V}_t(\tau) \cdot \mathbf{R}_t(\tau) \tag{2.38}$$

It can also be demonstrated that the derived strain rate tensors are respected:

$$\mathbf{L}(t) = \frac{\partial}{\partial \tau}\mathbf{F}_t(\tau)\bigg|_{\tau=t}, \quad \mathbf{W}(t) = \frac{\partial}{\partial \tau}\mathbf{R}_t(\tau)\bigg|_{\tau=t}, \quad \mathbf{D}(t) = \frac{\partial}{\partial \tau}\mathbf{U}_t(\tau)\bigg|_{\tau=t} \tag{2.39}$$

2.1.4. Stress tensors

Three tensor descriptions are presented to define the stress state in a solid depending on the choice of internal forces and surface elements. Figure 2.3 shows how the internal forces and element surfaces are displayed on C_0 and C_t.

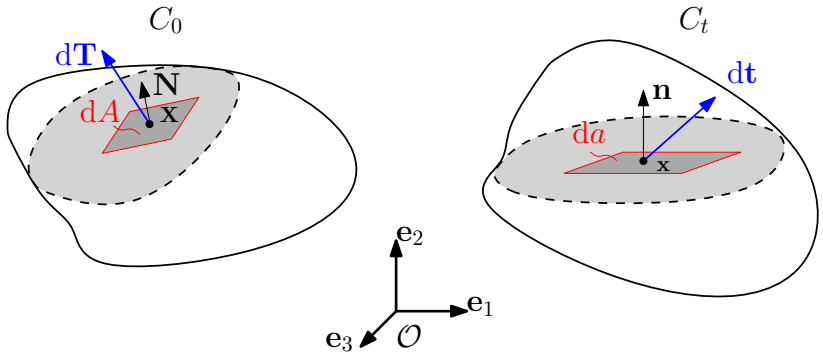

Figure 2.3. – Internal forces acting on an infinitesimal surface element vectors.

The stress on the current configuration can be calculated by the force vector $\mathrm{d}\mathbf{t}$ acting on an infinitesimal area $\mathrm{d}a$, with its normals. If the surfaces are taken with respect to C_t, the forces are derived from the true stress:

$$\mathrm{d}\mathbf{t} = \boldsymbol{\sigma} \cdot \mathbf{n}\mathrm{d}a \tag{2.40}$$

where $\boldsymbol{\sigma}$ is the Cauchy stress, being a symmetric second order tensor. On the other hand, the undeformed surface $\mathrm{d}A$ is usually employed to measure classical engineering stresses in a mixed description:

$$\mathrm{d}\mathbf{t} = \mathbf{P} \cdot J\mathbf{F}^{-T} \cdot \mathbf{N}\mathrm{d}A \tag{2.41}$$

where $\mathbf{P}$ is the first Piola-Kirchoff tensor, being asymmetric due to the transformation of surface elements according to 2.6. Physically, it represents the internal forces currently acting on an undeformed surface element. While $\boldsymbol{\sigma}$ is purely Eulerian, $\mathbf{P}$ is a mixed description. To define a complete Lagrangian description of the stress, the internal forces are transported to the reference configuration, by:

$$\mathrm{d}\mathbf{T} = \mathbf{F}^{-1} \cdot \mathrm{d}\mathbf{t} \tag{2.42}$$

which helps to define the second Piola-Kirchhoff tensor $\mathbf{S}$ which has no physical meaning, but has the particularity of being symmetrical:

$$\mathrm{d}\mathbf{T} = \mathbf{S} \cdot \mathbf{N}\mathrm{d}A \tag{2.43}$$

Therefore, the relationship between the three tensor descriptions is presented:

$$\mathbf{S} = J\mathbf{F}^{-1} \cdot \boldsymbol{\sigma} \cdot \mathbf{F}^{-T} = \mathbf{F}^{-1} \cdot \mathbf{P} \tag{2.44}$$

2.2. Balance equations

To establish the relationship between stress and strain measures, the balance equations are employed to conjugate physical quantities in continuum mechanics. Since all balance equations have the same form, a *master balance* is axiomatically introduced according to [14]. For a body (Ω), it generalises the temporal change of a physical quantity (ψ) multiplied by the material density (ρ) with its flux (φ) over the body boundary ($\partial\Omega$), a storage term (σ) and a production term ($\hat{\psi}$):

$$\frac{\mathrm{d}}{\mathrm{d}t}\int_{\Omega}\rho\psi(\mathbf{x},\,t)\,\mathrm{d}v \;=\; \int_{\partial\Omega}\varphi(\mathbf{x},\,t)\mathrm{d}a \;+\; \int_{\Omega}\sigma(\mathbf{x},\,t)\,\mathrm{d}v \;+\; \int_{\Omega}\hat{\psi}(\mathbf{x},\,t)\,\mathrm{d}v \tag{2.45}$$

Under the condition of continuity and continuous differentiability of the fields, the Reynolds' transport theorem is applied on the left term:

$$\frac{\mathrm{d}}{\mathrm{d}t}\int_{\Omega}\psi(\mathbf{x},\,t)\,\mathrm{d}v \;=\; \int_{\Omega}\dot{\psi}(\mathbf{x},\,t)\,\mathrm{d}v \tag{2.46}$$

Over the body boundary $\partial\Omega$, the total flux of the physical quantity can also be expressed as $\varphi = \boldsymbol{\Phi}\cdot\mathbf{n}$. By applying the divergence theorem, so that Equation 2.45 can be written without considering volume integrals, the local form of the master balance for a material point with velocity field $\mathbf{v}$ is obtained:

$$\dot{\psi} + \psi\,\mathrm{div}\,\mathbf{v} \;= \mathrm{div}\,\boldsymbol{\Phi} + \sigma + \hat{\psi} \tag{2.47}$$

2.2.1. Mass balance

In equation 2.47, different physical quantities can be attributed to ψ. If the density ρ is chosen, assuming that the right terms of flux (φ), storage (σ) and production ($\hat{\psi}$) are zero, it delivers the mass balance in the current configuration:

$$\dot{\rho} + \rho\,\mathrm{div}\,\mathbf{v} \;= 0 \tag{2.48}$$

By denoting ρ_0 as the density per unit volume at the reference configuration, the equation for the mass conservation is established by making use of equation 2.6:

$$\rho dv = \rho_0 dV \quad \text{or} \quad \rho_0 = J\rho \tag{2.49}$$

This relationship is important to describe the incompressible nature of rubber. In this particular case, the volume of a material element remains identical in both reference and current configurations. It leads to the following internal condition imposed on the deformation gradient that also implies $J = 1$:

$$\det(\mathbf{F}) = 1 \tag{2.50}$$

2.2.2. Linear momentum balance

In classical mechanics, the linear momentum balance is defined according to Newton's second axiom. According to this, the temporal change of momentum is caused by forces, acting on the volume and the surface elements. Figure 2.4 displays a free-body with boundary displacements and loads acting on each configuration:

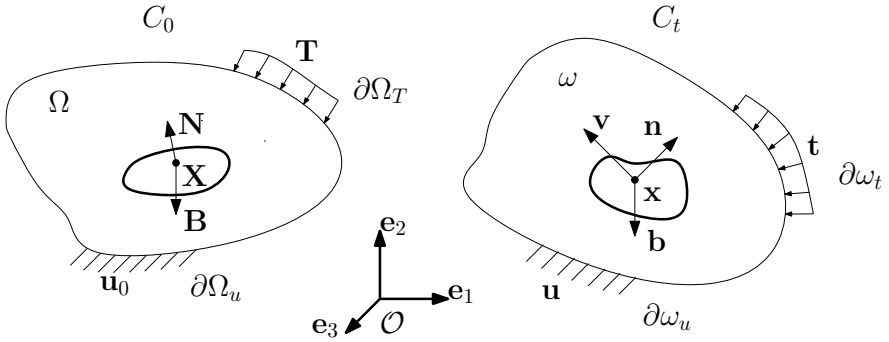

Figure 2.4. – Free-body on reference and current configurations.

The physical quantity ψ on the current configuration is taken by the impulse $\rho\,\mathbf{v}$. Additionally, the boundary flux is delivered by the traction forces of the Cauchy theorem $\mathbf{t} = \boldsymbol{\sigma} \cdot \mathbf{n}$, while the storage term is the body force $\rho\,\mathbf{b}$. No production term is considered, thus, the local form of the momentum balance is given by:

$$\rho\,\dot{\mathbf{v}} = \operatorname{div}\boldsymbol{\sigma} + \rho\,\mathbf{b} \tag{2.51}$$

If a static problem is taken, the left-hand term is neglected ($\dot{\mathbf{v}} = \mathbf{0}$), wherefore the resulting equation establishes the boundary value problem on C_t as:

$$\begin{cases} \operatorname{div}\boldsymbol{\sigma} + \rho\,\mathbf{b} = \mathbf{0} & \in \quad \omega \\ \boldsymbol{\sigma} \cdot \mathbf{n} = \mathbf{t} & \in \quad \partial\omega_t \\ \mathbf{u} = \mathbf{u}_0 & \in \quad \partial\omega_u \end{cases} \tag{2.52}$$

where the vector $\mathbf{u}_0$ and $\mathbf{t}$ are prescribed displacements imposed to the body boundaries. Another formulation of the problem can be written by taking the tractions on C_0 while also considering the mass conservation Equation 2.49:

$$\begin{cases} \operatorname{Div}\mathbf{P} + \rho_0\,\mathbf{B} = \mathbf{0} & \in \quad \Omega \\ \mathbf{P} \cdot \mathbf{N} = \mathbf{T} & \in \quad \partial\Omega_T \\ \mathbf{u} = \mathbf{u}_0 & \in \quad \partial\Omega_u \end{cases} \tag{2.53}$$

In the case of deformations from Equation 2.17, where the gradient $\mathbf{F}$ tends towards unity, the expressions on C_0 and C_t are the same, so $\boldsymbol{\sigma} \approx \mathbf{P} \approx \mathbf{S}$. The stresses are then usually denoted by the Cauchy tensor verifying the equilibrium equations and boundary conditions as shown in Equation 2.52.

2.2.3. Angular momentum balance

The evaluation of the angular momentum balance employs the physical quantity $\psi = \mathbf{r} \times \rho\mathbf{v}$, with $\mathbf{r}$ being the position vector over the body. Additionally, the terms considered for the balance are the flux ($\mathbf{r} \times \rho\mathbf{t}$) and the storage ($\mathbf{r} \times \rho\mathbf{b}$), which leads to the condition of symmetry of the Cauchy stress tensor, which is presented as:

$$\boldsymbol{\sigma} = \boldsymbol{\sigma}^T \tag{2.54}$$

As a consequence of this balance, it is possible to deduce that other tensors, such as the second Piola-Kirchhoff stress tensor $\mathbf{S}$ and the Kirchhoff stress ($\boldsymbol{\tau} = J\boldsymbol{\sigma}$), are also symmetric. However, from Equation 2.44, it is now clear why the first Piola-Kirchhoff stress tensor $\mathbf{P}$ is, in general, not symmetric as described in [54].

2.2.4. Energy balance (1st law of thermodynamics)

The energy balance is presented according to the first law of thermodynamics for the conservation of energy. For this, the transformation of external power is employed to obtain the physical quantities of interest. If only mechanical energy is considered, the power of the external forces is derived from the current configuration as:

$$\mathcal{P}_{ext} = \int_{\partial\omega} \mathbf{t} \cdot \mathbf{v} \, \mathrm{d}a + \int_{\omega} \mathbf{b} \cdot \mathbf{v} \, \mathrm{d}v \tag{2.55}$$

By using the divergence theorem, namely the linear momentum balance from Equations 2.51 and 2.32, the virtual work principle is established:

$$\int_{\partial\omega} \mathbf{t} \cdot \mathbf{v} \, \mathrm{d}a + \int_{\omega} \mathbf{b} \cdot \mathbf{v} \, \mathrm{d}v = \frac{\mathrm{d}}{\mathrm{d}t} \int_{\omega} \frac{1}{2} \rho\mathbf{v} \cdot \mathbf{v} \, \mathrm{d}v + \int_{\omega} \boldsymbol{\sigma} : \mathbf{D} \, \mathrm{d}v \tag{2.56}$$

In this case, the mechanical energy balance is according to $\mathcal{P}_{ext} = \dot{\mathcal{K}} + \mathcal{P}_{int}$, where:

$$\mathcal{K} = \int_{\omega} \frac{1}{2} \rho\mathbf{v} \cdot \mathbf{v} \, \mathrm{d}v \tag{2.57}$$

is the kinetic energy and the last term on the right of Equation 2.56 is the internal stress power, which can be expressed using different stress-strain descriptions, e.g.:

$$\mathcal{P}_{int} = \int_{\omega} \boldsymbol{\sigma} : \mathbf{D} \, \mathrm{d}v = \int_{\Omega} \mathbf{S} : \dot{\mathbf{E}} \, \mathrm{d}V = \int_{\Omega} \mathbf{P} : \dot{\mathbf{F}} \, \mathrm{d}V \tag{2.58}$$

If the variation of the kinetic energy is zero, the problem is called quasi-static, although the physical quantities may still depend on time. To account for thermal work, an additive quantity is used to express the total internal energy of the body:

$$\dot{\mathcal{E}} = \mathcal{P}_{int} + \mathcal{Q} \tag{2.59}$$

According to reference [55], the variation of the internal energy $\mathcal{E}$ is governed by the stress power $\mathcal{P}_{int}$ and the thermal power $\mathcal{Q}$ on the material whereby $\mathcal{E}$ is expressed in terms of the specific internal energy e:

$$\mathcal{E} = \int_{\omega} \rho\, e \,\mathrm{d}v = \int_{\Omega} \rho_0\, e \,\mathrm{d}V \tag{2.60}$$

Lastly, the thermal power $\mathcal{Q}$ is decomposed into a volume distributed supply (r) and a surface term derived from the Stokes' theorem ($-\mathbf{q}\cdot\mathbf{n}$):

$$\mathcal{Q} = \int_{\omega} \rho\, r \,\mathrm{d}v - \int_{\partial\omega} \mathbf{q}\cdot\mathbf{n}\,\mathrm{d}a = \int_{\Omega} \rho_0\, r \,\mathrm{d}V - \int_{\partial\Omega} \mathbf{Q}\cdot\mathbf{N}\,\mathrm{d}A \tag{2.61}$$

To express the energy balance in Equation 2.59 more explicitly, the divergence theorem is used, while Equations 2.58 and 2.61 are recalled to obtain:

$$\frac{d}{dt}\int_{\omega} \rho\, e \,\mathrm{d}v = \int_{\omega} (\boldsymbol{\sigma} : \mathbf{D} - \operatorname{div}\mathbf{q} + \rho\, r)\,\mathrm{d}v \tag{2.62}$$

The local form of the energy balance is presented in the current configuration:

$$\rho\,\dot{e} = \boldsymbol{\sigma} : \mathbf{D} - \operatorname{div}\mathbf{q} + \rho\, r \tag{2.63}$$

In this case, the master balance implies the physical quantity $\psi = \frac{1}{2}\rho\,\mathbf{v}\cdot\mathbf{v} + \rho\, e$, the sum of flow is $\boldsymbol{\sigma}\cdot\mathbf{v} - \mathbf{q}$ and the storage term is equal to $\rho(\mathbf{v}\cdot\mathbf{b} + r)$. The other forms of the local energy balance depend on the description of the stress power:

$$\rho_0\,\dot{e} = \mathbf{S} : \dot{\mathbf{E}} - \operatorname{Div}\mathbf{Q} + \rho_0\, r \tag{2.64}$$

$$\rho_0\,\dot{e} = \mathbf{P} : \dot{\mathbf{F}} - \operatorname{Div}\mathbf{Q} + \rho_0\, r \tag{2.65}$$

where the dual strain tensors of the kinematic quantities $\mathbf{D}$, $\mathbf{E}$ and $\mathbf{F}$ are obtained by writing the virtual power theorem.

2.2.5. Entropy balance (2nd law of thermodynamics)

The last balance considers the second law of thermodynamics which states that the entropy production should always increase according to the inequality:

$$\dot{\mathcal{S}} - \mathcal{T}_{ext} \geq 0 \tag{2.66}$$

where $\mathcal{S}$ is the system entropy and $\mathcal{T}_{ext}$ is the heat $\mathcal{Q}$ received by the system, divided by the temperature θ. The balance is introduced by a specific entropy η:

$$\mathcal{S} = \int_{\omega} \rho\,\eta \,\mathrm{d}v = \int_{\Omega} \rho_0\,\eta \,\mathrm{d}V \tag{2.67}$$

Equation 2.66 denotes a non-adiabatic system, according to which the entropy supply by the heat transport into the continuum body can be written as:

$$\mathcal{Q} = \int_{\omega} \frac{\rho\, r}{\theta}\, \mathrm{d}v - \int_{d\omega} \frac{\mathbf{q}\cdot\mathbf{n}}{\theta}\, \mathrm{d}a = \int_{\Omega} \frac{\rho_0\, r}{\theta}\, \mathrm{d}V - \int_{d\Omega} \frac{\mathbf{Q}\cdot\mathbf{N}}{\theta}\, \mathrm{d}A \tag{2.68}$$

By substituting Equations 2.67 and 2.68 into Equation 2.66, the Clausius-Duhem inequality is presented here in the Eulerian description:

$$\frac{d}{dt}\int_{\omega} \rho\,\eta\, \mathrm{d}v - \int_{\omega} \frac{\rho\, r}{\theta}\, \mathrm{d}v + \int_{d\omega} \frac{\mathbf{q}\cdot\mathbf{n}}{\theta}\, \mathrm{d}a \geq 0 \tag{2.69}$$

In material modelling, this inequality is widely employed according to the citations [56, 57]. To derive the local form, the divergence theorem is once more employed with the product form:

$$\begin{aligned} \int_{d\omega} \frac{\mathbf{q}\cdot\mathbf{n}}{\theta}\, \mathrm{d}a = \int_{\omega} \mathrm{div}\left(\frac{\mathbf{q}}{\theta}\right)\, \mathrm{d}v &= \int_{\omega} \left[\frac{1}{\theta}\mathrm{div}\,\mathbf{q} + \mathbf{q}\cdot\mathrm{grad}\left(\frac{1}{\theta}\right)\right] \mathrm{d}v \\ &= \int_{\omega} \left[\frac{1}{\theta}\mathrm{div}\,\mathbf{q} - \frac{1}{\theta^2}\mathbf{q}\cdot\mathrm{grad}\,(\theta)\right] \mathrm{d}v \end{aligned} \tag{2.70}$$

In C_t and C_0 respectively, the inequality in Equation 2.69 locally becomes:

$$\rho\dot{\eta} - \frac{\rho r}{\theta} + \mathrm{div}\left(\frac{\mathbf{q}}{\theta}\right) \geq 0 \tag{2.71}$$

$$\rho_0\dot{\eta} - \frac{\rho_0 r}{\theta} + \mathrm{Div}\left(\frac{\mathbf{Q}}{\theta}\right) \geq 0 \tag{2.72}$$

From the master balance it is possible to achieve these equations, considering that the physical quantity is the entropy $\rho\eta$, the flow term is defined by $-\mathbf{q}/\theta$ and the storage term is $\rho r/\theta$. No production terms are considered in this case. Finally, by introducing Equation 2.63 into the Equations 2.71 and Equation 2.64 and 2.65 into the Equation 2.72, three formulations of the Clausius-Duhem inequality are obtained:

$$-\rho(\dot{e} - \theta\dot{\eta}) + \frac{\mathbf{q}}{\theta}\cdot\mathrm{grad}\theta + \boldsymbol{\sigma} : \mathbf{D} \geq 0 \tag{2.73}$$

$$-\rho_0(\dot{e} - \theta\dot{\eta}) + \frac{\mathbf{Q}}{\theta}\cdot\mathrm{Grad}\theta + \mathbf{S} : \dot{\mathbf{E}} \geq 0 \tag{2.74}$$

$$-\rho_0(\dot{e} - \theta\dot{\eta}) + \frac{\mathbf{Q}}{\theta}\cdot\mathrm{Grad}\theta + \mathbf{P} : \dot{\mathbf{F}} \geq 0 \tag{2.75}$$

It is important to emphasise that the symbol θ represents the absolute temperature in units of Kelvin. If isothermal boundary conditions are imposed, then the remaining terms are part of the Clausius-Planck inequality[13].

2.3. Materials theory

In the previous section, the equations describing the kinematics and physical balances were formulated independently of the material behaviour. According to Sidoroff [13], the derivatives of the physical variables with respect to time do not interfere with the definition of the local state, hence the state evolution is considered as a succession of equilibrium states. A local approach is carried out to completely determine the thermodynamic state at any point on a body, where the constitutive laws are usually distinguished in the literature [14, 54] according to two types of variable relations:

- **Process variables**

  Hereinafter, the pair strain and temperature can directly be obtained from the measurements. This choice is equivalent to considering $\mathbf{F}$ and θ with regard to each gradient transformation.

- **Internal variables**

  These are introduced to describe complex phenomena such as plasticity, damage or viscosity. In this case, the internal variables of interest are mostly defined according to the aircraft door seal problem in the following chapters.

The more complex the model is from a thermodynamic point of view, the more difficult its numerical implementation is. It is necessary to identify the predominant phenomena in the behaviour of the material, to introduce a reduced but sufficient number of variables, without affecting the desired material predictions. Therefore, the relationships that represent the material behaviour may be adequately simulated. Since this work makes use of simple material models that are already implemented in commercial FEM software, the precision that is sought to determine certain elastomer physical phenomena is limited to the material models already implemented on ABAQUS 2018. Nevertheless, the conditions put forward in this study are assumed to be verified and generalizable to descriptions with internal variables. Depending on the thermodynamic variables, the existence of a specific thermodynamic free Helmholtz energy potential ψ is postulated, in the form of the following Legendre transformation:

$$\psi = e - \eta\theta \tag{2.76}$$

with the time derivative introduced into the Clausius-Duhem inequalities as:

$$-\rho\dot{\psi} - \rho\eta\dot{\theta} + \frac{\mathbf{q}}{\theta} \cdot \mathrm{grad}\theta + \boldsymbol{\sigma} : \mathbf{D} \geq 0 \tag{2.77}$$

$$-\rho_0\dot{\psi} - \rho_0\eta\dot{\theta} + \frac{\mathbf{Q}}{\theta} \cdot \mathrm{Grad}\theta + \mathbf{S} : \dot{\mathbf{E}} \geq 0 \tag{2.78}$$

$$-\rho_0\dot{\psi} - \rho_0\eta\dot{\theta} + \frac{\mathbf{Q}}{\theta} \cdot \mathrm{Grad}\theta + \mathbf{P} : \dot{\mathbf{F}} \geq 0 \tag{2.79}$$

The free energy function plays a central role in phenomenological models. The scalar formulation is based on process variables, e.g $\mathbf{B}$ and θ, together with internal variables denoted as $\mathcal{A}_i$ and α_i, respectively on C_0 and C_t. Thus, the free Helmholtz energy function may present the following relationship with the current configuration:

$$\psi = \psi(\mathbf{B}, \theta, \alpha_1, \alpha_2, ..., \alpha_n) \tag{2.80}$$

The total time derivative of the scalar function is expressed in the tensorial form:

$$\dot{\psi} = \frac{\partial \psi}{\partial \mathbf{B}} : \dot{\mathbf{B}} + \frac{\partial \psi}{\partial \theta} : \dot{\theta} + \frac{\partial \psi}{\partial \alpha_i} \bullet \dot{\alpha_i} \tag{2.81}$$

where $\bullet$ denotes the contracted product to the number of orders sufficient for the result to be a scalar. Since $\mathbf{B}$ is symmetric, Equation 2.34 is rearranged after the first term from the right side of Equation 2.81 in the following way:

$$\frac{\partial \psi}{\partial \mathbf{B}} : \dot{\mathbf{B}} = \frac{\partial \psi}{\partial \mathbf{B}} : (\mathbf{L} \cdot \mathbf{B} + \mathbf{B} \cdot \mathbf{L}^T) = \frac{\partial \psi}{\partial \mathbf{B}} : (\mathbf{L} \cdot \mathbf{B}) + \frac{\partial \psi}{\partial \mathbf{B}} : (\mathbf{B} \cdot \mathbf{L}^T) \tag{2.82}$$

$$= \frac{\partial \psi}{\partial \mathbf{B}} \cdot \mathbf{B}^T : \mathbf{L} + \mathbf{B}^T \cdot \frac{\partial \psi}{\partial \mathbf{B}} : \mathbf{L}^T \tag{2.83}$$

$$= \mathbf{B} \cdot \frac{\partial \psi}{\partial \mathbf{B}} : \mathbf{L} + \mathbf{B}^T \cdot \frac{\partial \psi}{\partial \mathbf{B}} : \mathbf{L}^T \tag{2.84}$$

$$= 2\mathbf{B} \cdot \frac{\partial \psi}{\partial \mathbf{B}} : \mathbf{L}^T \tag{2.85}$$

In the specific case that the material response is the same in all directions, the free energy can be defined as an isotropic scalar function that respects:

$$\psi(\mathbf{R}^T \cdot \mathbf{B} \cdot \mathbf{R}) = \psi(\mathbf{B}) \tag{2.86}$$

where $\mathbf{R}$ is an orthogonal rotation tensor. Under this assumption, and considering the symmetry of $\mathbf{B} \cdot \frac{\partial \psi}{\partial \mathbf{B}}$, the following tensorial operation is valid:

$$\mathbf{B} \cdot \frac{\partial \psi}{\partial \mathbf{B}} : \mathbf{L}^T = \mathbf{B} \cdot \frac{\partial \psi}{\partial \mathbf{B}} : \mathbf{D} \tag{2.87}$$

By replacing this last expression in $\dot{\psi}$ and then in the inequality in Equation 2.77 the following expression is obtained:

$$(\boldsymbol{\sigma} - 2\rho\mathbf{B} \cdot \frac{\partial \psi}{\partial \mathbf{B}}) : \mathbf{D} - \rho(\eta - \frac{\partial \psi}{\partial \theta}) : \dot{\theta} - \rho \frac{\partial \psi}{\partial \alpha_i} \bullet \dot{\alpha_i} - \frac{\mathbf{q}}{\theta} \cdot \text{grad}\theta \geq 0 \tag{2.88}$$

The constitutive relations arise from the reasoning of Coleman and Noll [57]. Hence, the process variables ($\mathbf{D}$ and $\dot{\theta}$), the internal variables (α_i) and the heat flux ($\mathbf{q}$) are evaluated separately, while satisfying the Clausius-Duhem inequality. For the other descriptions in Equations 2.78 and 2.79, the inequalities for material model formulation are not presented here.

2.3.1. Isotropic hyperelasticity

In this section, the phenomenological constitutive equation that describes the hyperelastic response of elastomers is discussed without thermodynamic variables, such as temperature and entropy. From the first term of the Clausius-Duhem inequality 2.77, the Clausius-Planck inequality is presented:

$$(\boldsymbol{\sigma} - 2\rho\mathbf{B}\cdot\frac{\partial\psi}{\partial\mathbf{B}}) : \mathbf{D} \geq 0 \tag{2.89}$$

For ny deformation history, the free energy function and the stress must respect the Clausius-Planck inequality. This important concept in elasticity is related to the polyconvexity of strain energy functions that are presented in previous studies in the literature [58, 59]. For the hyperelastic behaviour, the constitutive equations are to be defined in terms of the strain measures, without energy dissipation. Evaluating the inequality in Equation 2.89 results in the constitutive model:

$$\boldsymbol{\sigma} = 2\rho\mathbf{B}\cdot\frac{\partial\psi}{\partial\mathbf{B}} \tag{2.90}$$

In the case of internal variables determined entirely through intermediate states, the isotropy of the material is reflected in the invariance of the constitutive laws for any rotation. It simplifies the relationships of the constitutive equations by fully defining the free energy function through the invariants 2.19. Therefore, the strain energy functions could be defined by the invariants, either from $\mathbf{B}$ or from $\mathbf{C}$, since:

$$\psi(I_1(\mathbf{B}), I_2(\mathbf{B}), I_3(\mathbf{B})) = \psi(I_1(\mathbf{C}), I_2(\mathbf{C}), I_3(\mathbf{C})) \tag{2.91}$$

For Equation 2.90, the free energy depends on the left Cauchy-Green strain tensor $\mathbf{B}$, which by means of the chain rule of differentiation results in:

$$\frac{\partial\psi}{\partial\mathbf{B}} = \frac{\partial\psi}{\partial I_1}\frac{\partial I_1}{\partial\mathbf{B}} + \frac{\partial\psi}{\partial I_2}\frac{\partial I_2}{\partial\mathbf{B}} + \frac{\partial\psi}{\partial I_3}\frac{\partial I_3}{\partial\mathbf{B}} \tag{2.92}$$

The derivative of the first invariant I_1 with respect to $\mathbf{B}$ can be reformulated by the double contraction operation, which results in:

$$\frac{\partial I_1}{\partial\mathbf{B}} = \frac{\partial\mathrm{tr}(\mathbf{B})}{\partial\mathbf{B}} = \frac{\partial\mathbf{I}:\mathbf{B}}{\partial\mathbf{B}} = \mathbf{I} \tag{2.93}$$

The derivatives of I_2 and I_3 are similarly obtained using the Caylay-Hamilton theorem in Equation 2.18 and the invariant relations in Equation 2.19:

$$\frac{\partial I_2}{\partial\mathbf{B}} = \frac{1}{2}\left(2\mathrm{tr}(\mathbf{B})\,\mathbf{I} - \frac{\partial\mathrm{tr}(\mathbf{B}^2)}{\partial\mathbf{B}}\right) = I_1\mathbf{I} - \mathbf{B} \tag{2.94}$$

$$\frac{\partial I_3}{\partial\mathbf{B}} = \frac{\partial\det(\mathbf{B})}{\partial\mathbf{B}} = \det(\mathbf{B})\mathbf{B}^{-T} = I_3\mathbf{B}^{-1} \tag{2.95}$$

By substituting each of the invariants' derivatives into Equation 2.90, the Cauchy tensor is presented in its most general form in terms of the strain invariants:

$$\boldsymbol{\sigma} = 2\frac{\rho_0}{J}\left[\left(\frac{\partial\psi}{\partial I_1} + I_1\frac{\partial\psi}{\partial I_2}\right)\mathbf{B} - \frac{\partial\psi}{\partial I_2}\mathbf{B}^2 + I_3\frac{\partial\psi}{\partial I_3}\mathbf{I}\right] \tag{2.96}$$

where the density ρ_0 is converted to the reference configuration according to the mass balance in Equation 2.49. Since many elastomers do not exhibit large volume changes under large strains, the incompressible hyperelasticity is often employed to impose constraints on the Jacobian which from Equation 2.50, implies that $J = \sqrt{I_3(\mathbf{B})} = 1$. This internal constraint has implications for the general formulation of hyperelasticity. Essentially, the pure volumetric stresses should not affect the strain values of an incompressible material. Therefore, the free energy function must only be governed by isochoric deformations. Which be achieved by modifying the dependence of the free energy function on the third invariant. To formulate the incompressible constitutive equation, the free energy should be reformulated as the first two invariants are the only independent variables:

$$\hat{\psi} = \psi(I_1, I_2) - p(I_3 - 1) \tag{2.97}$$

where p works as an intermediate Lagrange multiplier [14]. In other words, it does not affect the mechanical work and must be determined from the boundary conditions. From the Coleman-Noll procedure 2.90, the constitutive equations are associated with I_1 and I_2 by the chain rule operation:

$$\boldsymbol{\sigma} = 2\rho\mathbf{B}\cdot\frac{\partial\psi(I_1, I_2)}{\partial\mathbf{B}} - 2\rho\mathbf{B}\cdot\frac{\partial p(I_3 - 1)}{\partial\mathbf{B}} \tag{2.98}$$

$$= 2\rho\mathbf{B}\cdot\frac{\partial\psi(I_1, I_2)}{\partial\mathbf{B}} - 2\rho\mathbf{B}\cdot pI_3\mathbf{B}^{-1} \tag{2.99}$$

$$= 2\rho\mathbf{B}\cdot\frac{\partial\psi(I_1, I_2)}{\partial\mathbf{B}} - p_H\mathbf{I} \tag{2.100}$$

where p_H plays the role of hydrostatic pressure. Under the incompressibility constraint, the density $\rho = \rho_0$ is constant, while the derivative is replaced by equations 2.93 and 2.94, according to:

$$\boldsymbol{\sigma} = 2\rho_0\left[\left(\frac{\partial\psi}{\partial I_1} + I_1\frac{\partial\psi}{\partial I_2}\right)\mathbf{B} - \frac{\partial\psi}{\partial I_2}\mathbf{B}^2\right] - p_H\mathbf{I} \tag{2.101}$$

Alternatively, the Cayley-Hamilton theorem can be used to substitute $\mathbf{B}^2$ in favour of $\mathbf{B}^{-1}$, while also absorbing the second invariant recurrence by p_H^* as shown below:

$$\boldsymbol{\sigma} = 2\rho_0\left(\frac{\partial\psi}{\partial I_1}\mathbf{B} - \frac{\partial\psi}{\partial I_2}\mathbf{B}^{-1}\right) - p_H^*\mathbf{I} \tag{2.102}$$

Equations 2.101 and 2.102 describe incompressible hyperelasticity. This is rather handful for comparisons between analytical calculations and experimental results from uniaxial, shear and bi-axial tests. However, for the numerical implementation into FEM, solving this internal constraint is not straightforward. In Equations 2.101 and 2.102, the diagonal stress can assume arbitrary values, which are independent of $\mathbf{B}$, due to the Lagrange multiplier and the identity tensor contribution. Some resources are feasible for the FEM implementation, either through hybrid elements [5] that dedicate an integration point to the hydrostatic components, or through a compressible formulation. In both cases, a degree of material compressibility is considered for numerical solutions in a so-called near incompressible approach. For compressible hyperelasticity, a solution proposed by Flory [60] is to decouple the volumetric and isochoric responses of the material. In this case, a multiplicative split of the deformation gradient is proposed:

$$\mathbf{F} = \hat{\mathbf{F}} \cdot \bar{\mathbf{F}} \tag{2.103}$$

where $\hat{\mathbf{F}}$ describes the volumetric deformations: $\hat{\mathbf{F}} = J^{1/3}\mathbf{I}$. Thus, the following transformation considers the gradient of deformation $\bar{\mathbf{F}}$ under constant volume:

$$\mathbf{F} = (J^{1/3}\mathbf{I})\bar{\mathbf{F}} \quad \text{and} \quad \mathbf{B} = J^{2/3}\bar{\mathbf{B}} \tag{2.104}$$

$\bar{\mathbf{B}}$ is now defined as an isochoric left Cauchy-Green deformation tensor, which allows for decoupling the free energy into isochoric and volumetric contributions:

$$\psi(\mathbf{B}) = \psi_{iso}(\bar{\mathbf{B}}) - \psi_{vol}(J) \tag{2.105}$$

The deviatoric invariants of $\bar{\mathbf{B}}$ are given by:

$$\bar{I}_1 = J^{-2/3}I_1 \quad \text{and} \quad \bar{I}_2 = J^{-4/3}I_2 \tag{2.106}$$

Deriving the constitutive law for the compressible case requires a little more computation than for incompressible case. Nevertheless, it is possible to obtain the Cauchy stress derived from the modified strain gradient containing both isochoric and volumetric contributions as:

$$\boldsymbol{\sigma} = 2\rho_0 J^{-1}\mathbf{B}\frac{\partial\psi}{\partial\mathbf{B}} = (\bar{\boldsymbol{\sigma}} : \mathbb{P}) - p\mathbf{I} \tag{2.107}$$

where $p = \frac{1}{3}\text{tr}(\boldsymbol{\sigma})$ and $\mathbb{P}$ is the fourth order projection tensor according to:

$$\mathbb{P} = J^{2/3}\mathbf{B}^{-1}\frac{\partial\bar{\mathbf{B}}}{\partial\mathbf{B}}\mathbf{B} = (\mathbb{I} - \frac{1}{3}\mathbf{I}\otimes\mathbf{I}) \tag{2.108}$$

with $\mathbb{I}$ being a fourth order identity tensor and the deviatoric stress written as:

$$\bar{\boldsymbol{\sigma}} = 2\rho_0 J^{-1}\bar{\mathbf{B}}\frac{\partial\psi_{iso}(\bar{I}_1, \bar{I}_2)}{\partial\bar{\mathbf{B}}} \tag{2.109}$$

As a consequence, the isochoric stress response of the isotropic hyperelasticity must be based on the choice of free energy functions that depend on the first two invariants. Several specific functions have been proposed for elastomers in the isothermal and quasi-static regime through a phenomenological approach [15]. Some well-known incompressible and nearly incompressible models are implemented in ABAQUS, mainly derived from the principal invariants, such as: neo-Hookean, Yeoh [61], Arruda-Boyce and the polynomial Mooney-Rivlin forms. To check the polyconvexity of the free energy function, the software asses whether the given model parameters fulfil the following boundary conditions:

$$\begin{cases} \psi(\mathbf{B}) = 0 & \mathbf{F} = \mathbf{I} \\ \psi(\mathbf{B}) \to +\infty & \lambda_i \to +\infty \end{cases} \quad \text{and} \quad \begin{cases} \psi(\mathbf{B}) \to +\infty & J \to +\infty \\ \psi(\mathbf{B}) \to +\infty & J \to 0^+ \end{cases} \tag{2.110}$$

The parameter λ_i comprises the principal stretches, from the eigenvalues of $\mathbf{U}$, and the Jacobian must be taken when compressibility is considered. This verification is performed with assistance of the Hill inequality [62] or Drucker's criterion [63]:

$$\frac{d\boldsymbol{\tau}}{dt} : \mathbf{D} > 0 \quad \forall\, \mathbf{D} \neq \mathbf{0} \tag{2.111}$$

where the Kirchhoff stress $\boldsymbol{\tau} = J\boldsymbol{\sigma}$ is given and $\mathbf{D}$ is the rate of deformation. To explore the existing capabilities in ABAQUS, under the operating limits of an aircraft door, two of the available energy functions are selected for the hyperelastic model.

- **neo-Hookean**

$$\rho\psi = C_{10}(I_1 - 3) + \frac{1}{D_1}(J-1)^2 \tag{2.112}$$

The neo-Hookean is the simplest model relating to hyperelasticity - since it only depends on the first invariant. Theoretically, this model offers satisfactory adherence to stretch levels up to $\lambda_i = 1.5$, or 50% strain [64]. For small strains, the parameter's first invariant is related to the shear modulus ($\mu = 2\,C_{10}$), while the Jacobian is related to the inverse of the bulk modulus ($k = 2\,D_1^{-1}$), in case of compressibility.

- **Mooney-Rivlin (general)**

$$\rho\psi = \sum_{i+j>1}^{n} C_{ij}(I_1 - 3)^i (I_2 - 3)^j + \sum_{i>1}^{n} \frac{1}{D_i}(J-1)^{2i} \tag{2.113}$$

The general Mooney-Rivlin model is presented with the polynomial order n with the first and second invariants. Depending on the strain levels, a higher polynomial order of the energy function can be employed to better describe the hyperelastic behaviour. In ABAQUS, Mooney-Rivlin is only denoted when $n = 1$ and the Polynomial form when $n > 1$. For linear elasticity, the first order form has the shear modulus given by $\mu = 2\,(C_{10} + C_{01})$ and an identical bulk term ($k = 2\,D_1^{-1}$) as the neo-Hookean.

2.3.2. Finite linear viscoelasticity

The constitutive equations introduced earlier describe elastic stress-strain under purely mechanical conditions. In the case of viscoelastic material behaviour, isotropic hyperelasticity governs the equilibrium part of the stress, independent of the strain rate. However, elastomers also dissipate energy by means of relaxation, creep or a characteristic hysteresis with time dependency. Thus, the history of external loadings plays an important role in estimating the correct response of the non-equilibrium states governed by internal variables of a memory functional. Under the assumption of incompressibility, which implies the existence of a constitutively undetermined pressure, generalised stress is presented as follows:

$$\boldsymbol{\sigma}(t) = \bar{\boldsymbol{\sigma}}(t) - p(\mathbf{X}, t)\mathbf{I} \tag{2.114}$$

By keeping compatibility with the internal constraint, the deviatoric stress can be written as a functional of the entire strain history:

$$\bar{\boldsymbol{\sigma}}(t) = \underset{\tau \leq t}{\mathscr{F}}[\mathbf{E}(s)] \tag{2.115}$$

Since for viscoelastic bodies the equilibrium stress $\bar{\boldsymbol{\sigma}}_{eq}$ is a function of the current deformation, as shown in Equation 2.109, the expression is separated in two parts:

$$\bar{\boldsymbol{\sigma}}(t) = \bar{\boldsymbol{\sigma}}_{eq} + \bar{\boldsymbol{\sigma}}_{ov}(t) \tag{2.116}$$

where $\bar{\boldsymbol{\sigma}}_{ov}$ is defined as the overstress. This process-dependent of over stress is a functional of the strain history with fading memory written as:

$$\bar{\boldsymbol{\sigma}}_{ov}(t) = \underset{s \leq t}{\mathscr{F}}[\mathbf{E}_t(s), \mathbf{B}(t)] \tag{2.117}$$

where $\mathbf{E}_t(s)$ is the relative strain history derived from Equation 2.37:

$$\mathbf{E}_t(s) = \mathbf{F}^{-T}(t)[\mathbf{E}(t-s) - \mathbf{E}(t)]\mathbf{F}^{-1}(t) \tag{2.118}$$

The relaxation of the overstress to zero under temporally constant deformation must be satisfied by the normalisation condition:

$$\underset{s \leq t}{\mathscr{F}}[\mathbf{0}(s), \mathbf{B}(t)] = \mathbf{0} \tag{2.119}$$

In other words, the memory functional does not contribute to the equilibrium stress under static conditions. To establish a representation of overstress, a general theory of rate-dependent functionals developed by Coleman and Noll [65] is employed. From a rheological approach, the one-dimensional Maxwell model is given by:

$$\dot{\sigma}_{ov}(t) + \frac{\hat{E}}{\hat{\eta}}\sigma_{ov}(t) = \hat{E}\dot{\varepsilon}(t) \quad \Longrightarrow \quad \sigma_{ov}(t) = \int_{-\infty}^{t} \hat{E}e^{-\frac{\hat{E}}{\hat{\eta}}(t-s)}\acute{\varepsilon}(s)\mathrm{d}s \tag{2.120}$$

The principle behind rheological models is to describe the material behaviour by a set of springs and dampers, that are lined up in an internal mechanical system. The model must be able to represent the viscoelastic response by displaying relaxation and creep behaviour, which depends on the number of elements and how they are connected. In the differential Equation 2.120, a Maxwell element is calculated based on a spring and a damper in a series. While the first responds elastically according to the Hookean law with a Young's modulus $\hat{E}$, the second works as a Newtonian viscous fluid that dissipates energy through a dynamic viscosity $\hat{\eta}$. Different parallel set-ups are possible such as the Kelvin-Voigt and Poynting-Thomson models. Figure 2.5 shows a generalisation of Maxwell's model containing n-branches in parallel.

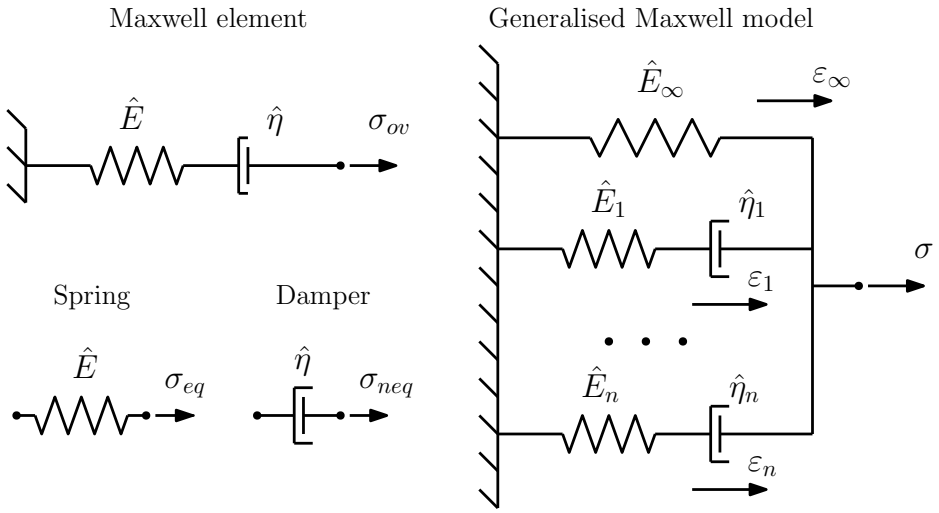

Figure 2.5. – Generalised Maxwell model and rheological elements.

From this generalised representation, the sum of the stresses is defined by:

$$\sigma = \sigma_\infty + \sum_{i=1}^{n} \sigma_{ov}^{i} \tag{2.121}$$

where the equilibrium stress σ_∞ is a function of the strain and σ_{ov}^{i} are the fading internal forces of the material observed in a process of relaxation. This approach for linear viscoelasticity can be extended to finite strains and hyperelasticity by two models, according to the work of Haupt & Lion [66]:

$$\text{Model A:} \qquad \overset{\triangle}{\bar{\boldsymbol{\sigma}}}_{ov} + \frac{1}{\tau_A}\bar{\boldsymbol{\sigma}}_{ov} = 2\mu_A \bar{\mathbf{D}} \tag{2.122}$$

$$\text{Model B:} \qquad \overset{\triangledown}{\bar{\boldsymbol{\sigma}}}_{ov} + \frac{1}{\tau_B}\bar{\boldsymbol{\sigma}}_{ov} = 2\mu_B \bar{\mathbf{D}} \tag{2.123}$$

The relaxation times τ_A and τ_B are the ratios between dynamic viscosities end the shear moduli of each model.

Model A employs a time derivative that is analogous to Oldroyd's rate in Equation 2.32, while in the case of Model B, the contravariant operation is used for the stress:

$$\overset{\triangledown}{\boldsymbol{\sigma}} = \dot{\boldsymbol{\sigma}} - \mathbf{L}\cdot\boldsymbol{\sigma} - \boldsymbol{\sigma}\cdot\mathbf{L}^T \tag{2.124}$$

For the negative strain rate $-\mathbf{D}$, the contravariant operation can be used as:

$$-\mathbf{D} = \overset{\triangledown}{\mathbf{a}} = \dot{\mathbf{a}} - \mathbf{L}\cdot\mathbf{a} - \mathbf{a}\cdot\mathbf{L}^T = \mathbf{F}\cdot\dot{\mathbf{e}}\cdot\mathbf{F}^T \tag{2.125}$$

where $\mathbf{a}$ is the Finger tensor written as:

$$\mathbf{a} = \frac{1}{2}(\mathbf{I} - \mathbf{B}) \tag{2.126}$$

and $\mathbf{e}$ is related to the Piola strain:

$$\mathbf{e} = \frac{1}{2}(\mathbf{C}^{-1} - \mathbf{I}) \tag{2.127}$$

To manipulate the models, the second Piola-Kirchoff tensor from Equation 2.44 is used together with the convected stress form on the current configuration:

$$\tilde{\mathbf{t}} = \mathbf{F}^{-T}\cdot\mathbf{S}\cdot\mathbf{F}^{-1} = \mathbf{F}^T\cdot\boldsymbol{\sigma}\cdot\mathbf{F} \tag{2.128}$$

The specific stress power is calculated according the corresponding dual variables:

$$\boldsymbol{\sigma} : \mathbf{D} = \mathbf{S} : \dot{\mathbf{E}} = -\tilde{\mathbf{t}} : \dot{\mathbf{e}} \tag{2.129}$$

Thus, for an isothermal process, the Clausius-Duhem inequality is simplified as:

$$\mathbf{S} : \dot{\mathbf{E}} - \rho_0\dot{\psi} \geq 0 \qquad \text{or} \qquad -\tilde{\mathbf{t}} : \dot{\mathbf{e}} - \rho_0\dot{\psi} \geq 0 \tag{2.130}$$

For incompressible isotropic solids the derivation steps of the overstress Equations 2.122 and 2.123 are presented by keeping the total form of stress:

$$\dot{\mathbf{S}}_{ov} + \frac{1}{\tau_A}\mathbf{S}_{ov} = -2\mu_A\dot{\mathbf{e}} \tag{2.131}$$

$$\dot{\tilde{\mathbf{t}}}_{ov} + \frac{1}{\tau_B}\tilde{\mathbf{t}} = +2\mu_B\dot{\mathbf{E}} \tag{2.132}$$

The solution of each constitutive law is obtained as shown in Equation 2.120:

$$\mathbf{S}_{ov}(t) = -\int_{-\infty}^{t} 2\mu_A\, e^{-\frac{(t-s)}{\tau_A}}\,\dot{\mathbf{e}}(s)\mathrm{d}s \tag{2.133}$$

$$\tilde{\mathbf{t}}_{ov}(t) = +\int_{-\infty}^{t} 2\mu_B\, e^{-\frac{(t-s)}{\tau_B}}\,\dot{\mathbf{E}}(s)\mathrm{d}s \tag{2.134}$$

The Cauchy stresses are obtained by transforming the previous solutions to the current configuration and by using the updated Lagrangian notation in Equation 2.118:

$$\boldsymbol{\sigma}_{ov}^{A}(t) = + \int_{-\infty}^{t} 2\mu_A \, e^{-\frac{(t-s)}{\tau_A}} \dot{\mathbf{e}}_t(s)\mathrm{d}s \tag{2.135}$$

$$\boldsymbol{\sigma}_{ov}^{B}(t) = - \int_{-\infty}^{t} 2\mu_B \, e^{-\frac{(t-s)}{\tau_B}} \dot{\mathbf{E}}_t(s)\mathrm{d}s \tag{2.136}$$

where $\mathbf{e}_t$ and $\mathbf{E}_t$ are the relative strain histories and the constitutive law have to be thermodynamically consistent. For each model, the energy functional is presented in the convolutional form, assuming compatibility with the Clausius-Duhem inequality:

$$\rho\psi_A(t) = - \int_{-\infty}^{t} 2G_A(t-s)\frac{\mathrm{d}}{\mathrm{d}s}\mathrm{tr}\mathbf{e}_t(s)\mathrm{d}s \tag{2.137}$$

$$\rho\psi_B(t) = - \int_{-\infty}^{t} 2G_B(t-s)\frac{\mathrm{d}}{\mathrm{d}s}\mathrm{tr}\mathbf{E}_t(s)\mathrm{d}s \tag{2.138}$$

where, the positive relaxation functions generally represented by $G(t)$ have to respect the following limit conditions:

$$\lim_{t\to\infty} G(t) = \mu, \quad \text{and} \quad \lim_{t\to\infty} \dot{G}(t) = 0 \tag{2.139}$$

After integration by parts and considering no pre-deformations, the free energy functional is written with a valid semi-opened time interval starting at zero:

$$\rho\psi_A(t) = \mu_A \mathrm{tr}\mathbf{E}(t) - \int_{0}^{t} 2G_A(t-s)\frac{\mathrm{d}}{\mathrm{d}s}\mathrm{tr}\mathbf{e}_t(s)\mathrm{d}s \tag{2.140}$$

$$\rho\psi_B(t) = \mu_B \mathrm{tr}\mathbf{e}(t) - \int_{0}^{t} 2G_B(t-s)\frac{\mathrm{d}}{\mathrm{d}s}\mathrm{tr}\mathbf{E}_t(s)\mathrm{d}s \tag{2.141}$$

where μ_A and μ_B are elasticity constants and the left parts of the equation are related to the fading memory part of the free energy. To investigate the dissipation inequalities, the following expressions are differentiated:

$$\frac{\mathrm{d}}{\mathrm{d}t}\mathrm{tr}\mathbf{e}_t(t-s) = 2\left[\mathbf{e}(t-s) - \mathbf{e}(t)\right]\dot{\mathbf{E}}(t) - \frac{\mathrm{d}}{\mathrm{d}s}\mathrm{tr}\mathbf{e}_t(t-s) \tag{2.142}$$

$$\frac{\mathrm{d}}{\mathrm{d}t}\mathrm{tr}\mathbf{E}_t(t-s) = 2\left[\mathbf{E}(t-s) - \mathbf{E}(t)\right]\dot{\mathbf{e}}(t) - \frac{\mathrm{d}}{\mathrm{d}s}\mathrm{tr}\mathbf{E}_t(t-s) \tag{2.143}$$

By inserting the previous relationships into the inequalities in Equation 2.130, the stresses $\mathbf{S}$ and $\tilde{\mathbf{t}}$ can be obtained by evaluating Equations 2.144 and 2.145:

$$\left[\mathbf{S}(t) - \mu_A\mathbf{I} + \int_0^t 2G_A[\mathbf{e}(t-s) - \mathbf{e}(t)]\mathrm{d}s\right] : \dot{\mathbf{E}} - \int_0^t G_A \mathrm{tr}\mathbf{e}_t(t-s)\mathrm{d}s \geq 0 \tag{2.144}$$

$$\left[\tilde{\mathbf{t}}(t) - \mu_B\mathbf{I} + \int_0^t 2G_B[\mathbf{E}(t-s) - \mathbf{E}(t)]\mathrm{d}s\right] : \dot{\mathbf{e}} - \int_0^t G_B \mathrm{tr}\mathbf{E}_t(t-s)\mathrm{d}s \geq 0 \tag{2.145}$$

The equivalent formulations related to the current configuration are obtained after a *push-forward* operation, which is presented by the deviatoric parts:

$$\bar{\boldsymbol{\sigma}}_{ov}^{A}(t) = \left[\mu_A\mathbf{B} - \int_0^t 2G_A\mathbf{e}_t(t-s)\mathrm{d}s\right]^D \tag{2.146}$$

$$\bar{\boldsymbol{\sigma}}_{ov}^{B}(t) = \left[-\mu_B\mathbf{B}^{-1} + \int_0^t 2G_B\mathbf{E}_t(t-s)\mathrm{d}s\right]^D \tag{2.147}$$

The remaining terms in Equations 2.144 and 2.145 correspond to the dissipated energy. Since $\mathrm{tr}\mathbf{E}_t$ and $\mathrm{tr}\mathbf{e}_t$ are always positive because of the incompressibility condition, for any mechanical process each relaxation function must respect:

$$\dot{G}(t) \leq 0 \quad \text{and} \quad \ddot{G}(t) \geq 0 \quad \forall\, t \tag{2.148}$$

Lastly, a combination between models A and B gives rise to the total stress functional, which has non-equilibrium components represented by the convolutional integrals:

$$\boldsymbol{\sigma}(t) = \mu_A\mathbf{B} - \mu_B\mathbf{B}^{-1} - \int_0^t 2G_A\mathbf{e}_t(t-s)\mathrm{d}s + \int_0^t 2G_B\mathbf{E}_t(t-s)\mathrm{d}s - p(t)\mathbf{I} \tag{2.149}$$

The equilibrium part has a similar representation if the energy function of Mooney-Rivlin is taken in Equation 2.102. If only model A is used, then the neo-Hookean model appears as the equilibrium part. A simple representation of the relaxation kernel functions is usually employed in the form of decreasing exponentials, as a Prony series depending on how many Maxwell elements are chosen:

$$G(t) = \sum_{k=1}^{n} \mu_k e^{-t/\tau_k} \tag{2.150}$$

A long experimental data acquisition might be necessary to cover the long-term relaxation behaviour of elastomers with good accuracy, whereby μ_k and τ_k parameters must be positive to respect the conditions defined in Equation 2.148.

Since the equilibrium and the non-equilibrium stresses are separated in Equation 2.149, the relaxation stress based on the generalised Maxwell model in te Equation 2.121 can easily be investigated. A quick deformation step at time $t = 0$ implies the following form of a step function to $\mathbf{F}_0$ of the deformation gradient:

$$\mathbf{F}(t) = \begin{cases} \mathbf{I} & \forall\, t \leq 0 \\ \mathbf{F}_0 & \forall\, t > 0 \end{cases} \quad \Longrightarrow \quad \boldsymbol{\sigma}(t) = \begin{cases} \mathbf{0} & \forall\, t \leq 0 \\ \boldsymbol{\sigma}_R & \forall\, t > 0 \end{cases} \tag{2.151}$$

From the convolution theorem of a step function, the non-equilibrium stresses are solved to suppress the time integration of the relative strain histories $\mathbf{E}_t$ and $\mathbf{e}_t$:

$$\boldsymbol{\sigma}_R(t) = -2G_A(t)\mathbf{F}_0 \cdot \mathbf{e}_0 \cdot \mathbf{F}_0^T + 2G_B(t)\mathbf{F}_0^{-T} \cdot \mathbf{E}_0 \cdot \mathbf{F}_0^{-1} - p(t)\mathbf{I} \tag{2.152}$$

By inserting the Piola and Green strain tensor at time zero:

$$\mathbf{e}_0 = \frac{1}{2}(\mathbf{F}_0^{-1} \cdot \mathbf{F}_0^{-T} - \mathbf{I}) \quad \text{and} \quad \mathbf{E}_0 = \frac{1}{2}(\mathbf{F}_0^T \cdot \mathbf{F}_0 - \mathbf{I}) \tag{2.153}$$

and employing the left Cauchy-Green deformation tensor definition $\mathbf{B}_0 = \mathbf{F}_0 \cdot \mathbf{F}_0^T$, the relaxation process is written as:

$$\begin{aligned} \boldsymbol{\sigma}_R(t) &= G_A(t)(\mathbf{B}_0 - \mathbf{I}) + G_B(t)(\mathbf{I} - \mathbf{B}_0^{-1}) - p(t)\mathbf{I} \\ &= G_A(t)\mathbf{B}_0 - G_B(t)\mathbf{B}_0^{-1} - p(t)\mathbf{I} \end{aligned} \tag{2.154}$$

The hydrostatic pressure p is constitutively undetermined. Since the relaxation process fades into the equilibrium stresses governed by the elastic (static) response, the instantaneous and equilibrium shear moduli G_0 and $G(\infty)$ are related to the relaxation function:

$$G(\infty) = G_0 \left(1 - \sum_{i=1}^{n} g_i\right) \qquad \Longrightarrow \qquad G(0) = G_0 = \tag{2.155}$$

where g_i are dimensionless coefficients of the relaxation function that respects the inequalities in Equation 2.148. It motivates an alternative formulation of the Prony series in Equation 2.150 that assumes the existence of the instantaneous modulus G_0:

$$G(t) = G_0 \left[1 - \sum_{i=1}^{n} g_i(1 - e^{-t/\tau_i})\right] \tag{2.156}$$

The experimental identification of the instantaneous elastic terms is difficult due to the large strain rate required at $t = 0$. However, the final solution remains mathematically valid, since each long-term and instantaneous term are related to each other as described in Equation 2.155. The time domain generalisation for hyperelastic materials implemented in ABAQUS uses the instantaneous stress $\boldsymbol{\sigma}_0$ as the core function for the hereditary integral formulation. Besides dealing with deviatoric stresses, the

hydrostatic pressure may be integrated on the basis of relaxation kernel functions. However, for the nearly incompressible behaviour of rubber, the relaxation of the bulk modulus is neglected, which leads to the following representation of the convolutional form of the stress quantities:

$$\boldsymbol{\sigma}(t) = \boldsymbol{\sigma}_0(t) + \int_0^t \frac{G(\tau)}{G_0} \boldsymbol{\sigma}_0(t-s) \mathrm{d}\tau - p(t)\mathbf{I} \tag{2.157}$$

Here the reduced time τ is introduced to provide a dependency with the temperature shift function A_θ. The reduced time is related to the actual time s through the time-superposition principle according to the differential equation:

$$\mathrm{d}\tau = \frac{\mathrm{d}s}{A_\theta(\theta(s))} \tag{2.158}$$

where A_θ is the Williams-Landel-Ferry (WLF) equation [67] implemented in ABAQUS in the following form:

$$-\log A_\theta = h(\theta) = \frac{C_1(\theta - \theta_g)}{C_2 + (\theta - \theta_g)} \tag{2.159}$$

where C_1^g and C_2^g are constants that can be calibrated by temperature-dependent relaxation experiments, and θ_g is the glass transition temperature of the material. According to [5], it is possible to use 'universal' constants for rubber at any convenient temperature range, other than below the glass transition. Therefore, a transformation to the reference temperature (θ_0) of the relaxation experiment is considered:

$$C_1 = \frac{C_1^g}{1 + (\theta_0 - \theta_g)/C_2^g} \tag{2.160}$$

$$C_2 = C_2^g + \theta_0 - \theta_g \tag{2.161}$$

Although each polymer presents a unique signature for the WLF constants, it is possible to investigate the influence of temperature in the vicinity of the glass transition of the material. Room temperature measurements in uniaxial conditions are proposed for finite strain viscoelasticity modelling. Initially, quasi-static tests for the incompressible isotropic hyperelastic behaviour of silicone are derived from quasi-static loadings. Optimisation methods are introduced in the following section and can be applied to the fitting of models with experimental data. In the next chapter, relatively inexpensive experimental investigations are presented to obtain the material model parameters based on aircraft doors seal samples. Since FEM implementation of material models reviewed in this chapter is available in several commercial software packages, this topic is not discussed in depth in this work, although, the continuum mechanics formalism is concluded to facilitate the understanding of subsequent analysis sections.

2.4. Introduction to optimisation

In this section, the basic concepts of nonlinear optimisation techniques are discussed for problems concerning: parametric identification, DOE and multi-objective optimisation. Typically, optimisation is a process that may involve maximising or minimising the values of one or more functions through the 'optimal' choice of design variables or parameters. In a general formulation, the optimisation tasks in this work are given by the following constrained minimisation problem:

$$\min_{x_i} \quad f(x_i) \qquad \text{Objective function} \tag{2.162a}$$

$$\text{subject to} \quad h(x_i) \geq 0 \text{ or } h(x_i) = 0 \qquad \text{Boundary constraint} \tag{2.162b}$$

$$l_i \geq x_i \geq u_i \qquad \text{Design constraints} \tag{2.162c}$$

Here, an objective function $f(x_i)$ depends on design variables x_i within their corresponding upper u_i and lower limits l_i. The minimisation problem should respect the boundary constraints $h(x_i)$, whether through equalities or inequalities. Figure 2.6 displays the idea behind minimising a function dependent on two variables, subject to linear constraints based on Rao's [51] explanation concerning optimisation techniques:

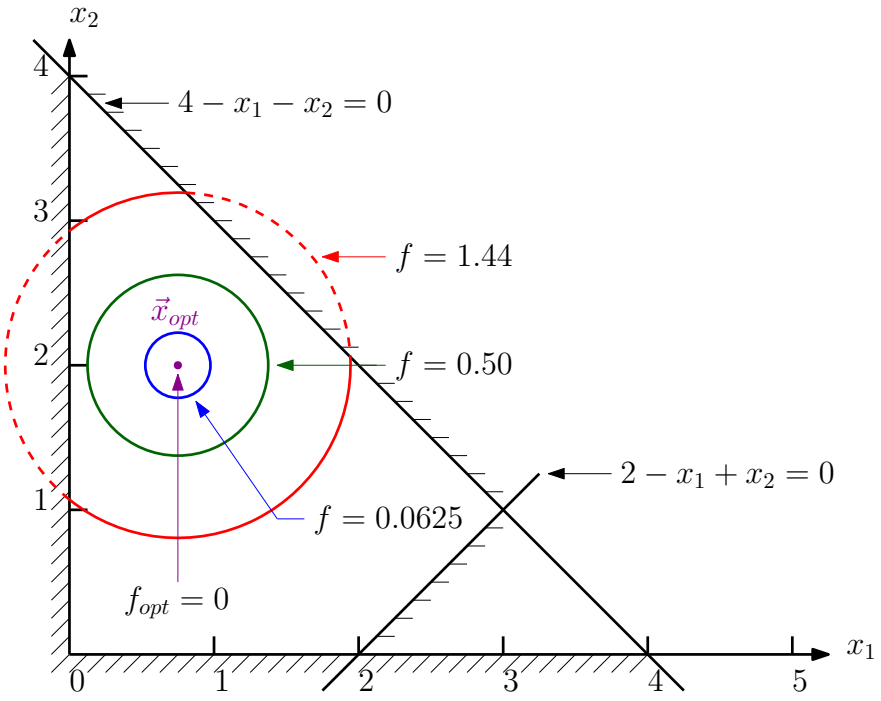

Figure 2.6. – Constrained minima under linear constraints.

In this simple example, the global optimum is contained within the boundary conditions at the point $(1, 2)$. However, depending on the problem formulation, the solution may become very complex if too many variables are involved in the problem.

When more than one function is optimised at the same time, the problem is classified as a multi-objective optimisation. Hence, new concepts known as the set of solutions are applied to a vector minimisation problem [51]. This approach does not satisfy a global optimum, but generates a set of solutions that can be considered *Pareto* optimal. By definition, a solution is in a *Pareto* set if there is no other solution that can minimise the function $f(x_i)$ without increasing another objective function $g(x_i)$. To illustrate , two polynomial functions are chosen to be minimised. Figure 2.7 shows their graphs where multiple solutions can be taken as a *Pareto* optimal set.

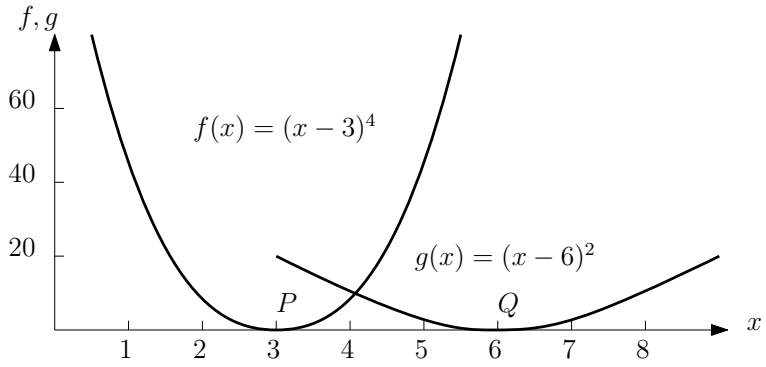

Figure 2.7. – *Pareto* optimal solutions are located within points P and Q.

Additional boundary and side constraints may add more complexity to a multi-parametric optimisation. However, a large number of independent variables x_i to be optimised at the same time may render the approach difficult or make it unfeasible to reach a solution. These problems designated by large-scale optimisation can be solved efficiently by using parallel processing, depending on the computation capabilities. For the parameter identification of hyper-viscoelastic models, the optimisation problem is formulated by minimising the mean-squared error between the model output and test results. It corresponds to a single objective function scalar depending on the variables denoted as the model parameters: C_{ij} from the general Mooney-Rivlin formulation or g_i and τ_i from the Prony series. However, in the case of the optimisation of a door seal design, several independent variables can be parametrised in an attempt to improve more than one design response. Table 2.1 lists suitable optimisation techniques that apply to several engineering problems according to references [51, 52, 53].

Table 2.1. – Optimisation techniques according to operation research methods.

Mathematical programming	**Stochastic process**	**Statistical methods**	**Modern techniques**
Calculus methods	Random search	Regression analysis	Neural networks
Nonlinear programming	Markov processes	Pattern recognition	Particle swarm
Gradient-based methods	Monte Carlo	DOE	GA

Historically, optimisation techniques come from calculus and are based on methodologies developed by Newton, Lagrange, and Cauchy. The nonlinear programming of mathematical methods is useful in determining the local minimum for large-scale variables and constrained conditions. On the other hand, stochastic processes are easily implemented, since computers have programmed functions for random number generators. These techniques are based on trial and error, or the probability of a solution eventually being reached, with no guarantee of convergence. Subsequently, statistical methods start from sampling methods similar to stochastic processes but adding notions of correlation analysis to determine empirical models or to evidence the sensibility of the objective function to certain variables. Despite being a time-consuming technique, DOE is useful to reduce the number of variables involved in a process by correlating the inputs and outputs. More recently, modern algorithms have emerged to handle complex problems faster by programming principles observed in nature, such as genetics and natural selection. Some of these optimisation techniques applied in this thesis are briefly described in the following subchapters.

2.4.1. Gradient-based methods

The optimisation techniques based on the gradient of an objective function comes from the Newton's implicit method for root finding, which expands the objective function $f(x)$ in a quadratic approximation of Taylor's series:

$$f(x) = f(x_i) + f'(x_i)(x - x_i) + \frac{1}{2}f''(x_i)(x - x_i)^2 \tag{2.163}$$

where x_i is an initial guess for the root of the expression. To find the minimum of the function, the first derivative of Equation 2.163 should be equal to zero:

$$f'(x) = f'(x_i) + f''(x_i)(x - x_i) = 0 \tag{2.164}$$

By isolating the variable x in Equation 2.164, a recurrence relation is obtained:

$$x_{i+1} = x_i + \frac{f'(x_i)}{f''(x_i)} \tag{2.165}$$

Since the derivatives of an objective function are often not available in a closed form or are difficult to differentiate, they can be approximated by the formulas:

$$f'(x) = \frac{f(x_i + \Delta x) - f(x_i - \Delta x)}{2\Delta x} \tag{2.166}$$

$$f''(x) = \frac{f(x_i + \Delta x) - 2\Delta x + f(x_i - \Delta x)}{\Delta x^2} \tag{2.167}$$

where Δx are small steps given to the implicit scheme with a convergence criterion $|f'(x)| \leq \epsilon$, for a small value of ϵ. The generalised reduced gradient (GRG) method is described by Lasdon [68] to account for multiple variables and constraints.

2.4.2. Design of Experiments (DOE)

DOE is a statistical tool that is commonly employed in industry to understand the relationship between key process inputs and outputs. For example, in a designed experiment of a machine, inputs or design parameters are intentionally modified to observe changes in the functional performance of the product. A common approach used by engineers in manufacturing companies is One-Variable-At-a-Time (OVAT), in which a single independent variable is perturbed while all other variables are unchanged [53]. However, when several design parameters can influence a certain characteristic of the product, statistical fundamentals are useful to highlight which inputs are most relevant for the observed outputs based on sampling and correlation methods. In reality, each experiment or process may be influenced by external factors that cannot be effortlessly monitored. Figure 2.8 illustrates a general process that depends on two types of inputs: controllable and uncontrollable variables.

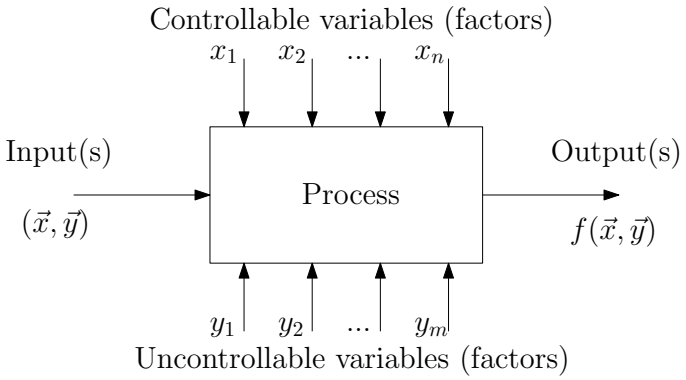

Figure 2.8. – General process with controlled and uncontrolled inputs.

By considering the general process as a seal design optimisation with several variables, it is important to define the control inputs prior to attempting the overall optimisation. Therefore, screening designs are considered to reduce the number of variables by identifying the key variables in a minimum number of experimental runs. The external or uncontrolled factors that affect the seal performance are often related to the loads, temperatures and material uncertainties on the product. Since the experiments in this work are conducted virtually, a certain number of runs are used to indicate critical scenarios for the seal performance by following the DOE tasks:

- **Hypothesis**: assumption about the influencing factors on the seal performance.
- **Experiment**: simulations conduced according to a sampling methodology.
- **Analysis**: collecting data and performing statistical analysis (correlation).
- **Interpretation**: understanding the experimental results and correlations.
- **Conclusion**: accepting or rejecting the hypothesis or establishing new scenarios.

Another important aspect of DOE is the possibility of approximating the process through surface response or meta-models [69]. If the response is correlated with certain variables, polynomial functions can be used to approximate the model outputs. However, this methodology is discarded due to the complexity of representing the non-linear response of the FEM simulations to the observed variables.

Latin Hypercube Sampling (LHS)

To conduct the designed experiments, a plan must be developed based on sampling methods. It is widely accepted that Full Factorial Designs with two-levels are used for correlations between the process and design parameters [53], by picking the upper and lower limits of the k-variables. However, the Full Factorial is represented by 2^k experiments, which very often do not allow adequate time and resources to be carried out. Since a large number of factors may influence the seal performance, other sampling technique based on the Latin Hypercube is proposed for a reduced number of experiments based on statistical judgement. Similar to other stochastic methods such as Monte Carlo, LHS consists in dividing the space formed by k-variables in a stratified and quasi-random manner by covering a design space with fewer redundancies in computational experiments. In two dimensions, LHS can be easily illustrated by the *Latin square*, name given by Leonhard Euler in his attempt to solve the 36 officer puzzle. Figure 2.9 shows on the left hand side a board in which each square has one of the first three letters from the Latin alphabet arranged so that any identical combination does not occupy the same row or column. Similarly, on the right hand side, a 3×3 chessboard formed by the two variables (x_1 and x_2) is arranged so that no two points have common values.

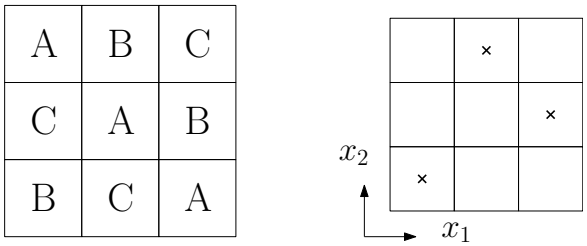

Figure 2.9. – *Latin square* example for the generalisation of the Latin hypercube.

The Latin hypercube is the generalisation of this last example to k dimensions: the sample space of each of the k variables is divided into n equiprobable intervals, and a point is chosen in each of these intervals; this generates a matrix of k columns, formed by the samples of each variable, which are then randomly permuted, generating the final sample of n vectors of k dimensions. In Chapter 5 an optimised LHS technique is employed by maximising the distance between the sampling points. For DOE with door seals simulations this technique is more suitable due to the large amount of variables considered, offering low computational cost compared to the Full Factorial.

2.4.3. Genetic Algorithms (GA)

Depending on the optimisation problem, variables can be represented by continuous or discrete values in a discontinuous and non-convex design spaces. If the previously mentioned techniques (GRG or DOE) are applied to such complex problems, convergence and computational cost aspects would possible not allow them to reach a feasible solution. Hence, GA were developed to find global optimum solutions through concepts of biological evolution based on Darwin's theory. GA differ from traditional methods since they do not require derivatives and are not simply random with respect to the problem variables. Despite the initial solutions are randomly initiated to create a population of designs, these algorithms are governed by a series of operations derived from genetics, such as:

- **Reproduction:** this selective operator sorts the solutions with above-average performance to pass their information on the next generation. Multiple copies of a variable input are added to a mating pool to be carried to the next generation based on a probability proportional to the solution fitness.
- **Crossover:** after the reproduction, this operator combines the variables from parent solutions to create new individuals for the next generation. It is expected that the resulting population will perform better than the previous. However, this effect may not be always useful for the success of the GA and, thus, the crossover has also an associated probability of occurrence to retain some characteristics from the parent solutions instead of completely changing all the variable inputs.
- **Mutation:** this last operator creates small perturbations on random variables of each newborn individual. It also depends on probability as well, and hence not all the variables will be affected by the mutation.

Given a number of generations driven by the three operators, the GA may successively yields a design solution that optimises complex multi-objective problems. However, for a small number of individuals covered by the algorithm, the global optimum may not be achieved, satisfying only the condition of a local minimum. Thus, it is recommended to use GA more than once with different initial populations to assume a convergence to the 'best' solution. In the case of parametric optimisation with a single objective function, Wolfram Mathematics' *NMinimize* algorithm employs GA by default in minimisation of numerical problems. In Chapter 6, the Non dominated Sorting Genetic Algorithm (NSGA-II) is used since it does not to privilege only the most sensitive objective function in a multi-objective design optimisation of a door seal, by constructing a *Pareto* set of feasible solutions. This exploratory technique is found implemented in ISIGHT software, which is handful for design optimisation through CAE tools. Both material and FEM models are parametrised and optimised by algorithms through their designed objective functions.

3. Material investigations

This chapter deals with experimental investigations and assumptions for the substantiation of material models used in FEM simulations for the mechanical characterization of an actual door seal. For large aircraft, structural components must be verified according to the means of compliance [70], which can be achieved through tests or analysis according to their criticality. Typically, the door sealing systems are not considered as significant structural component that contributes to the fuselage load path during flight, landing and take-off manoeuvres. However, cabin pressure, apart from being the reason for the existence of seals, is the load case that sizes most of the door structures. For the airframe certification, static and fatigue tests may require full-scale or component testing of the fuselage section. From an aerospace project perspective, these tests are the most expensive stages of development which is why the structures must be compliant with the requirements without interrupting the progress of a large test campaign. Although seals do not represent a great danger to structural integrity, the malfunctioning of a single-sealing system can cause delays in the development due to cabin decompression failure. A smaller test campaign can be conducted using sub-components by taking the door and its surrounding door structures into account to check the airtightness in a closed door configuration. However, these tests are considered only if a door mechanism philosophy is developed for the validation of the kinematics rather than specifically for the seal functionality.

Ultimately, the seal element should be tested in detail, considering the door striker and adjacent structures. Exploring different configurations, as well as cabin pressure or out-of-plane loads, would be an ideal set-up to identify the competing seal failure modes and the critical loading conditions for leakage. This approach should be applied to predict whether the analysis methods are reliable in the design of a seal, as otherwise, they do not provide a long-term solution for the development. The manufacture of seal parts is costly, as the injection moulding process for the silicone seal and its inner layers take time for each new geometry proposal. Thus, coupon tests with simple geometries are considered a relatively inexpensive way to obtain the material characteristics for further analysis consideration. The data necessary for FEM computations must be derived from simple experimental investigations and assumptions concerning the material behaviour under different loading conditions. Uniaxial, biaxial, and shear loads should be prescribed to cover the different operational conditions of a structural element. Since manufacturing processes are constantly being improved in the industry, these tests are standardised for material qualification. In general, coupon tests are sufficient to qualify new materials and provide reliable stress databases.

Figure 3.1 shows a conceptual diagram for validating the door fuselage structures that are based on the level of tests for structuring different mechanical tests.

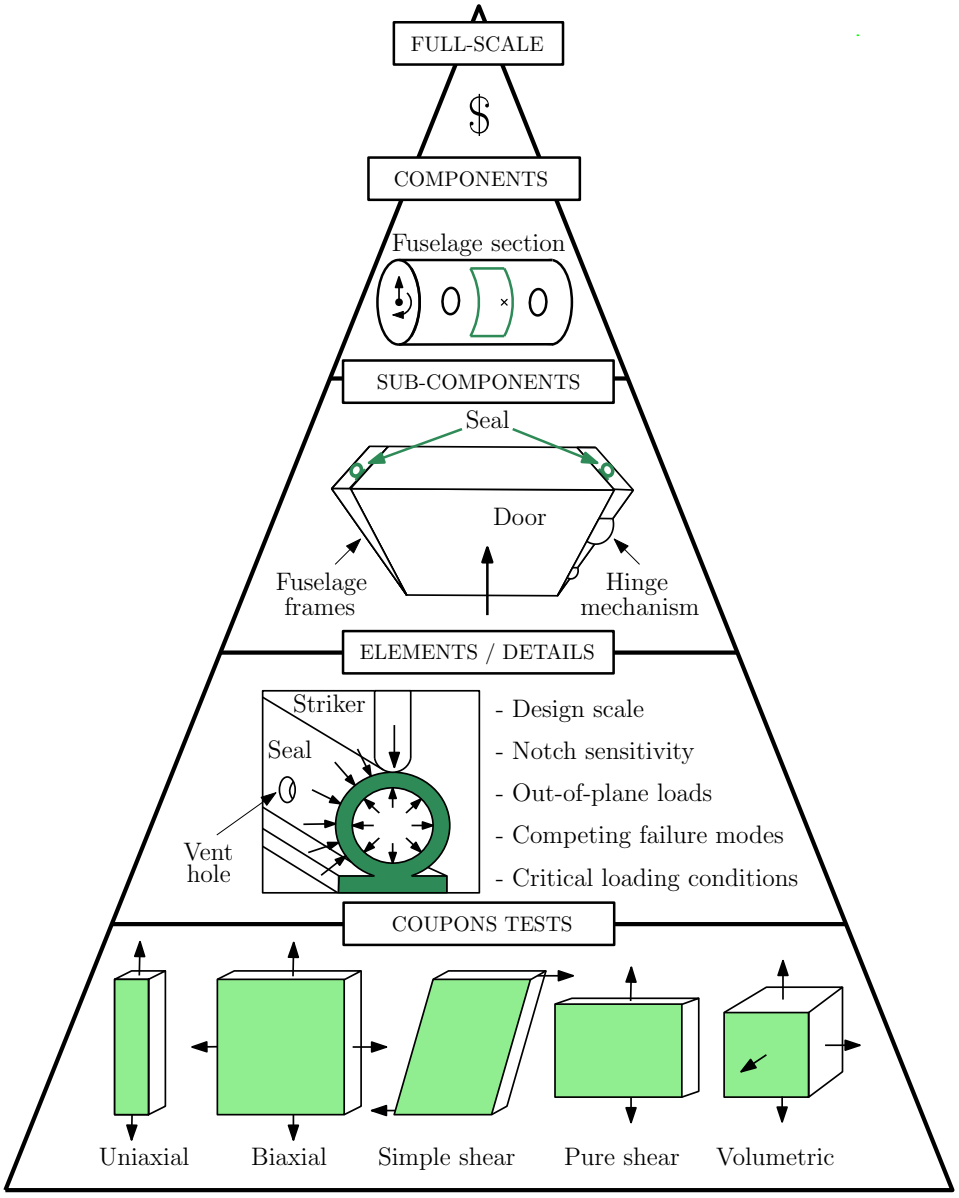

Figure 3.1. – Diagram with the test levels considered for aircraft certification.

This pyramid scheme is based on the Federal Aviation Administration (FAA) advisory [71] for composite structure tests. Even if there are no explicit guidances that establishes compliance means for elastomeric components, the standard norms for rubber provide inputs and instructions for a coupon base. The main references for this chapter are based on the standards DIN 53504 for uniaxial testing [72] and DIN 13343 for linear viscoelasticity [73].

3.1. Uniaxial coupon tests

According to the DIN 53504 standard [72], at least three specimens should be tested for the main load directions. Two sets of five samples were obtained from seals used in civil aircraft doors for quasi-static and relaxation tests. Perpendicular cuttings of the specimens, either in the longitudinal or transverse directions to the sealing line, were used to check if the fibre-reinforced seal can be simplified as an isotropic material. The coupon tests provide a data-basis for the material modelling. Previous analyses of elastomeric door seals [74] indicated that the maximum principal deflection does not exceed 50% when subjected to combined compressive and cabin pressure loadings. Therefore, a representative domain for the principal strains was considered. Uniaxial tests are conveniently chosen to identify the material parameters up to a maximum stretch of $\lambda = 1.5$, representing the ratio between the final and initial length of the sample. The sample dimensions follow the same DIN 53504 standard and are tested on a Zwick-Roell universal testing machine under ambient temperature conditions measured at 20°C, with a 500N force sensor. Figure 3.2 shows how the samples are obtained from seal sheets for mechanical tests according to the machine standards for the quasi-static and relaxation investigations for uniaxial loading conditions.

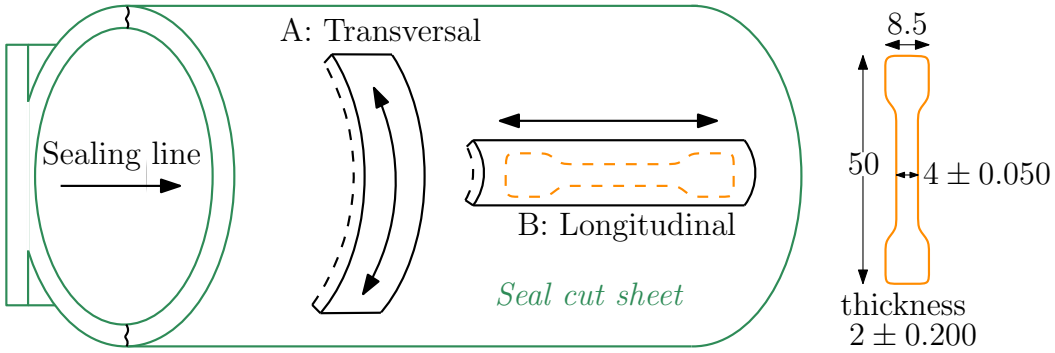

Figure 3.2. – Sample cutting directions and main dimensions in mm.

Although all of the rubber sheets are extracted from the same door seal element, a total of ten specimens are considered to cover the variability along the geometry. An average density of 1.189 g/cm^3 was measured for all specimens. It is also important to note that the seal sheets contain layers that are not solely composed of silicone rubber. The external anti-friction layer and the internal reinforcements are assumed to be homogeneous bodies. Tensile tests were performed for each specimen on a Zwick-Roell© universal testing machine at room temperature with a force sensor of 500 N and different strain rates depending on quasi-static and relaxation experiments. From a material modelling point of view, more loading conditions are recommended according to model rubber components that are based on the first two invariants [75].

3.1.1. Quasi-static loadings

Quasi-static tests are employed to characterise the elastic behaviour of the material, which is the equilibrium stress. During this process, the load endured by the specimen and the change in length are measured. To avoid viscoelastic dissipation, the process is conducted at a low strain rate for 10 different samples at a limit strain of 50%. Therefore, the specimens are stretched along their largest major axis at a constant speed of 15 mm/min until maximum stress (force) or strain (stretch) is reached. Although a minor degree of visco-elastic behaviour should be present, a good representation of the equilibrium stress is assumed. If laboratory costs and testing time are not limiting factors for the research, lower strain rates or step tests are recommended to characterise the elastic behaviour [76].

Figure 3.3 presents the stress-strain diagram for a set of average curves according to the directions extracted from the seal samples. To calculate the forces acting on the undeformed surface element, the first Piola-Kirchoff notation is used to express the uniaxial stress component P_{11}. Two curves for the longitudinal and transverse cutting directions are obtained from the average of the uniaxial tests, in addition to the total mean stress with error bars for a Confidence Interval (CI) of 95% for the specimens.

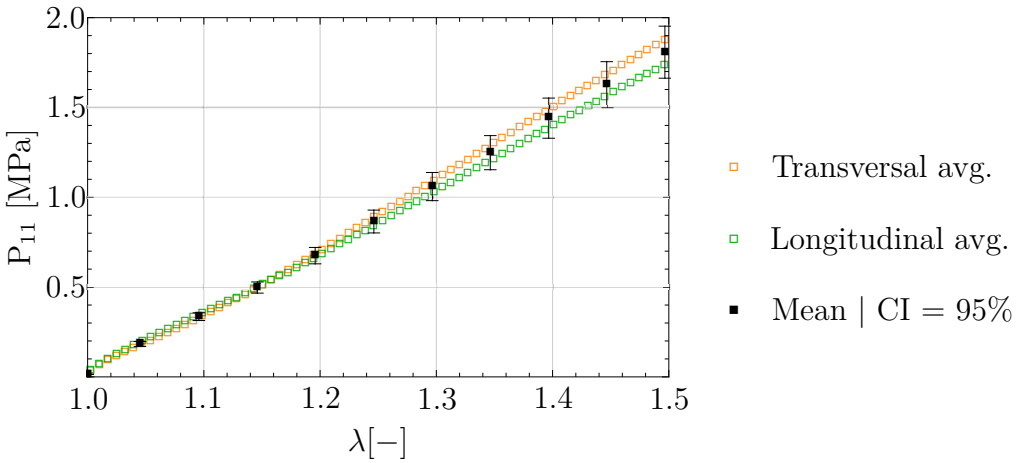

Figure 3.3. – Average stress from 2×5 samples based on the cutting direction.

These preliminary investigations show that the seal material does not exhibit a pronounced anisotropic behaviour up to stretch values of 1.5. At the maximum level of stress with a standard deviation of 0.226MPa between all 10 samples, a CI of 1.81±0.14MPa is built. Although a maximum variation of ±14.4% of the elastic behaviour is observed at the highest stress between both directions, the material of the seal is assumed to be isotropic in the considered deformation range. Therefore, the mean stress-strain curve serves as input for the parametric identification of hyperelastic models developed in Section 2.3.1. Different free energy models are considered to derive the best representation of the mechanical behaviour under large strains.

To relate the experimental studies to the formalism of continuum mechanics, the equations for the stresses are derived for the uniaxial loadings. Therefore, the prescribed displacements are represented by the single stretch variable (λ) along with the internal conditions of material incompressibility. The related deformation gradient definition is written as:

$$\mathbf{F} = \begin{pmatrix} \lambda & 0 & 0 \\ 0 & \frac{1}{\sqrt{\lambda}} & 0 \\ 0 & 0 & \frac{1}{\sqrt{\lambda}} \end{pmatrix} \tag{3.1}$$

Since the neo-Hookean (Equation 2.112) and Mooney-Rivlin (Equation 2.113) models are based on the first and second invariants of the left Cauchy-Green deformation tensor $\mathbf{B} = \mathbf{F} \cdot \mathbf{F}^T$, the invariants are given by:

$$I_1(\mathbf{B}) = \lambda^2 + \frac{2}{\lambda} \tag{3.2}$$

$$I_2(\mathbf{B}) = \frac{1}{\lambda^2} + 2\lambda \tag{3.3}$$

where the third invariant $I_3(\mathbf{B}) = \det(\mathbf{B})$ is equal to the unity for any value of deformation to keep the compatibility with the incompressibility condition at Equation 2.50. Apart from the isotropic assumption for the Equation 2.102, the uniaxial stress is obtained from the boundary value problem considering that the transversal components σ_{22} and σ_{33} are zero. Therefore, the constitutive equations in matrix form are derived for any energy function ψ that depends on the invariants I_1 and I_2:

$$\boldsymbol{\sigma} = 2\rho_0 \begin{pmatrix} \lambda^2 \frac{\partial \psi}{\partial I_1} - \frac{1}{\lambda^2} \frac{\partial \psi}{\partial I_2} & 0 & 0 \\ 0 & \frac{1}{\lambda} \frac{\partial \psi}{\partial I_1} - \lambda \frac{\partial \psi}{\partial I_2} & 0 \\ 0 & 0 & \frac{1}{\lambda} \frac{\partial \psi}{\partial I_1} - \lambda \frac{\partial \psi}{\partial I_2} \end{pmatrix} - p_H \begin{pmatrix} 1 & 0 & 0 \\ 0 & 1 & 0 \\ 0 & 0 & 1 \end{pmatrix} \tag{3.4}$$

The pressure p_H, or Lagrangian multiplier, is computed by:

$$\sigma_{22} = \sigma_{33} = 0 \implies p_H = \frac{2\rho_0}{\lambda} \left(\frac{\partial \psi}{\partial I_1} - \lambda^2 \frac{\partial \psi}{\partial I_2} \right) \tag{3.5}$$

and hence the uniaxial Cauchy stress is given by the following scalar function:

$$\sigma_{11} = 2\rho_0 \left(\lambda^2 - \frac{1}{\lambda} \right) \left[\frac{\partial \psi}{\partial I_1} + \frac{\partial \psi}{\partial I_2} \frac{1}{\lambda} \right] \tag{3.6}$$

By using the relationship in Equation 2.44, the stresses can be related to the undeformed surface element in the same way as the test results were evaluated:

$$\mathrm{P}_{11} = 2\rho_0 \left(\lambda - \frac{1}{\lambda^2} \right) \left[\frac{\partial \psi}{\partial I_1} + \frac{\partial \psi}{\partial I_2} \frac{1}{\lambda} \right] \tag{3.7}$$

Different free energy functions are investigated with respect to the test results to stipulate the best representation of the elastic behaviour of rubber. For this purpose, four forms of incompressible hyperelastic models are chosen, which include the neo-Hookean model and variants of the generalised form of Mooney-Rivlin:

- **Model 1**: neo-Hookean form with one parameter.

$$\rho_0\psi = C_{10}(I_1 - 3) \tag{3.8}$$

- **Model 2:** Mooney-Rivlin ($n = 1$) form with two parameters.

$$\rho_0\psi = C_{10}(I_1 - 3) + C_{01}(I_2 - 3) \tag{3.9}$$

- **Model 3:** Yeoh or reduced polynomial form with three parameters.

$$\rho_0\psi = C_{10}(I_1 - 3) + C_{20}(I_1 - 3)^2 + C_{30}(I_1 - 3)^3 \tag{3.10}$$

- **Model 4:** Mooney-Rivlin ($n = 2$) or polynomial form with five parameters.

$$\begin{aligned} \rho_0\psi &= C_{10}(I_1 - 3) + C_{01}(I_2 - 3) \\ &+C_{11}(I_1 - 3)(I_2 - 3) + C_{20}(I_1 - 3)^2 + C_{02}(I_2 - 3)^2 \end{aligned} \tag{3.11}$$

These models do not take the Jacobian into account, as in Equations 2.112 and 2.113, since the constitutive relations are formulated for the incompressible case. In the same way, the density only considers ρ_0. Once the free energy functions are differentiated by the invariants in Equation 3.7 to obtain the uniaxial stress, the model parameters are identified while checking if the polyconvexity condition is fulfilled. A bounded optimization problem is proposed through the minimization of the sum of mean squared errors (MSE) between the test results and the model predictions, as:

$$\text{MSE} = \frac{1}{N}\sum_{k=1}^{N}\left(\mathrm{P}_{11}^{model}(\lambda_k) - \mathrm{P}_{11}^{test}(\lambda_k)\right)^2 \tag{3.12}$$

where N is the number of data-points from the mean stress curve. To check if the model fitting is valid in a range beyond the tested strain range, Drucker's criteria in Equation 2.111 are employed considering a rate of deformation in a biaxial state $\mathbf{D}_{biaxial}$ between 0.25 and 2.5 of stretch. This consideration is described in [77], showing that the parameter identification must be fulfilled by the following inequalities for the model stability:

$$\text{tr}(\mathbf{D}_{biaxial}) > 0 \qquad \text{and} \qquad \det(\mathbf{D}_{biaxial}) > 0 \tag{3.13}$$

The results presented in this work aim to evaluate the quality of the four hyperelastic models, according to their adherence to test results and modelling complexity. Therefore, the parameter identification by the proposed minimisation problem was carried out with the nonlinear algorithm *NMinimize* for global optimisation that is available in Wolfram Mathematica® and employed when solving constrained problems [78]. This approach is described in the context of experimental studies with silicone materials to evaluate 3D printing technologies for aircraft door seal simulations [77]. Figure 3.4 shows the fitted models, which are slightly beyond the limits of the tests.

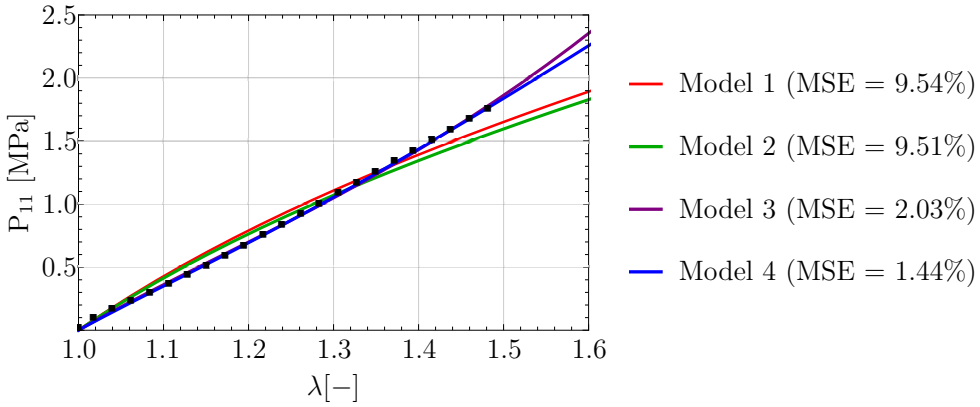

Figure 3.4. – Fitted material models with MSE values obtained with *NMinimize*.

The first two models that have a linear relationship with the invariants are not well suited to fit the curves, as they yield larger errors compared to the polynomial forms of models 3 and 4. Table 3.1 presents the identified parameters for each model.

Table 3.1. – Identified parameters for the four material models.

Model parameters in MPa	C_{10}	C_{01}	C_{11}	C_{20}	C_{02}	C_{30}
Model 1: neo-Hookean	0.782					
Model 2: Mooney-Rivlin (n=1)	0.785	-0.003				
Model 3: Yeoh (Reduced poly.)	0.649			0.200		0
Model 4: Mooney-Rivlin (n=2)	0.619	0	0	0	0.425	

The standard Mooney-Rivlin form $n = 1$ requires at least one negative parameter that is close to zero, which is not consistent with the polyconvexity conditions and has a similar response to that of the neo-Hookean model. On the other hand, the stability criteria allowed the optimization problem to reduce the number of parameters of the polynomial forms. Both the Yeoh and the second-order Mooney-Rivlin $n = 2$ models are better suited to represent the material response under quasi-static loadings. To ascertain the representativeness of the material models under large deformations, a uniaxial tension test until failure was conducted with one of the samples.

Figure 3.5 shows how the material models behave up to the limit stretch of 2.5, where the sample started to fail. Although none of the models can match the behaviour at stretches greater than 1.5, it is possible to highlight that model 4 (Mooney-Rivlin $n = 2$) is conservative enough to estimate the limit stresses under lower values of stretching. While models 1 and 2 present stress responses below the rupture point, model 3 diverges significantly from the experimentally observed behaviour. Therefore, a limit of 4MPa for the engineering stress (P_{11}) at 100% strain is established, which is equivalent to 8MPa in the true stress (σ_{11}) cf. Equation 3.6.

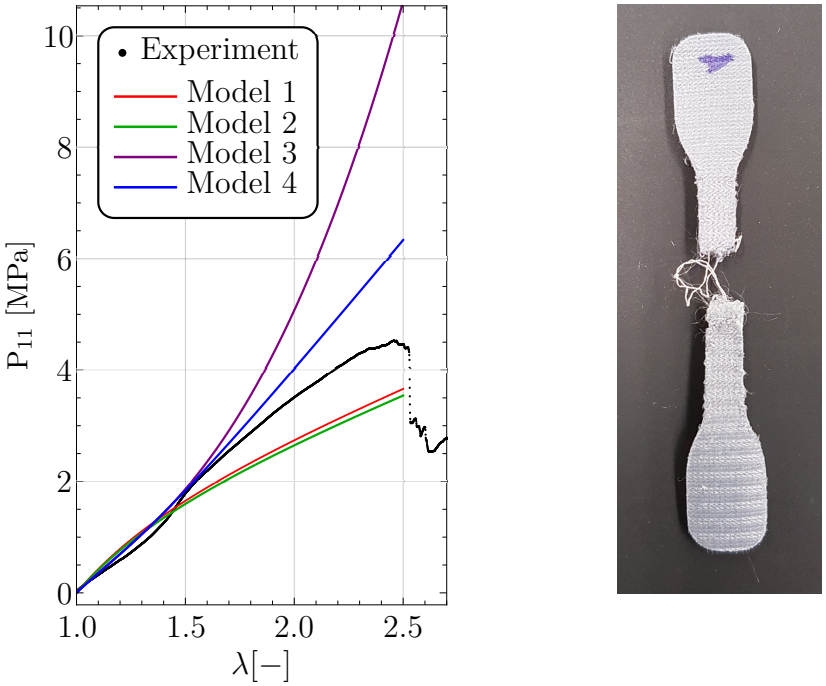

Figure 3.5. – Stress-strain results to rupture (left) based on one sample (right).

After the sample rupture, internal layers are visible, revealing that the rupture stress should correspond to a different location depending on the cutting direction. A longitudinal sample was designated for the destructive tests since transversal cutting directions presented higher stiffness. Furthermore, it is observed that the tested specimen presents a slightly attenuated elastic response compared to the originally fitted models before reaching 50% strain. Since the specimens came from new seal parts, an internal damaging process denominated as Mullins' effect might play a role in the representation of the material behaviour between the first stretch and the succeeding stretches [79]. As the FEM method of analysis proposed in Section 4 does not take the stress histories arising from one flight cycle to the next into account, the use of internal variables is purely dedicated to the viscoelastic modelling, as they are relevant for a single flight and temperature variations.

3.1.2. Relaxation process

To study the time-dependent response of seals due to a fading memory behaviour observed in elastomers [24], relaxation tests were conducted with a single sample without a previous history of loadings. No influence of the cutting directions is considered, assuming an isotropic silicone matrix for the dissipative energy modelling. Therefore, uniaxial tests were performed with a similar set-up as on the quasi-static tests, with the main difference being the initial rate of deformation and the test duration. To prescribe similar boundary conditions as in the case of door closure, an abrupt unit-step loading with a 500mm/min deformation rate of up to a 50% maximum strain is configured on the Zwick-Roell machine. After the loading, the sample is kept at a constant deformation for 12 hours to cover long-distance flights of civil aircraft. Figure 3.6 shows the experimental stress results from the relaxation process, as well as the stretch step in the course of the experiment.

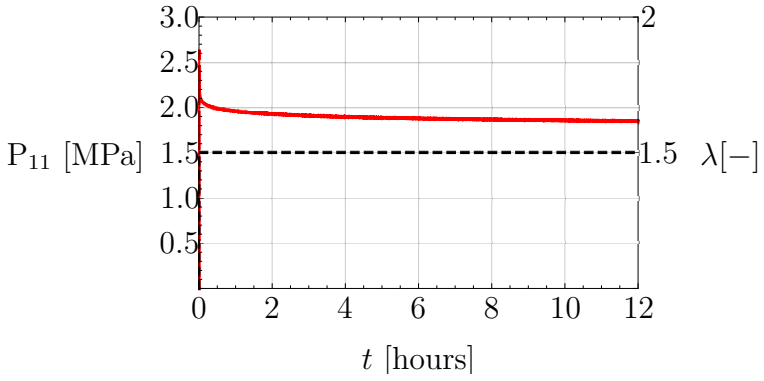

Figure 3.6. – Relaxation process with a deformation step of $\lambda = 1.5$ for 12 hours.

In this test, the maximum stress of 2.64MPa is observed, before a decrease occurs close to the equilibrium value of 1.85MPa. At the end of the test, the relaxation is not completely finished. While the coupon tests described in the previous Section 3.1.1 substantiate the choice of the hyperelastic material models in equilibrium, the relaxation process aims at identifying the viscoelastic model parameters from the chosen fading memory functional in Equation 2.117. It is assumed that the relaxation process can be approximated by a series of exponential functions from Equation 2.156. Although the initial strain rates do not correspond to the unit step function at the beginning of the experiment, the results are assumed to be representative of the instantaneous stress response. Therefore, the relaxation modulus is obtained from the normalised stress after dividing each data point by the maximum value, which implies the following dimensionless expression:

$$\frac{G(t)}{G_0} = 1 - \sum_{i=1}^{n} g_i (1 - e^{-t/\tau_i}) \tag{3.14}$$

This approach enables estimation of the viscoelastic model parameters independently of the modelling choice for the elastic behaviour. Since the stress response in Equation 2.154 is derived from a Prony series corresponding to a discrete number of Maxwell elements in parallel, a good representation of the relaxation spectrum must be verified for a minimum number of elements. By prescribing the relaxation times τ_i inside the time range of the experiment through a sequence of decades, the dimensionless parameters g_i of the normalized relaxation function is identified by minimising the error as given by Equation 3.12. This leads to a more simplified way of formulating the nonlinear optimisation problem to determine the material parameters [80]. Figure 3.7 presents the fitted series of Prony according to the pair of terms $(2 \times n)$ with the mean squared error (MSE) results found by *NMinimize*:

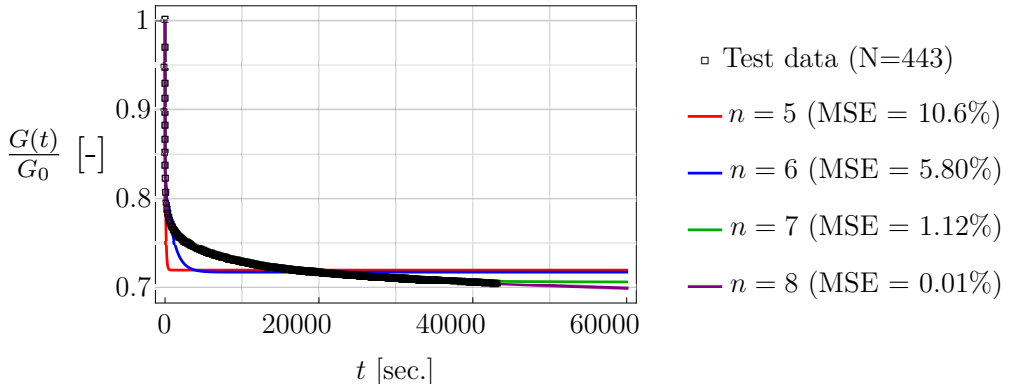

Figure 3.7. – Relaxation modulus from test data to fitted kernel functions.

Table 3.2 shows the identified coefficients for a set of predefined relaxation times:

Table 3.2. – Identified coefficients for the linear viscoelasticity models.

g_i coefficients for τ_i in sec.	τ_1 10^{-2}	τ_2 10^{-1}	τ_3 1	τ_4 10	τ_5 10^2	τ_6 10^3	τ_7 10^4	τ_8 10^5
$n = 5$	0	0.0368	0.0085	0	0.1582			
$n = 6$	0	0.0412	0.0680	0.0595	0	0.1141		
$n = 7$	0	0.0411	0.0686	0.0521	0.0499	0.0247	0.0575	
$n = 8$	0	0.0415	0.0673	0.0556	0.0423	0.0358	0.0402	0.0406

The model error is reduced as the coefficients take long relaxation times into account. Since for values of τ_i below 0.1 seconds, the dimensionless coefficients of g_i are found to be equal zero, seven Maxwell elements in parallel are sufficient according to $n = 8$. Therefore, a total of 14 parameters with relaxation times between 0.1 and 10^5 seconds are representative of the time-dependent seal modelling at ambient temperature conditions of 20°C.

3.2. Modelling assumptions

Since the tests were conducted with samples derived from a specific manufacturing process of injection moulding, other types of crosslinking or fibre reinforcements may have an impact on the mechanical behaviour [81]. Some assumptions were made about the material modelling if different silicone matrices and room temperatures were employed during the experiments. It may affect the elastic and visco-elastic response which is further investigated by the DOE for the seal analysis.

3.2.1. About the seal hardness

The relationship between the modulus of elasticity and the shore hardness of rubber [82] was initially employed to derive the obtain elastic properties of the silicone. According to Gent [83], it has a good correlation with Young's modulus estimation through the Shore A hardness, making it possible to estimate the range in which the parameters of the hyperelastic model may vary according to the specifications of the silicone from the supplier. The following equation derived by Gent is widely used for the linear modulus of rubber based on values measured with the durometer in degrees:

$$E(SH_A) = \frac{0.0981(56 + 7.62336\,SH_A)}{0.137505(254 - 2.54\,SH_A)} \qquad \text{[MPa]} \tag{3.15}$$

Figure 3.8 displays a range in which the correlation can be employed for rubber:

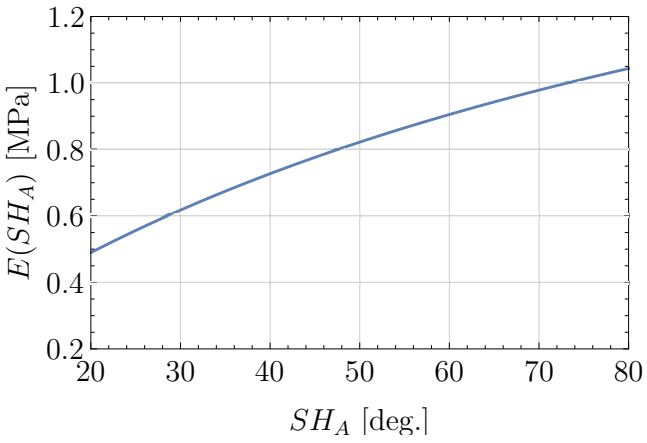

Figure 3.8. – Gent's relationship between Young's modulus and hardness.

According to the specifications of the seals used for aircraft doors, a range of SH_A from 40 to 65 degrees is used. As the requirements of cabin pressure or closing mechanisms dictate these limits, variations in the Shore hardness are a rapid and inexpensive way to characterise how stiff the design is. By measuring the shore A hardness of the samples, an average of 56 degrees was obtained, resulting in an approximated Young's modulus of 3.154 MPa from Gent's equation.

To compare the linear modulus with the material parameters of hyperelasticity models, the uniaxial stress should be derived with respect to the stretch under the assumption of small strains. The Mooney-Rivlin polynomial model with the smallest error is carried out, depending on C_{10} and C_{02}:

$$\rho_0 \psi = C_{10}(I_1 - 3) + C_{02}(I_2 - 3)^2 \tag{3.16}$$

By the definition of the first Piola-Kirchoff Equation 3.7, the uniaxial stress is written:

$$\mathrm{P}_{11} = 2C_{10}\frac{(\lambda^3 - 1)}{\lambda^2} + 4C_{02}\frac{(2\lambda + 1)\,(\lambda^3 - 1)\,(\lambda - 1)^2}{\lambda^5} \tag{3.17}$$

Differentiating it and carrying out $\lambda \to 1$, the linear expression is obtained:

$$E = \left.\frac{\mathrm{dP}_{11}}{\mathrm{d}\lambda}\right|_{\lambda=1} = \left(2C_{10}\frac{(\lambda^3 + 2)}{\lambda^3} + 4C_{02}\frac{(2\lambda^6 + 2\lambda^3 - 9\lambda^2 + 5)}{\lambda^6}\right)\Bigg|_{\lambda=1} = 6C_{10} \tag{3.18}$$

Applying the parameter identified for the model $C_{10} = 0.619\mathrm{MPa}$, the initial modulus of 3.714MPa is obtained. This result is slightly superior to that obtained using Gent's equation due to the presence of fibre reinforcements. Thus, the Equation 3.15 is modified to obtain the exact parameter $C_{10} = 0.619\mathrm{MPa}$ at $SH_A = 56$ as:

$$C_{10} = \frac{E(SH_A + 4.74)}{6} = \frac{0.356872\,SH_A + 4.31309}{95.26 - SH_A} \qquad [\mathrm{MPa}] \tag{3.19}$$

The second material parameter $C_{02} = 0.425\mathrm{MPa}$ is not present in the linear expression 3.18 and it is assumed unchanged. Figure 3.9 shows uniaxial stress curves resulting from the estimation of model parameter C_{10} and hardness range.

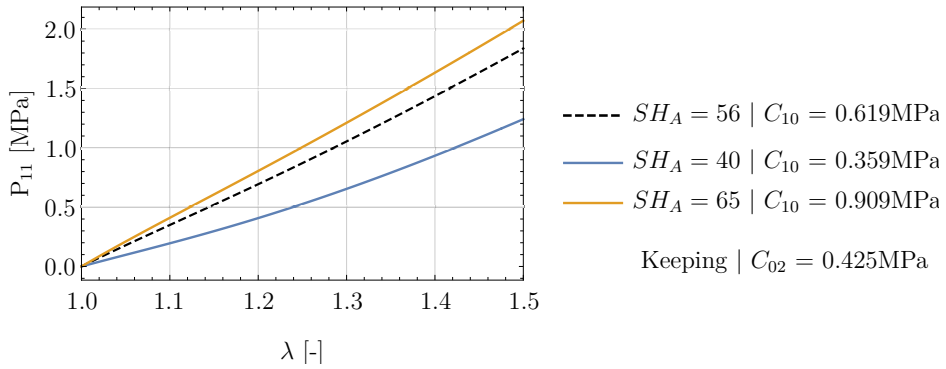

Figure 3.9. – Stress curves based on different hardness degrees for door seals.

In the analysis sections, the seal hardness is considered as a design variable to be investigated with regard to the influence of the sealing performance. An extrapolation of the parameters is comparable to studies employing the Mooney-Rivlin forms for silicone applications in the literature [84, 85, 86, 87].

3.2.2. The influence of temperature

The experimental investigations presented prior to this section are valid for the characterisation of pure mechanical loadings in ambient temperature conditions. To transfer the mechanical behaviour of the seal at room temperature to other temperatures, which are relevant for the aircraft, the WLF function in Equation 2.159 is considered to estimate the relaxation times for different temperature ranges. The constants C_1^g and C_2^g are found in practice through temperature sweep tests using a master curve fitting [26]. In view of the relevant temperature range for the seals, above the glass transition temperature it is possible to employ the 'universal' WLF constants C_1^g=17.44 and C_2^g=51.6K, which are often used due to the lack of experiments [88]. According to references on polymers and their physical properties [89, 90, 91, 92, 93], the glass transition temperature of silicone rubber is in a range of between −135°C to −120°C. In the case of atmospheric conditions relevant for civil aircraft, the lowest temperatures are approximated at −55°C in flight at altitudes of 35 000ft [94, 10] and extreme ground climates. To take the effect of the temperature on relaxation time shifting into account, a glass transition temperature of θ_g=−60°C is chosen to remain slightly bellow the limit conditions found in door seals. Thus, the values adopted for the WLF equation are C_1=6.84 and C_2=131.6°C, after calculations with Equations 2.161 and 2.160 from a reference temperature θ_0 of 20°C approximately measured during the relaxation tests. These arbitrary parameters do not deviate significantly from the experimental findings for silicone rubber in the work of Yoon and Siviour [95]. Figure 3.10 illustrates the effect on the relaxation modulus by employing the WLF function to account for the influence of temperature.

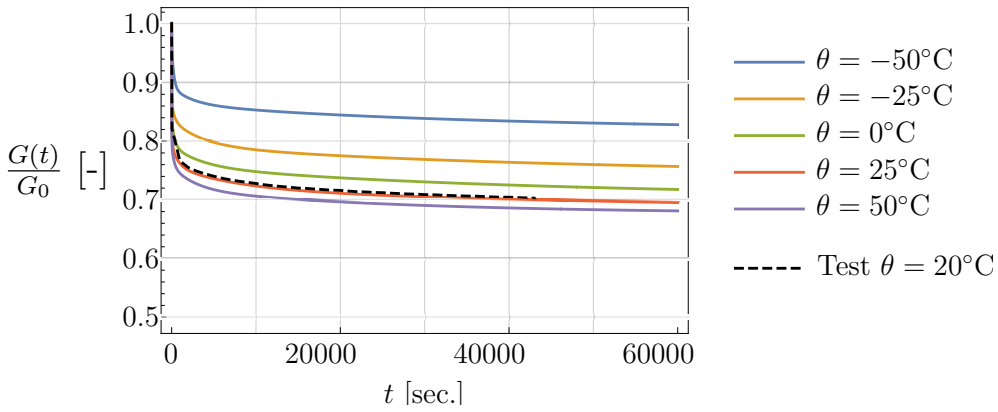

Figure 3.10. – Relaxation modulus employing the WLF shift function.

It is anticipated that the seal performance might be affected under both positive and negative temperature variations between flight cycles due to the seal relaxation time shift. Since the WLF function should be limited to $\theta_g + 100°C$ for many polymers [96], a temperature of 50°C is considered to account for hot ground conditions.

4. Seal FEM analysis

The following sections present the important FEM model inputs of an aircraft door seal design as well as the related analysis steps. For the boundary value problem with an incompressible material, a hybrid element formulation is employed for the discretisation of a concept geometry. A suitable element formulation is chosen from ABAQUS library to account for the test's representativeness and temperature dependency. To establish the minimum number of elements in the seal, a mesh convergence investigation is performed with Grid Convergence Index (GCI) criteria [97]. The analysis steps are split into mission events, such as door closure, take-off and landing, with a combination of pressurisation and manoeuvres, by providing a standard flight profile of a civil aircraft. The loads that have a direct influence on the seal system are defined based on contact interactions, prescribed displacements and distributed loads from the cabin pressurisation. In addition, the seal temperature is directly modified on each element according to ground-air-ground steps to avoid heat transfer simulations and keep a purely mechanical problem the displacement-based results.

FEM solutions have limitations, either due to convergence issues of the implicit solver or the complexity of coupling thermal and mechanical problems [98]. Nevertheless, the commercial software ABAQUS allows the problem to be split into multiple independent analysis steps, according to the physical quantities that are necessary for the solution. Specifically for seal simulations, the main advantage of the software is the application of distributed loads through the FPP interaction [5]. For the heat exchange between the cabin and atmosphere at the door contour, simplifications are made by considering a no-temperature gradient over the seal cross-section. Consequently, the solver configuration in ABAQUS can be changed between quasi-static and dynamic steps to keep convergence along the analysis, while keeping steady-state conditions for the temperature transitions. Nevertheless, the possibility of integrating the simulation sequences for multiple flight conditions using the ISIGHT tool is an important feature to set up different loadings in Chapter 5.

The seal performance is derived from pass-failure criteria for leakage based on FEM outputs, founded on contact stresses. Furthermore, other outputs such as the reaction force for section compression and the residual displacement after a creep phase are used to evaluate the design from a multi-objective perspective. To cover a larger number of design variables, 2D plane strain are assumed to reduce the calculation time for a large amount of simulations. Although the proposed methodology is applicable for straight sections of the seal, which cover the majority of a door sealing system, it is not valid for more complex 3D simulations for the corner locations [74].

4.1. Premises of the model

Regarding the 2D modelling approach for the straight sealing sections of aircraft doors, the minimum number of parts that establish a sealing interface is the seal and the striker. The design philosophy for each part may reflect how the door kinematics operates, as previously illustrated in Figure 1.2. It is often necessary to use adjacent structures, such as retainers, to stabilize hollow section seals under cabin pressure. However, reinforcing the sealing interface through seal design choices should be feasible without adding stiff components. The striker that forms part of the rigid door contour structure must compress the seal and not clash with any rigid parts of the door. For the placement of the seal, an available area of ca. 50x50mm is estimated around the door contour, given the boundaries between the frames and the skin edges. To consider a simple design whose dimensions are easily set to Computer-Aided Design (CAD), a prototype is reiterated from previous studies with FEM analysis of seals [77], as shown in Figure 4.1.

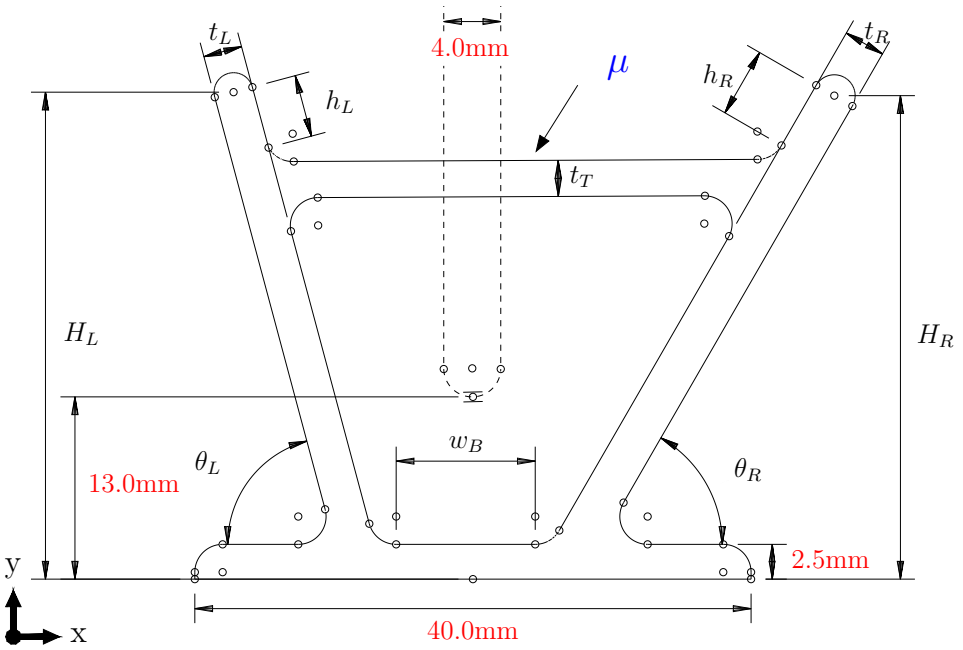

Figure 4.1. – Seal prototype (solid) and rigid striker (dashed) cross sections [77].

The striker is long enough and centred on the seal cross-section, keeping a clearance to the door skin in the nominal closed position. All of the radii transitions are set to 2mm between the seal wall along the cross-section and the hollow inflatable areas of the seal and the red dimensions added to the sketch are kept constant for all analysis sections. To operate with the initial values of a prototype, the seal design variables are conceived following the inputs in Table 4.1. These values are revised in Chapter 6 using Parametric Optimisation for the improvement of the seal performance.

Table 4.1. – Initial design values for the seal prototype.

Design parameters	Description	Initial values
t_L, t_R, t_T	Thickness (seal wall)	2.0mm
H_L, H_R	Height (seal wall)	40.0mm
h_L, h_R	Height (lip feature)	3.0mm
θ_L, θ_R	Angle (seal wall)	75°
w_B	Width (seal bottom)	12.5mm
μ	Friction coefficient	0.25

From the information provided it is apparent that an unconventional design variable has been considered, namely the coefficient of friction between the seal and striker surfaces. The way in which nondimensional variable can be changed is related to the addition of anti-adherent layers, which often do not play a structural role in the mechanical behaviour of the seal. However, it is regarded as a finishing aspect of the material design rather than a mechanical property. In Chapter 5 related to the DOE, the coefficient of friction is modified to check its influence on the FEM results.

4.1.1. Boundary conditions

The boundary conditions in the FEM model are defined relative to the seal referential, which means that the seal does not move in space. Usually, aircraft seals are located on the door's side, which in turn perform translational and rotational movements around the fuselage during opening and closing. For reasons of simplification of the prescribed displacements, it is conventionally defined that the rigid striker located on the side of the fuselage translates the door kinematics instead of the elastic seal body. For proper modelling of straight sections of the seal, plane strain conditions are important for the 2D element formulation. On the other hand, the striker is taken as a rigid body because it has a considerably higher modulus of elasticity compared to rubber. Additionally, in ABAQUS, 2D rigid parts can be created either by a meshing with lines elements or analytically using two lines and a semicircle. Due to the simplicity of the striker geometry, an analytical rigid body is preferable for the contact pairs of the surface formulation. Therefore, the relative displacements are prescribed to a single reference node where the rigid striker is connected in all degrees of freedom. The closure kinematics is specified as a movement in the y-direction of the cross-section, up to a minimum clearance of 13mm from the fixed door attachment. Further relative motions in either the x- or y-direction are given according to the flight mission events or rigging tolerances. Door displacements U_x and U_y are variable inputs, while the rotational degree of freedom is considered fixed. Therefore, a reversed local coordinate relative to the global system is placed on the striker reference node.

In addition to the prescribed displacements, contact interactions play a fundamental role in the sealing problem. From all the nonlinearities highlighted for the modelling so far that are intrinsically geometric or related to the material, the contact problem must be processed with greater care to reach an acceptable numerical solution [74]. In the case of contact between deformable bodies, the relationship between stresses and displacements may be disturbed, which affects the calculation of the tangent matrix for the implicit scheme. This leads to a gradual reduction in the integration increments, which eventually may exceed the limiting number of attempts to obtain a feasible solution. In ABAQUS, the maximum displacement and force increment criteria add more constraints to the solution [5]. For the considered seal analysis, a maximum value of 20 attempts was set, which increases the chances of getting a valid iteration. The default value in the software is 5. Another way to overcome divergence is by adding numerical damping to the solution, which is not recommended since it removes elastic energy from the system. To avoid these issues, simulations are defined with intermediate dynamic steps when static solution is not feasible.

To save some time in the solution of a contact problem, predefined pairs of surfaces are better suited than a general algorithm for surface detection. Furthermore, certain interactive features can only be explored by using a surface-to-surface algorithm, e.g. FPP, which is very important for an appropriate cabin pressurization prescription. Among the properties chosen for contact interactions, the same friction coefficient is set for all pairs of surfaces using the penalty method. Figure 4.2 displays the seal and the striker with a set of 4 surfaces used in the implementation of the boundary conditions, including the self-contact and the pressure load.

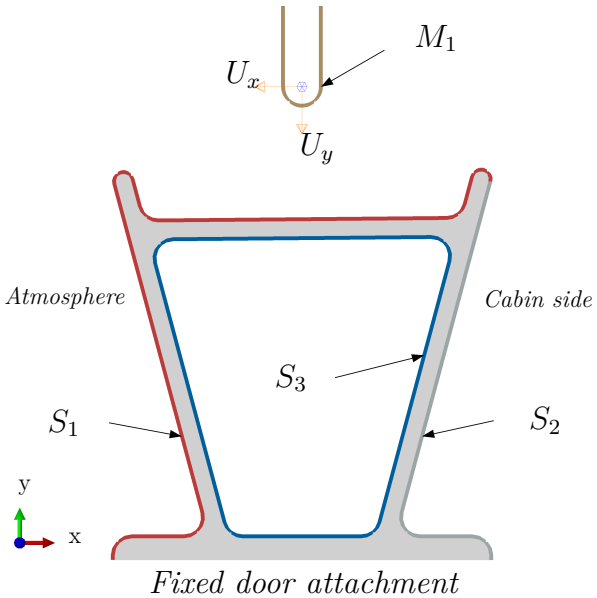

Figure 4.2. – Contact interactions with 3 slave surfaces on the seal and 1 master rigid striker surface (Pairs: $M_1 - S_1$ (FPP) and $M_1 - S_2$; Self contact: $S1$ and S_3).

The slave surfaces S_1 and S_2 are paired with the master surface of the striker M_1, while all the slave surfaces of the seal, including the inner wall S_3, have self-contact interactions. It is conventionally stipulated that the cabin side is to the right of the seal and the atmosphere to the left, while the striker reference node is placed at the centre of the semi-circle to prescribe the displacements U_x and U_y. The boundary conditions are often not applied simultaneously according to the order of the loading cases for a correct representation of the physical problem. To apply the cabin pressure, the seal must be previously compressed. It is necessary to identify the areas where the seal should be under cabin pressure. Usually, in linear problems, the distributed loads do not move or rotate. However, the sealing problem is the perfect example of nonlinearities that are even extended to the force load definition. The difficulty to apply cabin pressure to elastomeric seals has been addressed in another publication [74]. Notably, the FPP interaction is the most suitable method for the pressure application of seal problems. If the pressure is applied with the standard distributed loading method (DLOAD) the boundaries would be able to translate according to the striker boundary the between cabin and the atmosphere. Before the striker compresses the seal, it is not possible to decide, which part of the boundary surface is pressurised and which part is not, thereby rendering it difficult to assume where the pressure must be taken. Fortunately, the function behind FPP updates the loads from a known reference point and penetrates the forces from the pressure until a contact boundary on the slave surface is reached. This process occurs along each time increment to take into account the contact changes. The algorithm requires only two parameters: one is the penetration time to gradually update the interaction and the second is the magnitude.

- **Relevant aspects concerning the Fluid Pressure Penetration (FPP):**

To correctly operate with the FPP feature, the pressure loads should be applied on the external surfaces (S_1) with the negative sign rather than on the cabin area (S_2). The sign of the pressure assigns the direction in which the forces are applied. When it is positive, it orientates the distributed loads in the opposite direction to the element surface normal. If the pressure is applied from the cabin side, it must be considered positive since the gradient of pressure points to the atmosphere side. Alternatively, a negative pressure with the same magnitude is also true from the other side, accounting for the pulling forces on the atmosphere. This second option is found to be simpler, since it avoids the creation of an additional distributed load on the hollow area for the seal's inflation and works better with FPP in ABAQUS. Once the cabin pressure increases, the seal slides towards the atmosphere. When the cabin pressure is positively prescribed on the cabin side, if one element with applied pressure penetrates through the striker barrier, the algorithm applies the load over all external walls of the seal. This often leads to the false conclusion of air leakage by only reading the outputs. If loads are applied from the atmosphere side, the algorithm works as expected, creating a tractive load to the new surfaces of the elements that cross the striker contact line, while maintaining the cabin side with zero pressure.

Although FPP is a built-in feature in ABAQUS, it is only available for the general implicit analysis that provides static solutions. The need for a dynamic counterpart for the analysis was highlighted in a study of FEM simulations with elastomer seals under cabin pressure [74]. In the case of seal collapse or post-leakage scenarios, when the seal slides under the door striker, the profile does not have sufficient stiffness to remain stable. The failure mechanism by the collapse of the seal occurs during in a quick process that has no margin to reach equilibrium when the structure contact is lost. Dynamic solutions accounting for the inertia of the system are certainly needed and must incorporate pressure loads that are representative of the seal physics. Remarkably, it is possible to induce the software to carry the FPP interaction even for thermally coupled and dynamic solutions if a general static step prior to this creates the interaction. By resorting to the dynamic solution only when the sliding motion is prone to occur, it is possible to use FPP for the cabin pressurisation and save time in the simulations. The FEM model is adjusted to keep the transient material behaviour active for creep and relaxation at any stage of the simulation. Furthermore, the temperature is modified during the same steps where the pressure load is changed and it motivates the use of a multi-step analysis solution from ABAQUS to properly represent all the boundary conditions involved in the sealing problem.

4.1.2. Analysis steps

Figure 4.3 draws a flight mission profile in a timeline marking when the displacements, altitude, pressure and temperature are changed during different events.

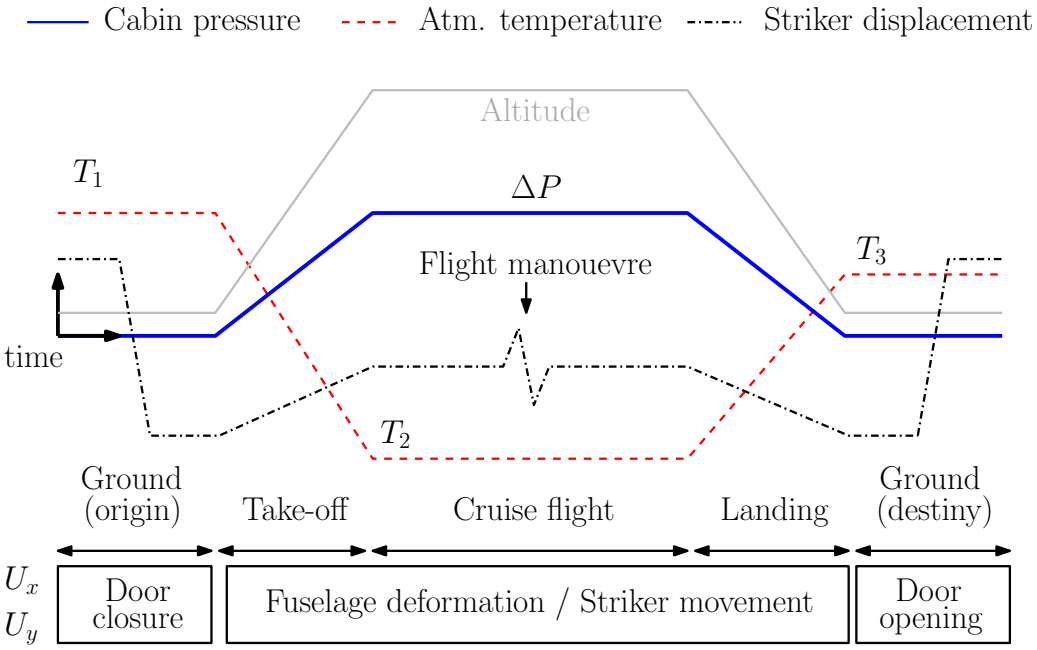

Figure 4.3. – Mission profile of a civil aircraft.

During the transition between the ground and flight, the differential pressure is applied with ramp steps according to the altitude. At the cruise altitude of 30 000ft, the cabin pressure has a set value of 470mbar, which corresponds to a ΔP value of 0.0470MPa in the unit system of the analysis [94]. Analogously, the atmospheric temperature changes during the climbing phase, although the ground origin and destination temperatures could be different. Thus, three temperature levels T_1, T_2 and T_3 are set depending on the weather conditions at sea level and high atmosphere cruising speed. Another variable affected by flight events is the relative striker position, which starts from the point of door closure and can change due to the pressurisation and during the flight manoeuvres. Depending on the fuselage stiffness and rigging tolerances, the striker displacements U_x and U_y may differ from the nominal position for each aircraft of the fleet starting from the door closure configuration. While the pressure is a defined asset for the seal system, the temperature and striker relative displacements are not simply fixed, but rather are affected by external disturbances. In Chapter 5, both temperature and displacements are provided in an acceptable range for hypothetical flight profiles.

The FEM model is built in a sequence of analysis steps to simulate the events of any given mission. It is not possible to carry out a dynamic simulation directly after a thermal-displacement coupling in ABAQUS. For this purpose, visco solutions (transient static) are added in between each step to shift between thermal and dynamic conditions. Fundamentally, visco and coupled temperature-displacement analysis are static solutions that take the time-dependent behaviour of the material for creep and relaxation into account and which are essential for applying the cabin pressure amplitude and the temperature boundary conditions, respectively. The implicit dynamic steps are necessary for the analysis sequence to overcome convergence issues when accelerations are relevant for the system response, e.g. seal collapse. Table 4.2 lists the sequence of the loading steps, as well as the time for each calculation in seconds that is integrated based on the multi-step implicit integration scheme.

Table 4.2. – Analysis sequence of a flight mission with time step durations.

#	Description	ABAQUS Step	Displacement	Temperature	Pressure	Time [s]
0	Ground	(Initial)	Created	Created		0
1	Door closure	Dynamic	Modified	Propagated		11
2	Taxiing	Visco	Propagated	Propagated	Created	600
3	Take-off	Temp.-displ.	Modified	Modified	Modified	1 800
4	Cruise	Visco	Propagated	Propagated	Propagated	18 000
5	Manoeuvre	Dynamic	Modified	Propagated	Propagated	60
6	Cruise	Visco	Propagated	Propagated	Propagated	18 000
7	Landing	Temp.-displ.	Modified	Modified	Modified	1 800
8	Taxiing	Visco	Propagated	Propagated	Propagated	600
9	Door opening	Dynamic	Modified	Propagated	Propagated	11
10	Parked	Visco	Propagated	Propagated	Propagated	1 800

The first analysis step is used to initiate the ground conditions at time zero. The dynamic phases of the analysis occur when there are large relative displacements of the striker during short time intervals, such as during door closure and opening (11s) or a flight manoeuvre event (60s). The take-off and landing phases last 30 minutes (1 800s) each and modify the pressure, temperature and relative striker displacements with amplitude ramps according to the altitude level. When the three types of loading are modified, the temperature-displacement coupling is required. Between altitude transition phases, a long flight with a cruising time of 10h (2×18 000s) is considered to be solved by the static (visco) transient response for seal relaxation. Taxiing times are approximated to 600s for ground phases, with 1 800s in total additional waiting for the aircraft parked at the end of each mission. Whenever a boundary condition is propagated, the same values are retained from previous analysis steps. As there is no history dependence from one flight to another, the analysis stresses are calculated within a standardised flight mission of 11 hours 51 minutes 22 seconds. Despite the restrictions of combinations between the analysis steps, the software allows for the transfer of the state of stress and strain even between different solutions. Additionally, the temperature results are transferred to the Gauss points even for solutions where no thermal analysis is involved for visco and dynamic steps. This is very important since the seal temperature affects the relaxation times of the selected viscoelastic model. Ideally, thermally coupled dynamic responses that allow the application of the cabin pressure with the FPP would be an effective solution for the seal analysis to cover the entire flight spectrum. However, the fully coupled thermal-stress analysis does not consider inertia effects, which are useful for the convergence of the analysis.

The proposed sequence of implicit solutions is an improvement on a previous work that used numerical approaches to overcome divergence problems regarding elastomeric door seal simulations [74]. Generally, the implicit scheme performs iterations with Newton's method to balance the equilibrium equations presented in the weak form in Section 2.2. Instead of using artificial damping parameters to reduce the residuals of the static solution, the analysis step sequences rely on the dynamic implicit scheme to reach convergence of steps 1, 5, and 9, where accelerations are relevant. According to the available dynamic implicit scheme [99], the numerical dissipation is less than 1% of the total energy. This introduces fewer errors compared to results from seal simulations where more than 6% of the total model energy was dissipated to stabilise the static analyses. If the solution is divergent in steps 3 and 7, the results are explored to predict seal failures, such as collapse and leakage. Since these steps vary the pressure load and striker displacement due to fuselage deformations, they are prone to induce seal slippage, which leads to statically unstable conditions. Section 4.3 presents the seal failure criteria for the performance evaluation of different designs. As the seal analysis is based on FEM results, output parameters such as the contact pressure (CPRESS), reaction force (RF), principal stress (S) and final displacement (U) are stored for the analysis steps 1 for door closure, 3 for take-off, 4 and 6 for cruising, 5 for manoeuvring and 10 for the parked aircraft.

4.2. Element suitability

From the identified material parameters, a single-element study is conducted to check whether the numerical solution can reproduce the relaxation test results. Table 4.3 condenses the parameters given to each FEM model.

Table 4.3. – FEM material model parameters given to ABAQUS.

Hyperelasticity Poly. ($n = 2$)	
C_{10} [MPa]	C_{02} [MPa]
0.619	0.425

Miscellaneous	
Density	Conductivity
ρ_0 [ton/mm^3]	k [W/(m.K)]
1.12E-09	1*

Visco-elasticity		**WLF**
g_i [-]	τ_i [sec.]	θ_0 [C°]
0.0415	0.1	20
0.0673	1	C_1
0.0556	10	[-]
0.0423	100	6.84
0.0358	1000	C_2
0.0402	10000	[C°]
0.0406	100000	131.6

Most of the values shown above were introduced in Chapter 3, except for of the heat conductivity (k). This parameter is required for heat exchange problems. However, since the temperature is directly prescribed for all elements, the solution of a heat transfer problem is avoided, which means that the heat conductivity plays no role in the solution. For the analysis with the FEM tool, this supplementary parameter is irrelevant and is set to 1. On the other hand, the material density (ρ_0) is converted to tons per cubic millimetre values to maintain consistency with SI units in millimetres. Given the additional conditions required for incompressible and thermally coupled models, a hybrid formulation for the hydrostatic pressure is required when the compliance parameter of the Mooney-Rivlin model is set to zero ($D_1 = 0$). For temperature, the integration points are disregarded in the numerical solution and are only used for prescribed values. In the ABAQUS element library [5], the following formulations are employed for the models featured in this work, depending on whether the problem is set up as 2D or 3D, respectively:

- **CPE4RHT:** 4-node bilinear plane strain thermally coupled quadrilateral, reduced integration, hybrid, constant pressure and hourglass control.
- **C3D8RHT:** 8-node thermally coupled brick, trilinear displacement and temperature, reduced integration, hybrid, constant pressure and hourglass control.

Both formulations have a reduced integration that automatically employs an hourglass control [100], which is a common feature for reduced integration. Although an in-depth exploration of FEM theory is not of interest to this work, it should be highlighted that this choice avoids shear and volumetric locking issues with fully-integrated elements [101].

For verification purposes with a uniaxially loaded element, a unit cube with all edges equal to 1mm and the C3D8RHT formulation is suitable for relaxation test comparisons. The boundary conditions are fixed for 3 perpendicular faces of the element in the X, Y and Z directions while in the remaining X face the displacements are prescribed according to the relaxation test presented in Section 3.1.2. Figure 4.4 shows the contour plots of displacement (U) and stress (S):

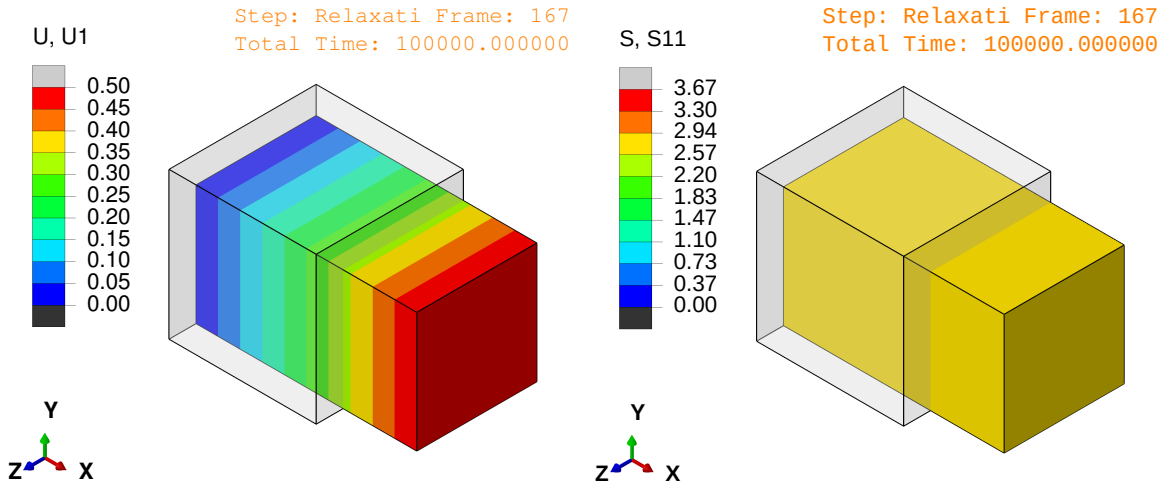

Figure 4.4. – Unit cube element outputs from the relaxation step.

The standard stress outputs from ABAQUS are given in terms of the Cauchy stress. The test results are converted into the current configuration against time on a logarithmic scale to compare with the test stress data shown in Figure 4.5:

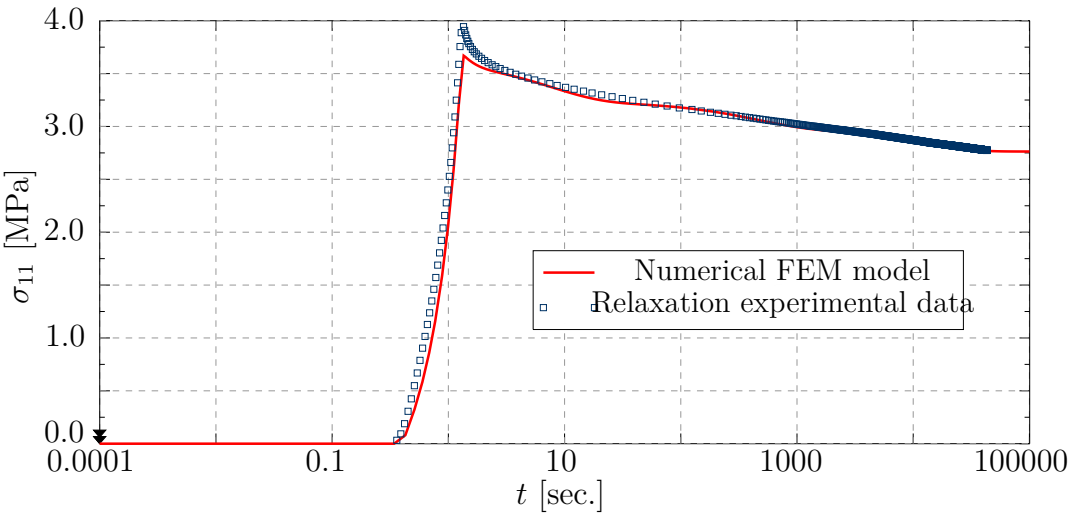

Figure 4.5. – Comparison of the stress from the FEM and relaxation test data.

Although the single-element model does not show the pronounced stress peak after the 50% strain step, the long-term response matches the test data very well. Part of this error could be due to the relatively large time increment values adopted by the solver after 0.1s, which are given by tolerances of the implicit integration scheme. Nevertheless, for seal analyses the equilibrium stresses are more important since relaxation has an effect on leakage and it is sufficient to adopt the hybrid element formulation with the application of the identified material model parameters for incompressible hyperelasticity and finite linear viscoelasticity.

Mesh convergence

For FEM modelling, it is crucial to define a discretization level based on the convergence of the model outputs. As mentioned, the seal model has a large number of nonlinearities that require attention to ensure the reliability of the numerical results. In the case of contact interactions, the mesh size influences the contact pressures, which are used for the analysis of the seal performance. A well-known procedure for grid refinement considered for numerical simulations derives from Richardson's generalised extrapolation theory [102]. The method described by Roache [97] is used to estimate the error of the FEM simulations that must converge within a sequence of three uniform element refinements. For this study, the seal cross section is continuously refined starting with two elements along the seal's thickness (grid 1), to four elements (grid 2), until it reaches eight elements (grid 3). Equation 4.1 is used to incrementally calculate the extrapolated solution (O^e) for uniform refinement step outputs (O_i) with a ratio of 2 between the edges of the elements from one grid size to the next:

$$O^e = O_i + \frac{O_{i+1} - O_i}{2^p - 1} \tag{4.1}$$

where p is the order of convergence calculated after three grid outputs:

$$p = \frac{\ln \left| \frac{O_1 - O_2}{O_2 - O_3} \right|}{\ln(2)} \tag{4.2}$$

A GCI is assigned from a consistent uniform mesh refinement procedure to verify that the output results converge to an extrapolated solution. Equation 4.3 calculates the convergence index for each step:

$$\mathrm{GCI}_i = F_s \left| \frac{O_i - O^e}{O^e} \right| \tag{4.3}$$

where the absolute error between the extrapolated solution and the outputs from a considered mesh size is multiplied by a safety factor (F_s) of 1.25. This value is recommended by the literature to estimate a confidence interval of 95% from three levels of uniform refinement. If only two grid refinements are used, a safety factor of 3 should be employed [97] to maintain acceptable CI.

Lastly, a final check of the convergence method is performed for the GCI progression based on the last two grid refinements. The output of the Equation 4.4 should be close to 1 to ensure that the solution is converging for any given FEM output:

$$r = \frac{\mathrm{CGI}_2}{\mathrm{CGI}_3} \frac{1}{2^p} \tag{4.4}$$

If this value is outside the range from 0.9 to 1.1, the extrapolated solution is not asymptotic and the element size should be further refined for comparisons. Figures 4.6 and 4.7 display the selected model outputs that are relevant for the seal analysis. The first simulation step of door closure is considered with the seal compressed up to 50% of the maximum striker displacement in the y-direction. This initial study was conducted to achieve a simple visualisation of the contact boundary in a single region of interaction between the seal and the striker. For higher door closure displacements, more contact regions are prone to appear around the lip areas.

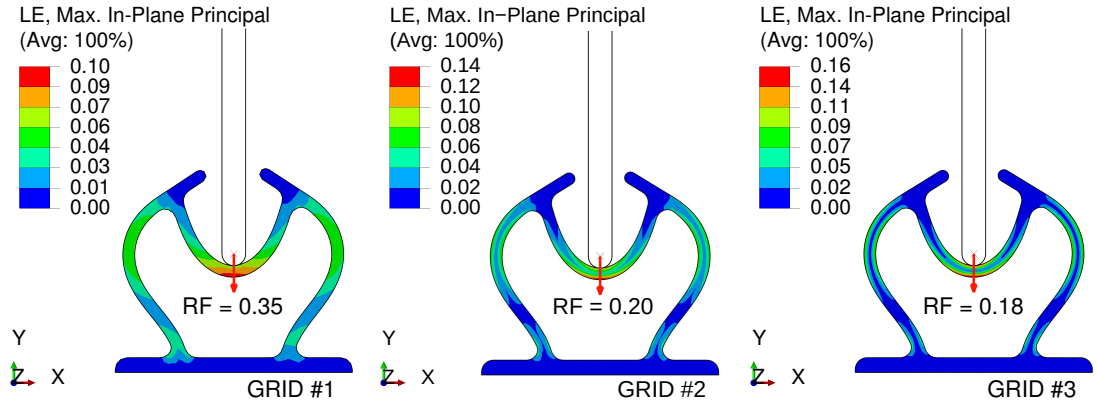

Figure 4.6. – Logarithmic strain (LE) and reaction force (RF) on the rigid striker.

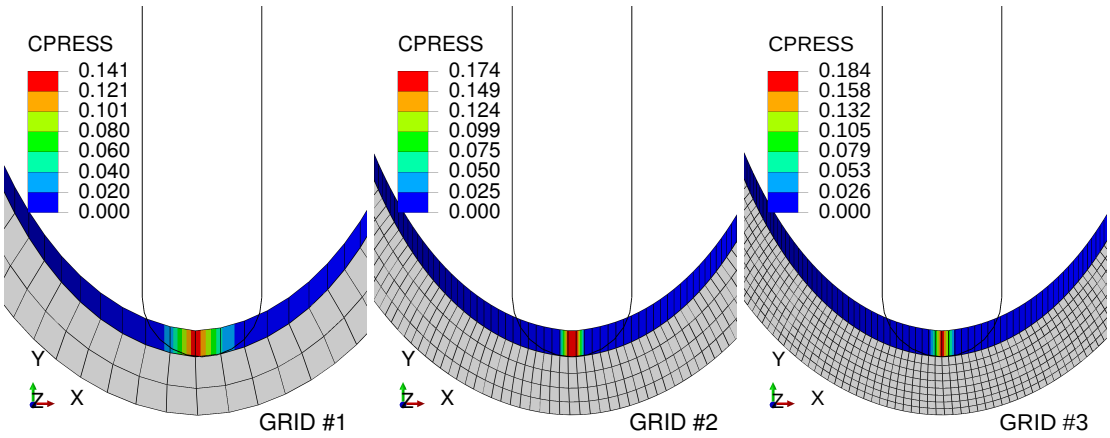

Figure 4.7. – Contact pressure (CPRESS) close-up view showing the refinement.

It is observed that the strain increases with a finer grid, while the reaction force deceases due to the better representation of the bending through the seal wall. The contact pressure output is dependent on the element area and must be well represented for small areas of interactions over the semi-circle region of the striker. By applying Richardson's extrapolation for each of the model outputs, the solution error is estimated based on the GCI calculation from a uniform element size reduction. Table 4.4 shows the convergence results for the given outputs.

Table 4.4. – Mesh convergence results from FEM outputs used for seal analysis.

Output variable	**Grid (i)**	**Edge size [mm]**	**Output value (O_i)**	**Index (GCI)**	**CGI check (r)**	**Extrapolated solution (O^e)**
Logarithmic	1	1.00	**0.10**	-		
strain	2	0.50	**0.14**	19%	**1.099**	**0.163**
LE [-]	3	0.25	**0.16**	6%		
Reaction	1	1.00	**0.35**	-		
force	2	0.50	**0.20**	14%	**0.900**	**0.177**
RF [N/mm]	3	0.25	**0.18**	2%		
Contact	1	1.00	**0.141**	-		
pressure	2	0.50	**0.174**	10%	**1.057**	**0.188**
CPRESS [MPa]	3	0.25	**0.184**	3%		

The results show that it is possible to extrapolate the solution from each model output through a uniform refinement with the three meshes. Furthermore, by taking 8 elements through the seal thickness, a maximum error of 6% should be expected, when considering the GCI of the logarithmic strain. In addition to the convergence criterion, it is reasonable to consider the calculation times involved in the simulation: 14.1 seconds for grid 1, 23.1 seconds for grid 2 and 36.8 seconds for grid 3. Due to large number of simulations required for the DOE, it is expected that the simulation time might be longer. Although the time increase of 60% is relative to grid 2, a fine mesh coming from grid 3 is considered for the subsequent seal analyses. Due to the proximity to the boundary conditions in the door attachment region, a coarser mesh is employed since it does not affect the global model outputs. Furthermore, two processors were dedicated to the CPU calculations among the 10 available physical cores. This facilitates running up to five analyses in parallel without impacting the duration of each simulation. It was observed that there is no significant gain when all cores are allocated for a single simulation. For information purposes, the FEM simulations were realised with standard job definitions on an Intel(R) Xeon(R) W-2155 CPU with a 3.30GHz processor, without GPGPU deployment for acceleration.

4.3. Seal performance

After evaluating the quality of a fine mesh based on the model outputs, the analysis criteria for seal performance investigations are derived from the simulation results. There is no consensus about how the seal analysis should properly rely on numerical modelling. While FEM is generally employed for component sizing under development, for aircraft doors, experimental validations are mandatory by certification agencies [103]. Although the criteria presented here emerge from the operational requirements for aircraft doors, seal simulations in the automotive industry have often sought to establish stable contact conditions by balancing with the handling forces induced by the cross-section compression [104]. As the finite viscoelastic model is employed to model the inelastic behaviour of the elastomer, the analysis results must be properly supported by the output result histories. Certain outputs, such as the reaction force and the safety factor for seal rupture, are directly obtained from the maximum envelope for specific simulation steps. A residual displacement criterion is further added to evaluate the relationship between the material model and different temperature conditions at the end of the flight. For the overall description of a good design, leakage and collapse are the main indicators of the efficiency of a seal. In an attempt to describe how the seal performance is obtained, the following subsections make use of graphical representations of FEM simulations under specific loading conditions. The main drivers used for the design evaluation are the closing reaction force, leakage criterion, seal collapse, stress safety factor, and residual displacement.

4.3.1. Reaction force

The reaction force required for door closure is the first indicator of the seal's performance under operating conditions. The model that is used represents the seal under plane deformation conditions with a unit thickness that is converted from N/mm to daN/m by a factor of 100, which is commonly represented in seal catalogues [105]:

$$\text{Force} = 100 \times \max\left(\text{RF}(t)\right) \qquad \left[\frac{\text{daN}}{\text{m}}\right] \tag{4.5}$$

Due to the time dependence of the forces induced by the viscoelasticity of the material, the measurements are taken within the analysis time steps 1 and 2. Since ground temperature and taxiing time before take-off may play a role in the FEM outputs, different boundary conditions must be considered. With a constant closing speed of the door, the maximum forces in the first two analysis steps are relevant for this initial evaluation of the cross-section compression. Subsequently, different mounting conditions involving the rigging tolerances of the door in the x and y directions should be considered to check their influences on the forces. With the striker positioned in its nominal position, the first studies are presented to illustrate the seal relaxation in response to different levels of ground temperatures (T_1).

Figure 4.8 shows the reaction forces measured with FEM under different temperatures between -30°C and +30°C with 20mm of seal compression after 30min:

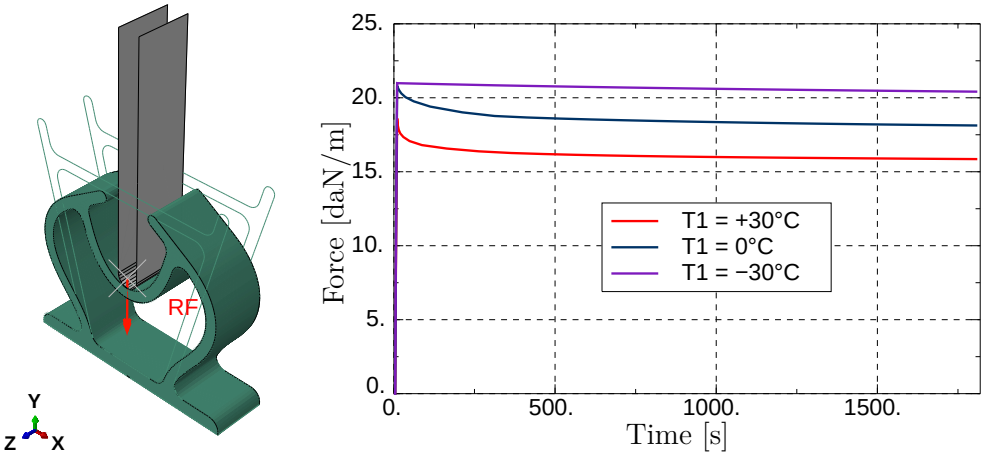

Figure 4.8. – Reaction force measured over 30min with peaks at first 10s.

The finite linear viscoelastic model presents differences in the peak values from the maximum force according to the ground temperature. Although the instantaneous elastic responses are mathematically identical for a deformation step with an infinite strain rate at any temperature, the relaxation times of the Maxwell models are directly influenced by the WLF equation. In the rheological representation of the material behaviour, the dampers of the Maxwell elements behave more viscous at lower temperatures. When considering realistic values of strain rate, the distinction due to the shift is more evident, as the reaction force peak is not solely dependent on the maximum strain value. However, it should also be noted that the maximum seal deformation is influenced by the initial rigging conditions set at step zero. Figure 4.9 shows the influence on the reaction forces when varying the rigging conditions for the same temperature of +30°C after prescribing 20mm of displacement in the y-direction.

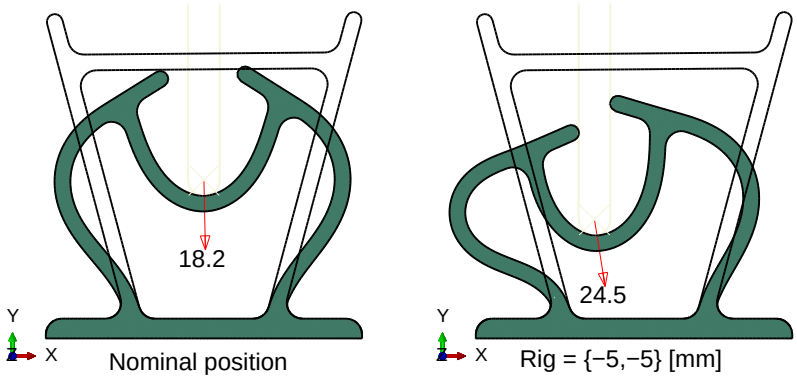

Figure 4.9. – Reaction force influences of rigging tolerances.

4.3.2. Leakage criterion

Air leakage in seals is simply presented as a qualitative measure relating differential cabin pressures and contact stresses at the seal interface. In the field of fluid-structural interaction, it is possible to model the dynamics between air particles and mechanical structures using techniques such as Coupled Euler-Lagrange (CEL) [38], which involves a high degree of complexity compared to the assumptions placed on the modelling of an elastomeric seal. Furthermore, numerical studies regarding the fluid percolation [36] of the contact area between elastic solids showed how fluid squeeze-out depends on the contact pressure distributions. Remarkably, publications about elastic leakage in aircraft seals [35, 106] display a good correlation with empirical models based on contact pressure to estimate the air leakage rate on the door surroundings. For these cases, experimental validations are necessary to fit specific parameters for the contact mechanics since the leakage depends on the interface geometry as well as on the roughness of the surfaces. Nevertheless, leakage is related to how far apart the contact surfaces or interface forces are distributed in a pressurised system. While it is valid to check whether leakage occurs due to a lack of contact between the striker and seal over the FEM result history, it is necessary to establish a continuous measure of leakage-related performance to judge different design solutions. Therefore, the following dimensionless index based on contact pressure (CPRESS) is employed to gauge leakage between flight analysis steps 3 to 7:

$$\text{Leakage} = \begin{cases} \max \left| \frac{\text{PPRESS}(t)}{\text{CPRESS}(t)} \right| & \text{for} \quad |\text{PPRESS}(t)| \leq \text{CPRESS}(t) \\ 1 & \text{for} \quad |\text{PPRESS}(t)| > \text{CPRESS}(t) \end{cases} \tag{4.6}$$

where PPRESS is the FPP output that corresponds to the differential pressure of the cabin assigned to the FEM model. Similar to the reaction force, the leakage criterion is evaluated using the entire history of the simulation results. The values obtained for this performance parameter vary in a range between 0 and 1 and are 1 when the contact stress equals the cabin pressure. Eventually, when the contact pressures are lower than the cabin pressure, or are zero, the leakage is limited to the value of 1 as well. This criterion is also related to the seal collapse check in which the seal is unable to recover its contact with the striker. The purpose of relating contact and fluid pressure works as an indirect measure of leakage, as it is not directly converted to airflow rates. Thus, the maximum leakage value is used as a performance quality parameter throughout the different flight stages (take-off, cruise, manoeuvres and landing). An operation in terms of absolute values is used to normalise the cabin pressure applied negatively on the atmosphere side. The leakage criteria are influenced by rigging tolerances, relative striker displacements, the coefficient of friction, the mechanical properties of the seal, as well as the temperatures before and during the flight. The following sequence of figures serves to illustrate the leakage criteria evaluation by taking the pressure loads against contact pressure within the analysis history into account.

Figure 4.10 presents the initial states in which the differential pressure starts increasing, thereby creating a gradient between the atmosphere and cabin environments. Here, some simplifications were made by taking a fixed displacement of the striker at the nominal position without influences from the fuselage deformation. The temperature is taken as +20°C while the friction coefficient is defined as 0.2. In this instance, it is noticeable that the ratio between PPRESS and CPRESS is low, since the cabin pressure is only 0.008MPa, resulting in a leakage index of 0.034.

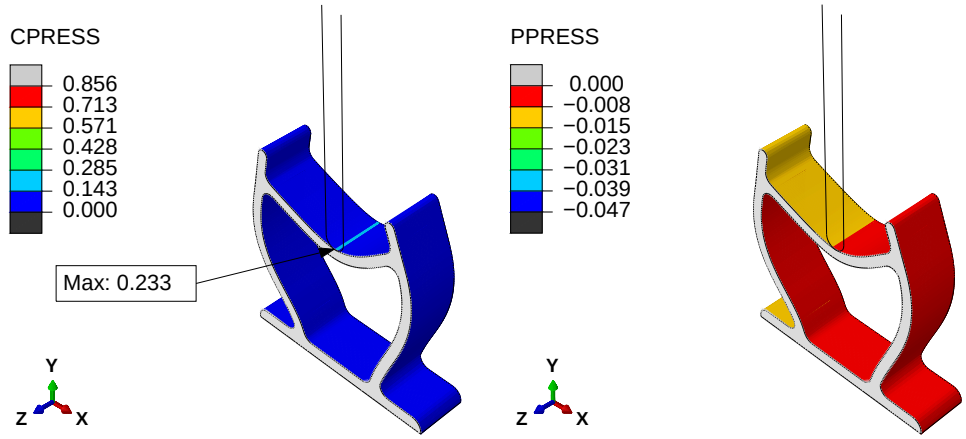

Figure 4.10. – First instants after the cabin pressure starts to increase.

Figure 4.11 shows the seal pressurised up to the value of $\Delta P = 0.047$MPa. Due to the design choice of an inflatable seal, it benefits from the pressure inside its hollow section to increase the contact forces. Remarkably, it can be seen that the seal has slipped in the negative x direction, which results in a redistribution of the pressure load carried out by the FPP interaction. Although the contact pressures have increased in the final increment, the last measured leakage index increases to 0.054.

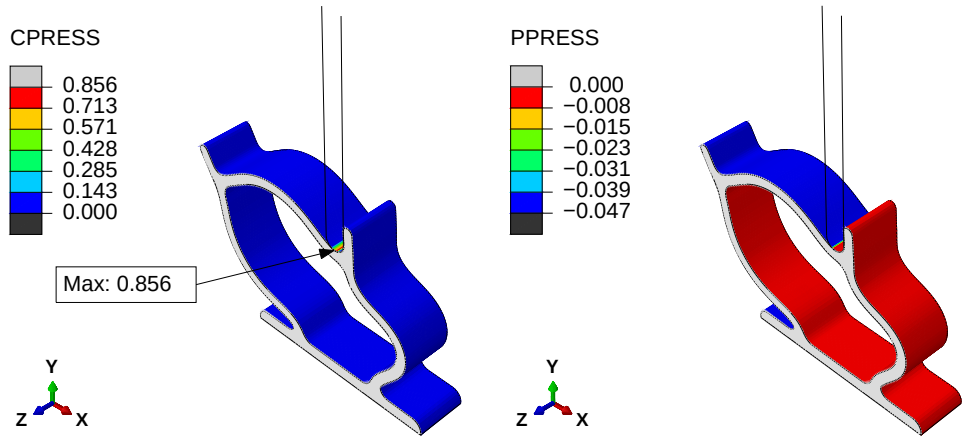

Figure 4.11. – Cabin pressure that is reached with the maximum differential.

Given the sequence of events in a standard mission profile, the aircraft goes through phases of cruising and manoeuvres as presented in Table 4.2. If the seal does not fail during the altitude gain phase as considered in previous studies with hyperelastic modelling [74], air leakage may either increase by seal relaxation [35, 106] or by relative displacements of the striker/fuselage. Therefore, it is necessary to monitor the leakage index during subsequent flight steps after the maximum cabin pressurisation is reached to evaluate the performance of the design. Fortunately, the selected geometry has lip features placed on both sides of the profile to block lateral displacement of the seal at the section boundary. However, Figure 4.12 shows that it is often not possible to block the seal sliding, which results in a drastic loss of contact pressure. At the maximum cabin pressure, the leakage index reaches a value of 0.231 up to the point where it is still in contact with the striker interface. In this example, the seal is pushed outboard - into the atmosphere side - by the pressure load, which can be triggered by the striker movement or the stiffness loss from the seal.

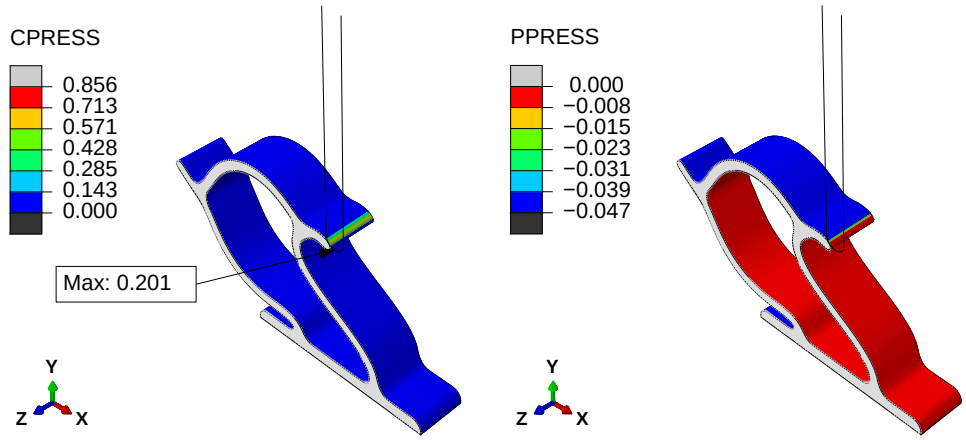

Figure 4.12. – Seal profile (about to collapse) that is part of a leakage scenario.

After this point, the seal cross-section may completely lose contact with the striker. In this case, the leakage index reaches the maximum value of 1 according to Equation 4.8. The leaking mechanism can be triggered at different flight stages such as climbing, cruising and manoeuvring. As previously stated, this criterion is not absolute for measuring the air flowing through sealing sections as fluid leakage involves tribology and fluid-dynamics and a good correlation of the predicted leakage with experimental results should be verified. Nevertheless, the proposed leakage index is an accurate qualitative measure to determine the effect of loading conditions on seal performance. Additionally, different design solutions should be comparable to the smallest leakage index under identical conditions. Usually, binary criteria, such as pass or fail results, can be applied to sensitivity studies in DOE. However, a continuous measure of the leakage criterion is generally recommended for multi-objective optimisation techniques explained in Section 6.

4.3.3. Seal collapse

The next condition to evaluate the performance of the seal is directly related to the previously described criterion. When the seal completely loses its ability to maintain contact with the striking interface, the seal cross section flips out to the atmospheric side and may no longer return to its compressed configuration. To quantify this, the seal's overall contact pressures are measured again. If the pair of master and slave surfaces are non-existent and the seal has self-contact with its external surfaces, a flag is assigned to the seal condition as:

$$\text{Collapse} = \begin{cases} 0 & \text{for} \quad \text{CPRESS}(t) \geq 0 \in M_1 - S_1 \\ 1 & \text{for} \quad \text{CPRESS}(t) > 0 \in S_1 - S_1 \end{cases} \tag{4.7}$$

In contrast to the leakage index, this criterion is a binary definition of seal collapse. The self-contact measurements of the slave surface of the seal S_1 can be distinguished from the interactions with the master surface of the striker M_1. Furthermore, due to the definition of the boundary conditions for applying FPP, the differential pressure is not distributed to the contact surfaces of the cabin side S_2. As it is complex to evaluate how the seal behaves due to dynamic interactions between the air and structure, some limitations are imposed on the problem after the collapse. A compromise that was found to keep some realistic boundary conditions involves restricting the distributed loads to surfaces located in the atmosphere region to simplify the conditions written in equation 4.7. Once contact is lost, the seal tends to move towards the atmosphere side under the resulting pressure force. Ultimately, it results in a self-contact under stable conditions no longer maintained by the striker. This verification in turn is simpler than that presented for design optimisation studies [74] that rely on the FEM nodal displacement results of the cross-section of the seal. Figure 4.13 displays the first condition to be verified for seal collapse by the complete loss of contact with the striker.

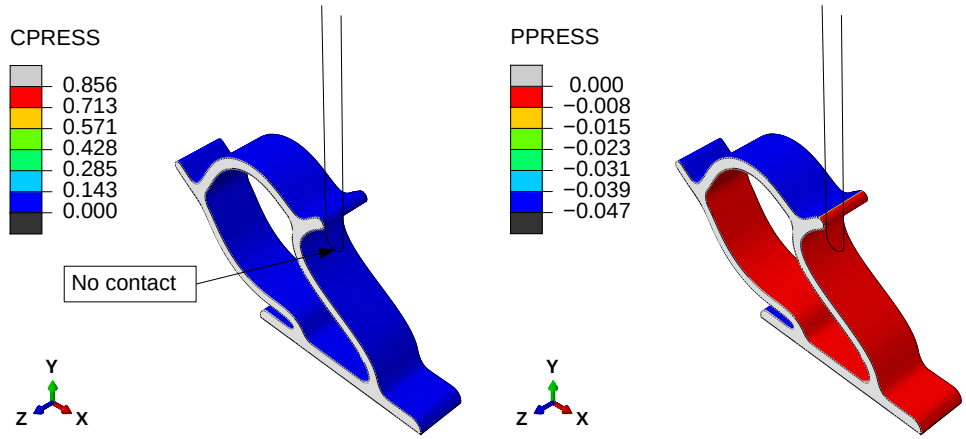

Figure 4.13. – First instants of the seal without contact with the striker.

This first verification sets the leakage index to 1, while from the analysis history it is possible to check whether the seal touches itself after contact loss. Figure 4.14 illustrates the self-contact of the external seal surfaces:

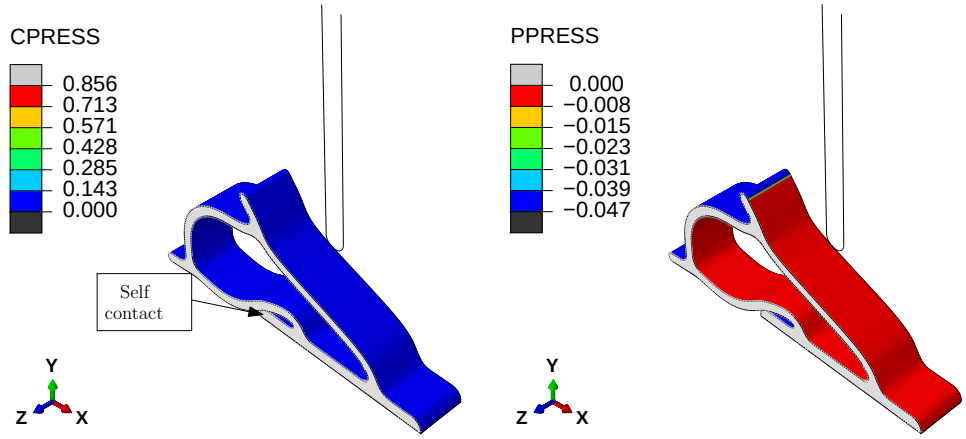

Figure 4.14. – Fully collapsed seal in an irreversible configuration.

Although this condition can be evaluated in other ways, it is easier to verify the collapse with contact outputs from the FEM model. It is observed that the pressure penetration (PPRESS) is limited to the S_1 surfaces, leading to similar collapse configurations. This behaviour is independent of the variables considered for the model, from the boundary conditions to different design solutions.

4.3.4. Safety factor

In a static stress analysis, it is very common to apply safety factors to avoid the failure of structural components under limited conditions. Based on the experimental results of tensile tests, the stress limit of the elastomer for the failure of $\mathrm{S}_{lim} = 8\mathrm{MPa}$ was estimated . Although such values are estimated for tensile stresses, an identical value for compression is assumed for the calculation of a safety factor. Therefore, the following expression is defined for the safety factor:

$$\mathrm{Safety} = 1 - \frac{\max|\mathrm{S}(t)|}{\mathrm{S}_{lim}} \tag{4.8}$$

where S_{lim} is the absolute maximum principal stress, according to the Cauchy stress computed by ABAQUS. A safety factor based on stresses should be positive for any combination of loads: compression, pressurisation, and temperature. If a negative value is reached, it indicates that the seal could be jeopardized after a critical loading scenario. From an excessive compression of the seal cross-section during the ground steps to an event of seal collapse during flight events, the safety factor is monitored over the complete stress history of the FEM simulations.

Figure 4.15 shows the maximum stresses belonging to two different scenarios, involving the critical scenario after the seal collapse. On the left side of the figure the safety factor is 84.8%, whereas on the right side it has a value of 49.1%.

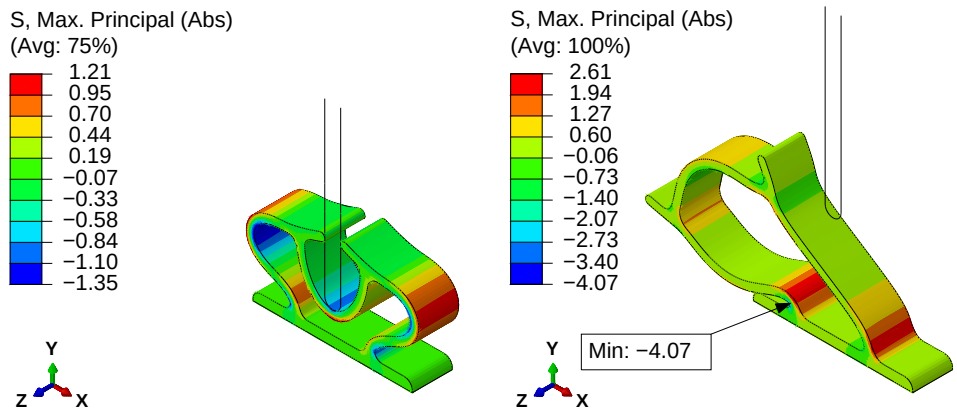

Figure 4.15. – Two stress measurements from for safety evaluation.

Remarkably, it is evidenced that lower safety factors correlate with the collapse occurrences based on DOE in Chapter 5. In this case, by restricting the seal collapse it is possible to cover the risks of damage to the seal. Thus, the safety factor is not considered for design improvements in Chapter 6.

4.3.5. Residual displacement

Residual displacement after door opening is a measurement that can influence the seal performance between one flight and another. By a creeping process after landing and take-off, in addition to the temperature on the ground, the seal response can be impaired due to the viscoelastic behaviour of the material. If the seal geometry does not return to its original configuration, there is a reduction in the closing reaction forces and consequently a risk of leakage due to the loss of contact pressure. The pre-deformed configuration of the seal is dependent on the previous flight. However, according to the FEM model assumptions, no relation between the stress histories of sequential flight missions is considered. Nevertheless, the final displacement of the seal is globally measurable from the last time (t_f) at the end of each simulation for comparison purposes between different FEM model input variables as:

$$\text{Residual} = \max\left[\text{U}(t_f)\right] \tag{4.9}$$

The ABAQUS outputs of the displacement magnitude are denoted as U for the nodal displacements. Thus, for all elements representing the seal geometry, the maximum values are measured for studies involving DOE, especially for the relative motion of the striker and temperature levels on the ground and in flight.

Figure 4.16 presents two deformed configurations at the maximum displacement during cruise conditions and the last increment after door opening for the seal relaxation. An undeformed frame from the beginning of the analysis is kept to show the differences between the displacement-based solutions of the FEM. The maximum residual displacement of 1.17mm takes place at the atmosphere wall, showing that pressure loads play an important role in the history of the analysis results.

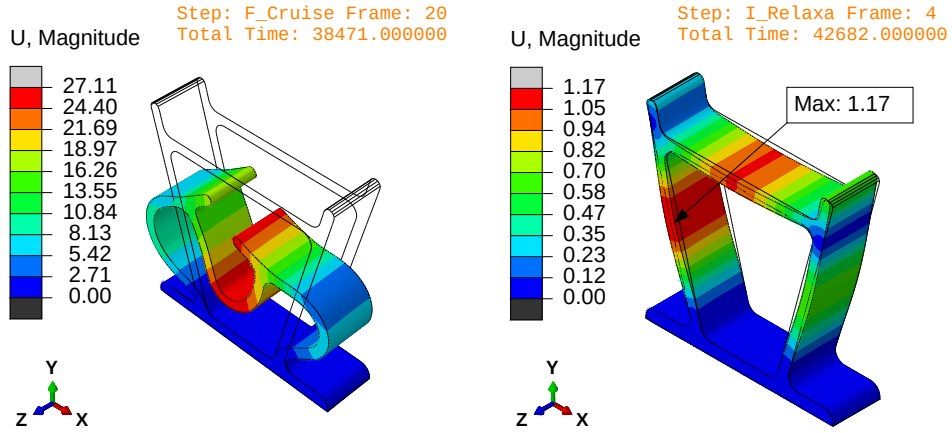

Figure 4.16. – Residual displacement due to creeping process.

Even though the model outputs for the displacements in a sequence of flight events are relevant for the overall performance, these results are not used for the Parametric Optimisation of the seal design in Chapter 6.

4.4. Summary of seal performance analysis

Five indicators related to a seal's performance were defined and can be evaluated using the FEM model outputs. Table 4.5 summarises their applicability to the DOE and Parametric Optimisation tasks in the following chapters.

Table 4.5. – Seal performance indicators summary for the next chapters.

Seal performance summary				Chapter application	
Notation	**Subsection**	**Units**	**FEM Ouputs**	**DOE [5]**	**OPT [6]**
Force	4.3.1	[daN/m]	RF	✓	✓
Leakage	4.3.2	[-]	PPRESS, CPRESS	✓	✓
Collapse	4.3.3	[-]	CPRESS	✓	✓
Safety	4.3.4	[-]	S	✓	
Residual	4.3.5	[mm]	U	✓	

5. Design of Experiments

DOE is a method that aims to understand the relationship between the inputs and outputs of an observable system through statistical concepts. The usual approach starts from an experimental strategy of combining influencing design factors [43] to highlight the variables that influence on the measurements. In some instances, DOE can be used as an optimisation tool to search for the best candidates by extensively testing the outputs of the system for different design parameters. However, in this thesis, DOE was primarily used to determine which variables influence the five performance indicators in Table 4.5. As each FEM simulation is a controllable and measurable experiment, the conceptual seal design is evaluated under different conditions and thermal and mechanical loadings, as well as dimensional and material tolerances, must be adjusted for multiple simulations.

From a range of hypothetical scenarios, the seal model inputs are modified according to the aircraft door operation limits. In total, 11 inputs are considered relevant for the five performance indicators presented in the previous section. Three temperatures (T_1, T_2 and T_3) are set independently to simulate different start/destination flight missions with altitude temperature variations. A reasonable range between -40°C and +40°C for ground conditions (T_1 and T_3) and between -50°C and -12°C for flight stages (T_2) is considered according to the international atmosphere standards [94]. Since the mechanical properties are affected by the manufacturing process, a deviation of ± 5 from the reference Shore hardness (SH_A) of 56 is proposed according to the model assumptions in Section 3.2 to adapt the hyperelastic parameters of the material model. Furthermore, surface finishing and external factors for the coating layers of the seal are important for the system stability and thus, a second material/design input variable is related to the coefficient of friction (μ), which is roughly estimated in a range from 0.1 to 0.4 for the envisaged simulations.

By taking the simulation steps with relative displacements into account, the striker position in the x and y directions should be modified for both ground and flight events, such as pressurisation and manoeuvrers. Based on global assumptions of fuselage deformation and assembly tolerances, three different types of rigid body offsets are chosen for the striker reference node. At step 0, the initial striker position is created based on the maximum rigging tolerances from the door to the fuselage cut-out. A variation of $\pm$4mm from the nominal position is assumed for study purposes of the rigging, as previously presented for the reaction force in Figure 4.9, and also to verify any correlation with important performance indicators such as leakage and collapse. Denoting the rigging tolerances, two variables R_x and R_y are assigned to the DOE.

Afterwards, the prescribed displacements of the striker are modified along with door closure, cabin pressurisation, and flight manoeuvre steps as presented in Table 4.2. It is assumed that the door kinematics in step 1 is identical for all simulations with a closure displacement of $C_y = 30$mm respective to the reference node of the striker, as shown in Figure 4.2. The only variation in the seal compression up to step 2 is a consequence of the assembly tolerances in step 0. After the start of the flight events in step 3, the superposition of the fuselage deformations by the pressurisation and flight manoeuvre steps allows for the definition of four more independent inputs for displacement. The first two consist of the relative deformation of the door cut-outs, solely due to the pressure loads P_x and P_y. Since an important counterpart of the running loads along the fuselage sections is affected by flight manoeuvrers, the relative displacements are not only driven by the cabin pressurisation. For this purpose, the additional interface movements M_x and M_y are considered in step 5. Therefore, the displacements U_x and U_y relative to the striker position are summed by each step through the operations:

$$U_x = R_x + P_x + M_x \tag{5.1}$$

$$U_y = R_y + P_y + M_y + C_y \tag{5.2}$$

Each sub-input increases linearly by a ramp function up to its end value. Until the (middle) step 5, the striker position is established by combining all types of displacements. From this point, the relative displacement is reflected back to the previous configurations, returning to the cruise, landing, and door opening. Global FEM models of the fuselage are usually able to predict the maximum displacements on the door surroundings, by the envelope of limit loading conditions. Some maximum and minimum values are proposed according to technical references for door cut-outs in airframe structures [107]. Table 5.1 displays the ranges of the 11 input variables for the DOE:

Table 5.1. – Maximum and minimum ranges of the design matrix for the DOE.

Input	**Rig. [mm]**		**Striker disp. [mm]**				**Mat. [-]**		**Temp. [°C]**		
	R_x	R_y	P_x	P_y	M_x	M_y	SH_A	μ	T_1	T_2	T_3
Maximum	4.0	4.0	7.0	4.0	8.0	3.0	61	0.4	40	-12	40
Minimum	-4.0	-4.0	0.0	0.0	-5.0	-4.0	51	0.1	-40	-50	-40

The range of inputs is crucial for defining a strategy for the computational experiments. Each experiment should contain at least one factor distinct from another model setup, to characterise the influence of the performance indicators from the FEM outputs. Sampling tools for the experiments are very important to establish systematic calculations for the DOE with regard to the FEM simulations.

For convenience, the native tool ISIGHT [108] from SIMULA was used, since it permits integration with ABAQUS, which allows the user to parametrise the FEM model inputs and outputs. Figure 5.1 displays the simulation flow through the components for the pre-processing of CAE inputs and the post-processing of FEM outputs.

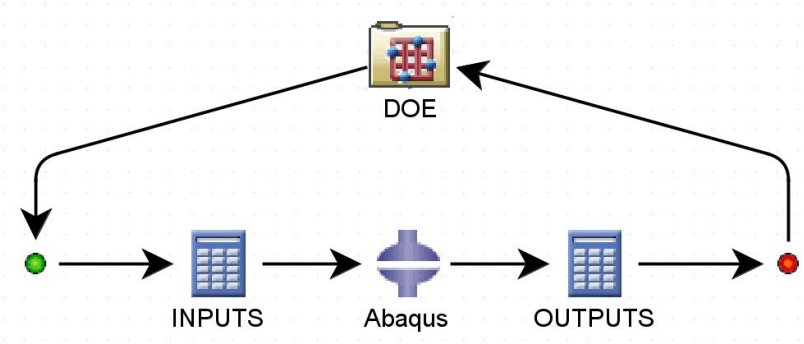

Figure 5.1. – Process components in the ISIGHT interface for the DOE.

Five performance indicators were obtained for each run by post-processing the models' outputs as presented in Subsection 4.3. In this chapter, a sequence of 500 simulations is proposed by using the Optimal Latin Hypercube technique to generate the inputs for the seal analyses. The design performance in a DOE was evaluated once the set of simulations was completed by assessing the number of failed runs with regard to leakage and collapse. Since the DOE module builds a database for further statistical analysis, Spearman's rank correlation [44] was calculated between the 11 model inputs and the 5 outputs describing the seal performance. The main objective was to verify which variables are relevant to further improve the seal design with the help of optimisation techniques. In Chapter 6, the DOE is recalled for comparisons between the initial design and the optimised seal geometry. The alternative workflow optimisation software OptiSlang [48] could be used for DOE with ABAQUS inputs (*.inp*) to modify certain parameters. However, for the design optimisation, the tool ISIGHT offers more advantages due to a direct parametrisation of ABAQUS part geometries with an automatic mesh update in each run. It simplifies the simulation flow and does not require integration with other CAE components and subroutines.

5.1. Sampling

Once the working environment was defined, sampling techniques were employed to conceive the number of experiments. There are several ways to combine the model inputs in ISIGHT, including using by Stochastic sampling, Latin Square methods or Factorial Design techniques [43]. In Full Factorial experiments with 11 variables, it would be necessary to have a minimum of 2^{11} samples, or 2 048, FEM simulations. Since parallel calculations are restricted to 5, a reduced size is envisaged to save time.

In a discrete distribution of observations, the experiments must be supported by statistical concepts to draw conclusions about the results concerning the sampling size. The ratio of the number of simulations with leakage to the total number of samples yields a generalization of the seal's efficiency. It is assumed that this seal failure relationship can be correlated by a reduced number of samples within the minimum and maximum range of the inputs. One technique available in ISIGHT, which is denoted as the Optimal Latin Hypercube, gives users the freedom to choose the number of experiments by evenly distributing the samples within an input space. Generally, this technique is recommended to increase the resolution of the experiment by selecting a higher order of combinations compared to the factorial analysis. However, it also works to reduce the data by eliminating redundancies between sample points. This statistical method for DOE is widely used to create computer experiments and exploratory designs [109]. Figure 5.2 shows three different sampling techniques represented by points and frames inside the range of two variables X_1 and X_2.

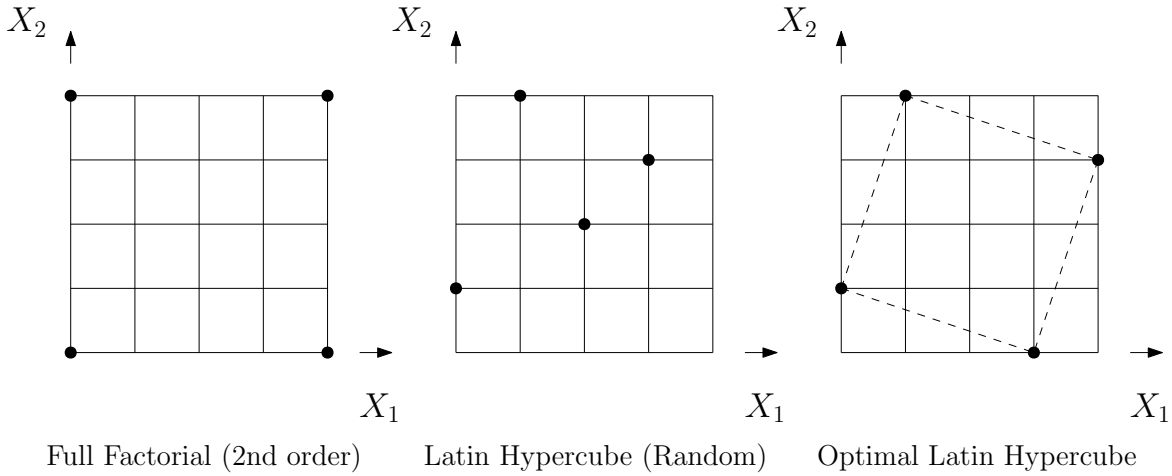

Figure 5.2. – Sampling concepts illustrated for a DOE configuration with two variables and four design points employing different techniques from ISIGHT.

In the left frames, the Full Factorial is presented with 4 points or experimental setups. Since this technique combines the maximum and minimum boundaries from each input, it allows 4 repeated input values either at X_1 or X_2 on an orthogonal array [110]. If more input variables are added and only a few have a significant influence on the outputs, these redundancies make no contributions to the experimental correlations. Alternatively, in the middle frame, a random distribution of points is employed with a Latin Hypercube arrangement to avoid dualities between points. Although the number of experiments is the same, the random data may create some bias due to the uneven sample distribution. Therefore, the optimal version [111] of the Latin Hypercube is better suited to avoid redundancies, since its algorithm attempts to maximize the distance between each point, as presented in the frame on the right.

Several criteria can be used to achieve an even distribution of samples. In the ISIGHT software, the optimal arrangement considers the *maximin* approach [112] that maximises the minimum inter-site distance between the sample vectors $\mathbf{x}_i$ and $\mathbf{x}_j$:

$$\min_{1\leq i,j\leq N, i\neq j} d(\mathbf{x}_i, \mathbf{x}_j) \tag{5.3}$$

where N is the number of samples and $d(\mathbf{x}_i, \mathbf{x}_j)$ is the Euclidean distance between the n-arguments indexed by k for the point pairs x_{ik} and x_{jk}:

$$d(\mathbf{x}_i, \mathbf{x}_j) = d_{ij} = \left[\sum_{k=1}^{n} |x_{ik} - x_{jk}|^2\right]^{1/2} \tag{5.4}$$

The Optimal Latin Hypercube technique sorts the inter-sited distances into a list $(d_1, d_2, ..., d_s)$ and then maximises the distances for all the s listed groups. According to the ϕ_p-optimal criteria [109], it is equivalent to minimise the following inverse relation:

$$\phi_p = d_{ij} = \left[\sum_{i=1}^{s} J_i d_i^{-p}\right]^{1/p} \tag{5.5}$$

where J_i is the pair of distances d_{ij} that are sorted by the algorithm, while p is assigned to a large positive integer number as described by Morris and Mitchell [109]. For a given set of $N = 500$ samples with $n = 11$ independent input variables, in Table 5.1, the Optimal Latin Hypercube technique manages to reach a ϕ_p plateau acceptance for the sample size. By starting with different random seeds, the *maximin* approach finds the optimal design matrix for FEM simulations after 11 000 iterations, requiring 19.2 minutes of CPU time. Table A.1 is included in the Appendix A to demonstrate the diversity of sample points considered for the computational experiments.

One of the advantages of the Optimal Latin Hypercube lies in the reduction of simulations, which became more than four times smaller compared to the Full Factorial approach. In fact, 500 runs were intended to be carried out during one day, since 5 runs in parallel required approximately 15 minutes per simulation. After 12h of idle computer, semi-finished DOE runs were available to be checked to determine if the results were coherent or not. This significantly helped to correct bugs and check if the parametric inputs that were given to ABAQUS were incorrect. Another important aspect is that the selected sampling technique works as a unique load case generator for the seal performance studies as each sample point corresponds to a hypothetical scenario for a single flight mission profile. Thus, an evaluation of how many failures occur regarding leakage or seal collapse gives a general representation of the seal's efficiency. With different design proposals, it should be assumed that the best candidate has lower failure occurrences. After the simulation runs are finished, a database is consolidated for statistical analysis. The outputs corresponding to each sample point are summarily evaluated in the post-processing interface with the help of data analysis tools.

5.2. DOE analysis

Seal efficiency is the first holistic analysis of the DOE results. From 500 simulations with different parameters for the conceptual design, the number of runs without leakage reveal how efficient a seal is on average of possible flight missions. Therefore, it is necessary to account for the occurrences of failure modes due to leakage and collapse. Overall, 22 simulations did not reach convergence according to the implicit scheme. Hence, it is evident that of the 500 experiments that were performed, only 478 were valid for further analyses. Table 5.2 shows all entries used to calculate the seal's efficiency. By counting the simulations with leakage criteria equal to 1, a total of 244 runs lost their sealing capability at some point. Among these cases, 216 presented seal collapse, and all of these instances that occurred during the manoeuvring loads in step 5. In the remaining 28 cases, leakage took place during cruise conditions without structural instabilities. The scenarios with seal collapse are considered to be more critical, as they tend to be irreversible and may cause higher stresses. In general, leakage is the primary seal failure mode, which comprises the collapse events. Thus, runs without any leakage are accounted for in the sampling quantification of sealing efficiency.

Table 5.2. – Efficiency calculated from sealed runs categorised by valid samples.

Planned	**Divergent**	**Valid**
500	22	478

Collapse	**Leakage**	**Sealed**
216	244	234

Efficiency
49.0%

As the leakage criterion takes the seal collapse into account, the global efficiency of the adopted seal concept is 49%. Evidently, the sample distribution created by the Optimal Latin Hypercube technique is not representative of the normal flight conditions due to a higher occurrence of limit loadings. However, a uniform sample-based efficiency motivates the search for improved design candidates with greater effectiveness, especially for critical conditions. Reducing the risks of leakage in specific cases and design improvement recommendations require a verdict about the causes of leakage. ISIGHT has built-in tools to analyse the DOE database, including Pareto charts, Response Surface and Data Correlation. The Pareto principle is useful to break problems down into smaller components, if one assumes that 80% of failure occurrences are caused by 20% of the source variables. However, certain model input contributions can be neglected by this principle. Response Surfaces are mathematical functions based on the higher polynomials used to fit the outputs by taking the inputs as independent variables. Also referred to as *metamodels* [69], the approximations are useful for understanding the system performance, but they are not suitable for representing discrete-event patterns such as the case of seal leakage and collapse. Therefore, Data Correlations are rather employed based on statistical fundamentals given an interval of acceptance for the sample size. Additionally, Spearman's rank coefficients allow for assessing the extent of the influence of DOE variables.

5.2.1. Data correlation

Data correlation is very useful to understand the relationship of dependence between control variables and the measurements derived from experiments. These tables are built from correlation coefficients that attempt to explain statistical relationships between inputs (X_i) and outputs (Y_i). The Pearson correlation [113] is usually employed to populate the tables by the ratio between covariance and standard deviation that is represented as:

$$r_{XY} = \frac{\sum_{i=1}^{N}(X_i - \bar{X})(Y_i - \bar{Y})}{\sqrt{\sum_{i=1}^{N}(X_i - \bar{X})^2}\sqrt{\sum_{i=1}^{N}(Y_i - \bar{Y})^2}} \tag{5.6}$$

where $\bar{X}$ and $\bar{Y}$ are the mean values of N samples from each variable. A more robust coefficient calculation called Spearman's rank is often recommended to slightly reduce non-linearities from experiments. By transforming the experimental data for both variables into ranked values and then substituting them into Equation 5.6, a rank coefficient is similarly calculated. In fact, ranking is a way of cataloguing higher and lower values from variables through positive ordinal numbers which allow the Spearman's rank coefficient to be written in the following form:

$$r_s = 1 - \frac{6\sum_{i=1}^{N}\Delta R_i^2}{N^3 - N} \tag{5.7}$$

where ΔR_i is the difference between two ranks $R(X_i)$ and $R(Y_i)$ variables. The operator R stands out in the ranking process, which can easily be addressed in Microsoft Excel with the *Rank.AVG* function by selecting column inputs from Table A.1 to transform each line value. Since the ISIGHT tools do this internally with the database, ranking is merely stated to differentiate Spearman's rank from the standard Pearson correlation. In this case, the coefficients not only quantify how strong the relationship between the variables is but also how they interact. If a correlation coefficient is close to 1, a proportional relationship exists between an input and output. On the other hand, an inverse relationship between the variables brings the coefficient to -1. When the rank coefficients are close to zero, it indicates a lack of dependence between the inputs and output.

For the DOE, some of the correlations should yield values close to zero, as they are not conjugated by the same time events. For instance, the air temperatures, T_2, have no causality effect on the maximum reaction forces (Force), as are measured before the aircraft starts to fly. On the other hand, different coefficients are expected to be driven by at least one strong factor, such as the ground temperature (T_3) and the final displacement (Residual), which is mainly influenced by the creeping of the seal. The force and displacements are very good output controls to check if the correlations are physically coherent, whereby the main outcome is the evidence of multiple effects coming from individual inputs. Air leakage and seal collapse can be influenced by a conjunction of factors that may be explained by the data correlation.

Table 5.3 shows the rank correlation coefficients calculated after 478 simulations with the conceptual seal design for the DOE. The *heatmap* chart is chosen since it is useful to visualise where the spots with direct proportional or inverse relations are. With Spearman's Equation 5.7, the variables employed are represented by the vectors $\boldsymbol{X}_i$ and $\boldsymbol{Y}_i$, indexed by the sample runs from the DOE database, where:

$$\boldsymbol{X}_i = [\, R_x \,, R_y \,, P_x \,, P_y \,, M_x \,, M_y \,, SH_A \,, \mu \,, T_1 \,, T_2 \,, T_3 \,]_i \tag{5.8}$$

are the input headers from Table 5.1 with 11 variables and:

$$\boldsymbol{Y}_i = [\, \text{Force} \,, \text{Leakage} \,, \text{Collapse} \,, \text{Safety} \,, \text{Residual} \,]_i \tag{5.9}$$

is summarised in Table 4.5 (seal performance indicators).

Table 5.3. – Spearman's rank correlation between the inputs and outputs.

Spearman's	**Rigging**		**Striker displacements**				**Material**		**Temperature**		
rank (r_s)	R_x	R_y	P_x	P_y	M_x	M_y	SH_A	μ	T_1	T_2	T_3
Force	0.06	0.83	0.01	-0.09	0.01	-0.05	0.37	-0.08	-0.01	0.02	-0.01
Leakage	-0.04	-0.47	0.04	-0.04	-0.23	-0.18	-0.36	0.04	-0.01	0.02	0.02
Collapse	-0.22	-0.20	0.07	0.08	-0.16	-0.22	-0.05	-0.22	0.09	-0.01	-0.03
Safety	0.23	0.18	-0.12	-0.01	0.19	0.21	-0.30	0.25	-0.05	0.02	0.06
Residual	-0.08	-0.10	-0.02	0.14	0.04	0.13	-0.01	0.04	0.10	0.02	-0.87

As previously estimated, a high correlation between residual displacement and ground temperature (T_3) has an inverse relationship, whereby the lower the ground temperature, the higher the residual displacement at the end of the final analysis step. On the other hand, the reaction force presents a direct dependency on the striker's position in the y direction. It is noteworthy that the coordinate system for the relative displacements is reversed compared to the global system, which means that rigging tolerances in the $+y$ direction cause more seal compression by the striker, thereby increasing the reaction forces during closure. Furthermore, the seal hardness variation has a similar influence, albeit of a lower intensity than the rigging since the correlation value is smaller. Before going into detail about each performance indicator in the correlation table, a limit must be set for the coefficient values that express dependence among the output outcomes with model inputs. According to Ramsey [114], a test is commonly performed to verify the significance of Spearman's rank based on the Z-test for normal distribution:

$$Z = r_s \sqrt{N - 2} \tag{5.10}$$

where N is the number of samples considered for the correlations.

Given the sample size of the Z-test, a threshold probability value $\alpha > 0.001$ is used to reject the null hypothesis that no correlations exist between a certain input and output. It corresponds to a confidence level of 99.9% where Spearman's coefficients $|r_s|$ are greater than 0.15 in their absolute values. Table 5.4 highlights the confidence levels for all Spearman's rank coefficients for which a correlation should exist.

Table 5.4. – Confidence levels based on Spearman's ranks with $N = 478$.

Confidence	**Rigging**		**Striker displacements**				**Material**		**Temperature**		
interval [%]	R_x	R_y	P_x	P_y	M_x	M_y	SH_A	μ	T_1	T_2	T_3
Force	83.1	99.9	19.0	95.8	17.3	74.3	99.9	93.0	11.8	25.6	19.0
Leakage	65.2	99.9	55.5	64.0	99.9	99.9	99.9	66.3	19.0	30.9	35.3
Collapse	99.9	99.9	86.2	90.3	99.9	99.9	73.4	99.9	95.1	22.3	48.7
Safety	99.9	99.9	99.1	10.4	99.9	99.9	99.9	99.9	72.5	33.7	77.8
Residual	93.6	96.4	33.3	99.8	58.0	99.6	12.1	66.3	97.3	37.0	99.9

From this approach, a preliminary screening of the DOE results reveals the model inputs that probably had the greatest influence on the seal performance indicators:

- **Rigging:** it has more correlations among all factors. Since it is an input that affects the initial conditions of the FEM problem, there are chances that it impacts the performance indicators of the seal at some point.
- **Displacements:** most correlations due to the relative motion of the striker arise from the effects of flight manoeuvres. Displacements resulting from pressure and cruise conditions (P_x and P_y) are unlikely to have an impact on any performance indicator compared to manoeuvre displacements (M_x and M_y).
- **Material:** the mechanical properties of the seal, although simplified for DOE studies, influence leakage and collapse. Notably, they play an important role in the reaction forces and the stress safety factor.
- **Temperature:** although the material model and boundary conditions have been enforced to capture thermal effects for creep and relaxation, there are not many correlations with the temperature levels apart from the residual displacement.

Only a few variables should be used to redesign the seal. Through the correlation tables, it was possible to visualise and filter the input variables with a high impact on the seal's efficiency. In the following Subsection 5.2.2, the data correlation results are interpreted to select the critical inputs for design improvement.

5.2.2. Interpretation of the results

First, each output row of Table 5.3 is individually discussed with respect to the input variables that were highlighted in Table 5.4:

- **Force:** as previously mentioned, reaction forces are mostly driven by two factors, namely rigging tolerances and material stiffness. The initial displacements from R_y have more influence on the maximum values than the shore hardness SH_A of the elastomer.

- **Leakage:** it seems to be driven by factors from rigging, material, and manoeuvre displacements. The lower the seal compression, the lower the contact pressures that impair the sealing effect. When SH_A is reduced, it mostly affects the material stiffness. Conversely, a negative R_y in the seals does not enable a sufficient compression of the section. Additionally two other displacement variables M_x and M_y can play a role in flight manoeuvre events. If the striker moves towards the cabin, with a negative displacement, there are more chances for leakage to occur. However, other in-flight displacements due to pressurisation do not seem to have a detrimental effect on the seal performance. Although the model takes temperature into account for the viscoelastic modelling, no seal relaxation influences were evidenced for the leakage occurrences.

- **Collapse:** Even though leakage embeds the cases with collapse, it is possible to provide evidence that the variables that drive both criteria are slightly different. It is very unlikely to correlate this performance indicator correctly since the collapse values are binary, i.e. either 0 or 1 which is why the correlations are fairly weak for the valid inputs. Notably, the friction coefficient μ plays an important role in the seal collapse as the greater its value, the lower the chance of a sliding mechanism that could trigger contact losses. Negative manoeuvre displacements are likely to be critical because they work in the opposite direction of the pressure load, which also explains the correlations of the leakage with M_y. Here, the ringing tolerance R_x seems to be equally correlated to the seal collapse. Thus, a combination of rigging and manoeuvrers could trigger structural instability.

- **Safety:** these correlations are almost inverse to the seal collapse, with the exception of the material hardness SH_A. This is because once the modulus of elasticity of the material is higher, the stresses also increase. As the absolute allowable value of 8MPa is fixed, the safety factor essentially relates to the rise in internal stresses in the material. In general, the occurrences linked to collapse correspond to those with low safety factors.

- **Residual:** residual displacements are mostly related to the final temperature on the ground T_3 of the destination. Although not used in the design improvement, it serves to check whether the simulations were sensitive to the temperature.

5.3. Outcomes

From the analysis of the DOE data, some questions can be answered regarding the efficiency of an aircraft door seal against leakage. Systematically, different designs can be evaluated under identical conditions and compared according to their performance indicators. Using data correlation and statistical analysis, the experimental variables that are most relevant can be filtered. The causes of seal failure and leakage may be highlighted by means of Spearman's correlation coefficients in table form. With a high confidence interval given the number of samples considered, it is possible to identify which FEM model inputs are critical to the seal analysis outputs.

These outcomes are important to separate the dimensioning load cases for the seal. In theory, it is possible to add an optimisation loop after a DOE process in ISIGHT. However, each round of optimisation would require another 500 simulations to be performed for each design iteration. A very large number of simulations would be required until the 'best' candidate is accepted by an optimisation criterion. For this purpose, the insights gathered from the DOE data analysis are useful to define a reduced number of scenarios for design improvements. In general, thermal loadings should not be applied as no significant correlations have been demonstrated for leakage, collapse or reaction forces. A low coefficient of friction should be considered for optimisation studies since it contributes to an increased chance of collapse. Since the unsealed runs happened after manoeuvre events, the striker displacement U_y must be prescribed in the worst configuration from the combination between P_y and M_y after the door closure displacement C_y. Figure 5.3 displays how the displacements are fixed for the critical conditions. U_x and R_y are defined according to the nominal, negative and positive positions of the striker, according to the maximum and minimum seal compression for the optimisation tasks in Chapter 6.

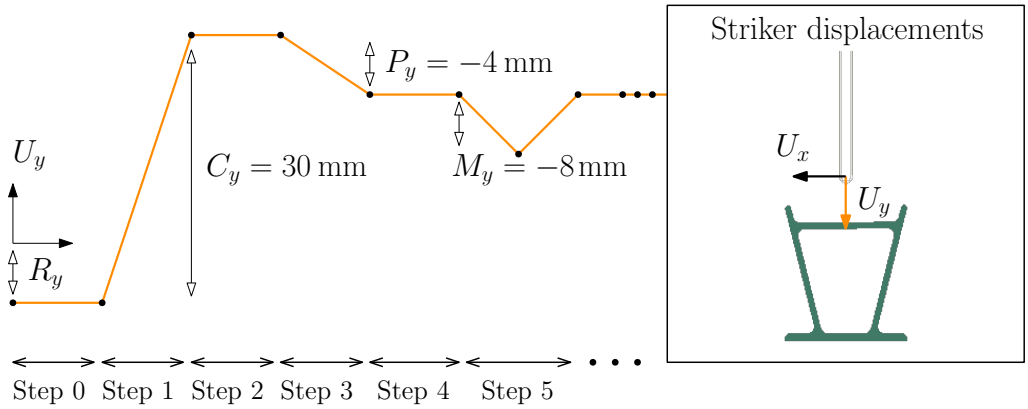

Figure 5.3. – Striker displacement envelope in U_y used for optimisation runs.

The following subsections describe the three load cases used in Chapter 6 with variations of the striker displacement for the ground and flight steps in the U_x direction.

5.3.1. Load case 1: R_x nominal max compression

The objective behind a nominal loading case is to evaluate the maximum reaction force undergone by the seal. It considers the striker in the nominal position for R_x, but with maximum tolerances in the positive y-direction. This extreme case of rigging with $R_y = 4$mm is used to tighten the limited operating conditions for door closure. The hardness of the seal is assumed to have a maximum value of $SH_A = 61$ so the material stiffness is the highest. After step 2, the striker moves uniquely in the y-direction due to the cabin pressure and manoeuvring effects following the envelope from Figure 5.3, while the striker displacements U_x are kept fixed to the nominal position. It serves to check if the seal is able to perform its function under normal disturbed conditions. Alternatively, load cases 2 and 3 consider the striker's lateral movement.

5.3.2. Load case 2: U_x positive min compression

Contrary to the previous scenario, in load case 2, the striker U_x relative displacement is assigned to the positive direction from the nominal reference. In order to prescribe severe conditions, the rigging tolerance of $R_y = 4$mm is assigned to reduce the reaction forces during closure thereby presenting a minimum compression of the seal profile. Under this condition, the seal was not able to establish higher contact pressures during manoeuvring, which increased the leakage and collapse occurrences in the DOE. Lastly, the material stiffness is reduced to $SH_A = 51$, while maximum displacements $P_x = 4$mm and $M_x = 8$mm are set to impair the structural strength.

5.3.3. Load case 3: M_x negative min compression

Load case 3 is a variation of load case 2 with the exception of the manoeuvre displacements M_x and R_x. As the cabin pressure brings the striker to the atmosphere direction due to the door cut-out deformation, P_y is kept at 4mm. However, the displacement manoeuvres can occur in the opposite direction to the pressure loading, which is likely to cause collapse due to the sliding movement. Therefore, the maximum negative displacement of $M_x = -5$mm prescribes a reverse motion. Although there is no strong correlation between positive manoeuvre displacements and leakage, it is speculated that some leakage originates from reverse displacements. Analogously, the same rigging tolerances are assigned to R_y as in load case 2. Since it operates with lower compression levels, the striker is placed with a negative tolerance of $R_x = -4$mm, which is added to the manoeuvre displacements.

A final remark about DOE: it is assumed that the load case descriptions presented in Subsections 5.3.1, 5.3.2, and 5.3.3 are the most critical for the seal design to reduce the number of simulations. However, the sealing concept should be redesigned with more conservative loading conditions to further improve the efficiency of the DOE.

6. Parametric Optimisation

Within the branch of structural optimisation of the FEM, parametric and non-parametric techniques can be distinguished. In the case of a non-parametric optimisation, the initial mesh region is given to an optimisation process that either removes the mass without changing the elements (topology optimisation) or manipulates the position of the nodes (shape optimisation) to achieve the desired goal. On the other hand, Parametric Optimisation uses design variables, e.g. from CAD, in an optimisation process bounded by dimensioning values. Because non-linearities mostly arise from the FEM simulations of contacts, it is cumbersome to employ Non-Parametric Optimisation tools such as TOSCA [115]. Thus, Parametric Optimisation is favourably considered to improve the seal design shown in Figure 4.1 while Table 6.1 presents the design parameters bounded by the maxima and minima based on the conceptual measures from Table 4.1.

Table 6.1. – Design parameters' range of the door seal optimisation.

Design parameters	Description	Minimum	Maximum
t_L, t_R, t_T	Thickness (seal wall)	1.0mm	5.0mm
H_L, H_R	Height (seal wall)	35.0mm	43.0mm
h_L, h_R	Height (lip feature)	1.0mm	5.0mm
θ_L, θ_R	Angle (seal wall)	60°	90°
w_B	Width (seal bottom)	5.0mm	15.0mm

The way the desired goal is reached derives from the reference to multi-parametric design optimisation [77], except that force and leakage are considered as multi-objective functions to be minimised subject to the following constraints:

$$\min_{x_i \in \text{Table 6.1}} f(x_i),\, g(x_i) \qquad f(x_i) = \text{Force} \tag{6.1a}$$

$$g(x_i) = \text{Leakage} \tag{6.1b}$$

$$\text{subject to} \qquad \text{Leakage} < 1 \tag{6.1c}$$

$$\text{Collapse} = 0 \tag{6.1d}$$

This approach attempts to optimise the seal geometry with the lowest reaction force while respecting the leakage and seal collapse criteria for the three critical load cases presented in Subsections 5.3.1 to 5.3.1.

Ultimately, it is anticipated that the geometry can be improved simply by a better combination of the design variables associated with the cross-section. By reducing the reaction force, it is envisaged to reduce weight in the closure mechanism, while keeping structural strength to cover critical cases. Some performance indicators are not employed for the optimisation according to Table 4.5 in Section 4.4. The safety is covered by the collapse events, while the residual displacements are hard to integrate into the optimisation scheme since they need to be considered from the loading history. Therefore, an optimisation task is built into the software by integrating three models in parallel according to the critical loading conditions. Figure 6.1 presents the scheme given to the optimisation algorithms to search for better design candidates.

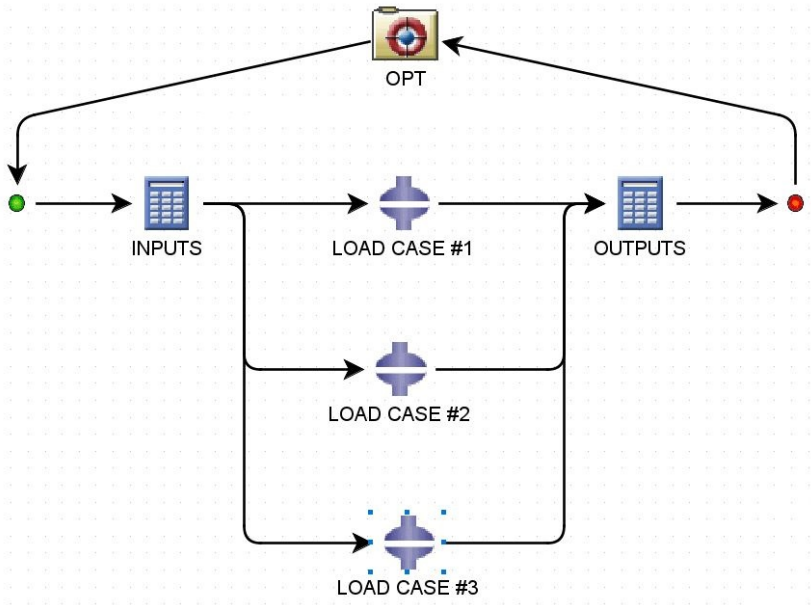

Figure 6.1. – Components of the ISIGHT interface for the Optimisation.

In the ISIGHT tool, some optimisation techniques are implemented depending on objective functions, either by considering design constraints or not, to minimise the multi-objective functions. Among the available options, the Non-dominated Sorting Genetic Algorithm (NSGA-II) and the Large Scale Generalised Reduced Gradient (LSGRG) can be employed, respectively, to explore and refine the designs candidates. According to the ISIGHT manual, the NSGA-II is well-suited for highly non-linear problems with discontinuities, while the LSGRG is useful for exploring the local area around an initial design point, which should be provided in anticipation. In standard operations of mutation and crossover, the NSGA-II attempts to keep the 'best' candidates by constructing a *Pareto* set, in which it is not possible to improve one objective without sacrificing another. Lastly, the LSGRG deals with inequality and equality constraints under convergence conditions to look for design improvements.

6.1. Non-dominated Sorting Genetic Algorithm

NSGA-II is classified as a multi-objective exploratory technique that is comprised of a group of GA [45]. The heuristics behind it does not have a mathematical proof that guarantees solutions that are either minimised or maximised for multiple objectives. However, these algorithms are largely employed to solve computationally complex problems, since they present a faster and more efficient solution compromise than gradient-based methods. Being categorised as part of evolutionary algorithms, NSGA-II follows a modified mating and survival selection for the combination of design variables based on the general outline of a genetic analogy. It is derived from the assumption that not all individuals in a population may pass their genes to the next generation since each individual is ranked by their objectives. The algorithm takes the standard operations of mutation and crossover from GA into account and deals with each objective function independently through a *Pareto-optimal* [51].

Initially, the diversity of a population is provided by a random seed that is considered within the range of dimensions provided in Table 6.1. Each individual is seen as a unique seal, with specific size parameters (x_i) or a genetic code, that is composed of 10 independent design variables. In the optimisation procedure, each objective function $f(x_i)$ and $g(x_i)$ is treated separately to construct a *Pareto* front with feasible non-dominated solutions [116]. It implies that none of the objective functions can be improved without impairing the other function, which means that a candidate design has a certain trade-off between force and leakage, e.g $f(x_i) < g(x_i)$. Consequently, the 'best' solution is selected by comparing the candidates after certain genetic interactions are completed, given the population size and how many generations of the genetic process are considered. Each objective function has a different unit and magnitude, which makes the design choice a compromise between both objectives to be optimised [77]. Since leakage is described as a qualitative index, the 'best' design is pragmatically taken from the lowest reaction force delivered by load case 1.

To verify if the algorithm is capable of converging into comparable design solutions, different initial populations are generated to provide at least three best candidates among all the generations. Since this technique is not well-suited for long-running simulations due to the strong dependence on crossover and mutation parameters of the genetic algorithm, a reduced number of simulations is envisaged in the attempt to achieve time-feasible results. Compared to the DOE, NSGA-II can explore candidates more quickly than sampling techniques by employing the recommended control settings for the genetic algorithm. A probability parameter establishes how often the recombination of genes between parent and offspring solutions occurs and two distribution indices are related to crossover and mutation operations that inversely influence how the genes are disturbed. The lower the value of these control parameters, the greater the variation of each generation. The ISIGHT manual recommends values of high probability and lower distribution indices to add diversification and achieve a quick convergence at the cost of a highly focused search.

6.1.1. Optimisation rounds

Table 6.2 provides the standard parameters recommended by ISIGHT that are attributed to the NSGA-II algorithm for optimisation rounds. In total, 240 interactions are performed for each round of optimisation according to a population size of 12 individuals for 20 generations. It is important to highlight that the three critical load cases from Subsections 5.3.1, 5.3.2 and 5.3.3 are simulated in parallel inside the optimisation loop in Figure 6.1. When a round is started, 720 simulations are queued with a maximum of 5 simultaneous calculations due to processor limitations. If a similar DOE approach was considered for a total of 500 samples, it would take at least 3 days to complete each optimisation round. Thus, the importance and necessity of optimisation techniques to overcome the time constraints in the search for design solutions become clear.

Table 6.2. – NSGA-II standard parameters employed for optimisation in ISIGHT.

NSGA-II parameters	Value
Population size (multiple of 4)	12
Number of generations	20
Crossover probability	0.9
Crossover distribution index	10
Mutation distribution index	20
Initialisation mode	Random

A random initialisation mode causes the algorithm to generate the first population evenly with Latin-Hypercube sampling. Along with unbiased Knuth Shuffling [117], a population size with a multiple of 4 individuals should be provided which establishes a nearly uniform distribution of individuals within the design space. Since the first generation can influence how the problem converges to a better or worse solution, random seeds are used to highlight the trend towards a single 'best' candidate. However, there is no guarantee that the final design is accurate enough to be close to a relative local minimum. In addition, the problem is likely to have many local minima within the conditions imposed. Depending on the technique employed, or on the formulation of the objective function, different types of design solutions can be achieved due to the high nonlinearity of the problem. Sensitivity studies with the genetic algorithm parameters would be required to effectively perform longer searches with small control parameters and a larger number of simulations. Therefore, three optimisation rounds with different random seeds are employed to check if closer design candidates are reached at the end of each round. Ideally, for the seal optimisation problem, another set of control parameters for the NSGA-II technique may improve convergence. However, the scope of this study is to evaluate the capabilities of available optimisation techniques, rather than to focus on the algorithm calibration.

Figure 6.2 displays the objective function $f(x_i)$ only represented by the individuals with different starting population sets. Inside the graph area, small circles represent the feasible simulations, while red triangles are unfeasible runs due to constraint violations from Equations 6.1c or 6.1d. The blue diamond marks are Pareto-optimal designs, whereby a single candidate is highlighted as the 'best' feasible design with the smallest force result.

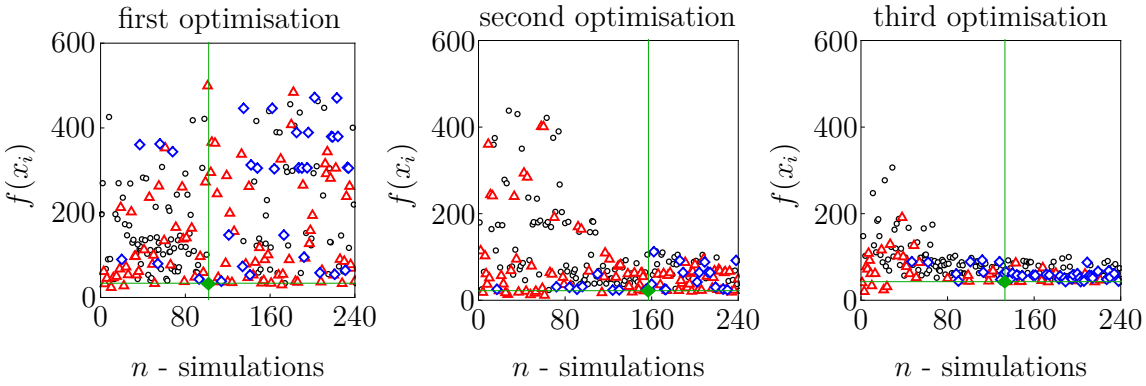

Figure 6.2. – Optimisation results for three random seeds with NSGA-II.

On the first examination, the findings appear to indicate that the third round of optimisation has a convergent trend, which implies a batch of individuals with a better combination of design parameters. However, it is necessary to compare the objective function results concerning the optimised design variables. Table 6.3 summarises the combination of dimensions of each design variant corresponding to the optimisation rounds A, B, and C with the run number (n) from which the candidate is obtained.

Table 6.3. – Design parameters extracted from each NSGA-II optimisation round.

OPT	Wall thickness			Seal height		Lip height		Width	Angles		Force	Leakage
NSGA-II	t_T	t_L	t_R	H_L	H_R	h_L	h_R	w_B	θ_L	θ_R	$f(x_i)$	$g(x_i)$
Variant (n)	[mm]								[grad]		[daN/m]	[-]
A (102)	2.7	1.5	3.4	39.3	42.7	2.9	2.3	8.6	64.0	74.6	**33.7**	**0.518**
B (157)	2.8	1.0	4.5	37.5	37.5	1.7	3.1	11.6	70.4	72.7	**22.1**	**0.586**
C (133)	1.2	3.3	4.0	36.0	38.3	1.5	2.4	14.5	70.2	72.2	**42.9**	**0.471**

For the first variant A, the best candidate was extracted from the 9th generation, while variants B and C appeared during the 14th and 12th generations, respectively. Examining the values from right to left in Table 6.3, it is apparent force and leakage are competing in the multi-objective criteria. Notably, load case 3 described in Subsection 5.3.3 has critical values for $g(x_i)$ in contrast to $f(x_i)$ sized by case 1, in Subsection 5.3.1. The collapse of the seal is mostly driven by case 2 in Subsection 5.3.2.

In the second round of the optimisation, the algorithm was able to generate candidates with lower reaction forces compared to the first optimisation. Since the initial population of the third round started with slightly lower reaction forces for feasible solutions, the algorithm favoured design features that minimised leakage rather than force. On the other hand, variant A emerged from an intermediate solution with values of force and leakage that are more dispersed according to the distribution of the *Pareto* points. Figure 6.3 displays the feasible runs with a *Pareto* front formed with blue diamond marks, with the best candidate highlighted using green lines.

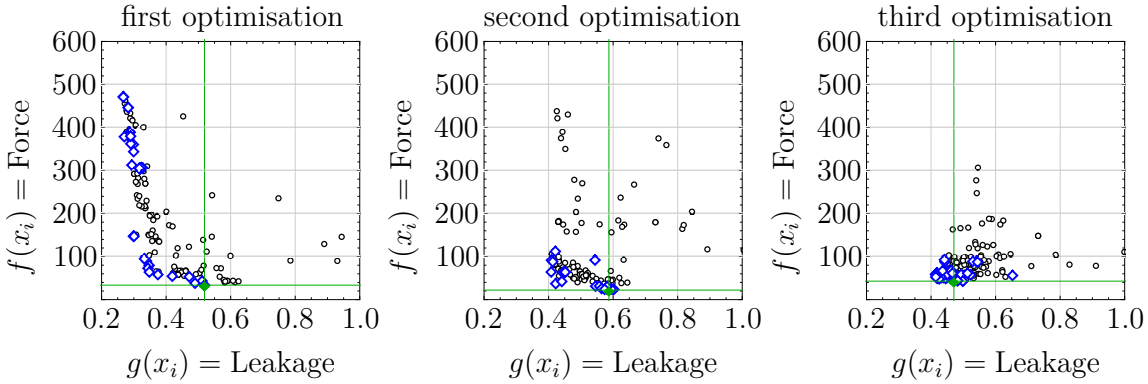

Figure 6.3. – *Pareto*-optimal front from NSGA-II between objectives.

Throughout the course of the optimisation from random design populations, it can be observed that the algorithm finds distinct solutions depending on how the first generation evolves. According to the references on NSGA-II [45], the main difference from the standard GA resides in the way the population diversity is maintained. A *Pareto*-optimal set is considered to transmit the genes, whereby NSGA-II presents higher elitism compared to standard GA since it ranks candidates before crosslink and mutation. When compared to other evolutionary algorithms with more spread populations [118], NSGA-II often leads to faster convergence of results at the cost of reducing the variety of solutions to be explored. However, for the design variables in Table 6.3, each seal candidate is slightly different, showing close deviations from the conceptual geometry in Table 4.1. The wall thickness was optimised to be thicker on the right-hand side of the seal (t_R) compared to the left (t_L) and top (t_T) locations. The seal height on both sides (H_L and H_R) was moderately reduced from the original height of 40mm in most cases. Furthermore, the lip heights (h_L and h_R) were reduced, except for of the optimisation variant B, which kept a similar size on the right side (h_R). The angles (θ_L and θ_R) were adjusted just below the conceptual value of 75° for all of the candidates and only the base width (w_B) turned out to be distinct for each optimisation. Nevertheless, the selected solutions are potential seal candidates that provided a minimum amount of reaction force for aircraft door ground operations without violating the in-flight leakage and collapse for the three critical conditions.

6.1.2. Design candidates

Figure 6.4 contrasts the cross-section of each design candidate with filled colours against the original seal profile represented by lines. These solutions reflect how the selection process keeps certain design features that are beneficial for the seal's efficiency, while certain regions are added due to the genetic operations.

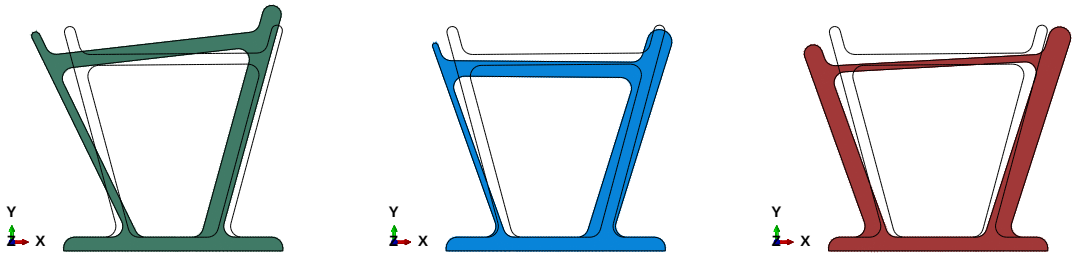

(a) Variant A ($n = 102$) **(b)** Variant B ($n = 157$) **(c)** Variant C ($n = 133$)

Figure 6.4. – Seal design candidates compared to the original concept profile.

Visually, it is possible to highlight that the aspect ratio of the profile was partially preserved from the conceptual design. The values of the heights and angles reveal that the first geometry used for the DOE was not beyond the scales that contribute to the seal's efficiency. However, at least two thicknesses around the section were increased, while one wall was hindered by the algorithm, mostly to reduce the force during seal compression. Figures 6.4a and 6.4b show thinner thicknesses on the right-hand side, while Figure 6.4c presents another option with lower thicknesses at the top wall. Since variants A and B have geometrical similarities, it is preferred to preserve the second design because it exhibits less reaction force during the door closing. Alternatively, there is potential behind the geometry of variant C due to the reduced leakage index, which was initially not considered in the screening criteria for the candidates. Thus, the two remaining designs are further investigated with regard to the multi-objective improvements on leakage and force by employing different optimisation methods. It is assumed that the candidates found were close to a local minimum in the vicinity of each solution. As previously described, GA are techniques that do not necessarily deliver the optimal solution in a few steps. In theory, if the number of generations and individuals per population were increased, different candidates could emerge from the optimisation process. However, it would require a large number of simulations to be carried out by the algorithm, since most of the designs explored were not even feasible solutions. Thereby, in the next section, the input variables from the remaining candidates are employed as the starting point for the design refinement by exploring a gradient-based technique. In this manner, it is aimed to obtain improved solutions, with fewer simulations based on convergence criteria to judge a single 'best' design.

6.2. Large-Scale Generalised Reduced Gradient

In this last task of the Multi-Parametric Optimisation, the LSGRG method is employed in the search for improvements, starting from the B and C variants discovered by NSGA-II. The concept behind the generalised reduced gradient is to use implicit methods to solve a multi-objective function while using constraints and equalities to reduce the number of independent variables. Thus, the algorithm performs a search in certain directions of the design space based on a vector of dependent variables that satisfies all the constraints [47]. This method was not used in the first instance for the concept geometry because it requires a starting point for feasibility. In the first phase, if the initial design is not feasible, the algorithm performs several interactions to reach at least one valid solution, otherwise the optimisation stops. Once a starting point is reached, the algorithm begins a second phase to search for small improvements. Basically, in the ISIGHT solver, the same components and problem formulations are given to the LSGRG algorithm, but it is possible to shift between optimisation techniques while employing other settings. Table 6.4 provides the control parameters that are specified by the LSGRG algorithm for each design refinement with custom inputs.

Table 6.4. – LSGRG custom parameters employed for the optimisation algorithm.

LSGRG parameters	**Value**
Max iterations	100
Relative step size	**0.1**
Convergence criteria	**0.1**
Convergence interactions	3
Max failed runs	5
Initialisation mode	Custom

The values in bold are not standardly recommended by the software, but they are provided to increase the convergence speed. A larger step size of 0.1 is used to modify the design variables at the first decimal place to reach faster convergence. Since dimensional tolerances of ± 0.1mm and ±0.1° for the angles are expected from the manufacturing process, it is not interesting to keep the precision under this scale. Equally, the convergence criterion is accepted once the multi-objective function does not vary in the first decimal place for the sum of $f(x_i)$ with $g(x_i)$ after 3 iterations. This means that either leakage or force can not be minimised by more than 0.1 together, thereby restricting the improvement of the design goal of each candidate. A convergence interaction is required to stop the algorithm, as well as a maximum number of sequential failure runs for the divergence criterion. LSGRG is suited for nonlinear design spaces without too many discontinuities whereby it is assumed that the objective functions are continuous in the vicinity of each design candidate.

6.2.1. Design refinement

Figure 6.5 shows how the seal design variants are refined for the multi-objective function using the LSGRG optimisation technique. Once more, small circles are feasible solutions and blue diamonds are *Pareto* points. The design refinements were frozen after the convergence criterion was reached, as indicated by the green lines.

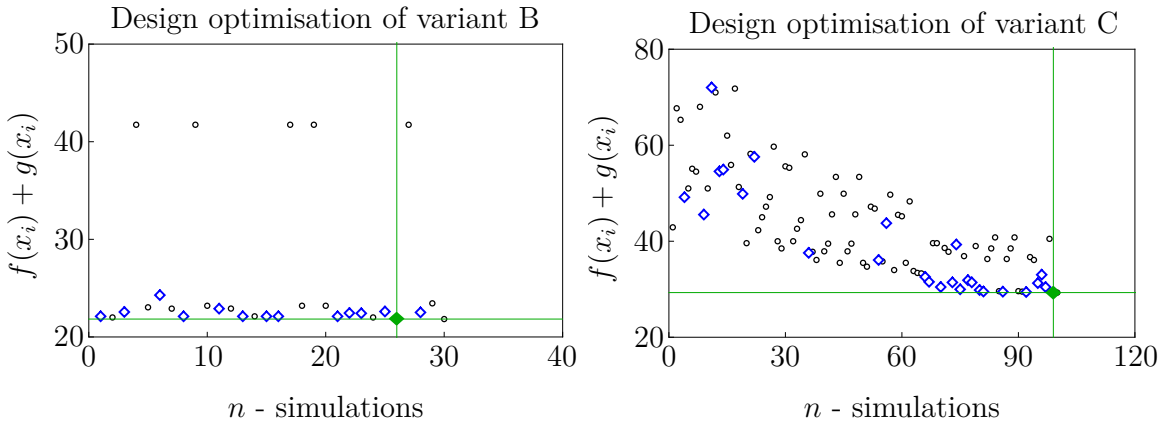

Figure 6.5. – Design refinement with selected variants using LSGRG.

From the results, it is apparent that variant C was improved to reduce the force in conjunction with leakage. On the other hand, variant B was not improved as much, which implies that the solution found by NSGA-II is already optimised regarding the sum of objectives $f(x_i) + g(x_i)$. This means that the refined variant B* is close to the original design source B, while the new variant C* provides major changes in the force results compared to C. Table 6.5 summarises the dimensions extracted from the 'best' candidates that minimise the combination between force and leakage.

Table 6.5. – Design parameters refined with the LSGRG optimisation algorithm.

OPT	Wall thickness			Seal height		Lip height		Width	Angles		Force	Leakage
NSGA-II	t_T	t_L	t_R	H_L	H_R	h_L	h_R	w_B	θ_L	θ_R	$f(x_i)$	$g(x_i)$
Variant (n)	[mm]								[grad]		[daN/m]	[-]
B* (26)	2.8	1.0	4.4	37.2	38.5	1.7	3.1	11.6	70.3	72.7	**22.1**	**0.580**
C* (99)	1.0	3.1	3.8	36.8	38.2	1.9	1.9	15.0	67.6	69.9	**27.3**	**0.459**

Remarkably, small changes in the thickness helped to reduce the force by 36% and leakage by 2.5%, when compared to the original C variant. Despite the optimisation efforts, the force remains the same for variant B*, with small improvements in the leakage. Since the optimisation process is mostly driven by the force results, the leakage has less of an impact on the sum of both objectives.

6.2.2. Design comparisons

Each new variant is compared in terms of the FEM simulations for the critical conditions used for the optimisation tasks. Through judgement during certain time frames of the analysis regarding force, leakage and collapse, a single geometry is selected to be carried out for seal efficiency comparisons with the original design. Figure 6.6 displays the moment when the maximum force is reached for variant B* for load case 1 from Subsection 5.3.1. At this point, the striker moves 24.6mm from its original position, which generates low reaction forces for variant C*. It is possible to observe that the left wall of variant B* is structurally weaker than C*'s left wall, leading to a buckling state, that was not observed in previous simulation results.

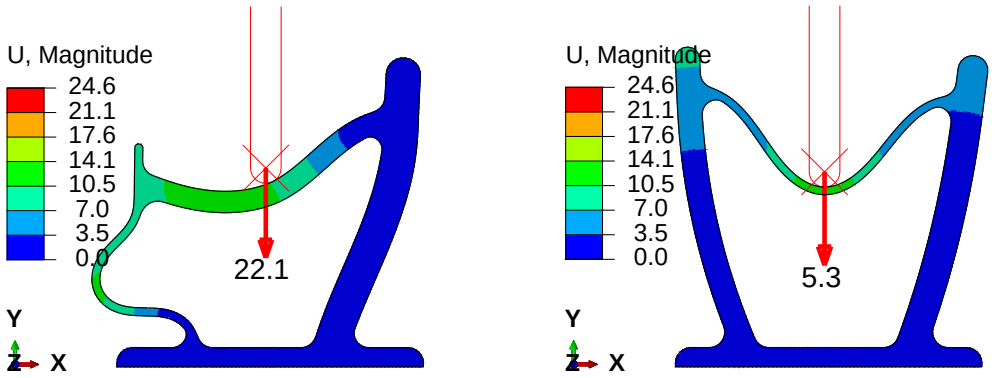

Figure 6.6. – Variants B* (left) and C* (right) at the initial compression stage.

Figure 6.7 shows the moment when the maximum force occurrs in variant C* at the end of the compression loading step, with 34mm for the displacement U_y. At this point, variant B* is no longer able to hold the seal in a stable configuration due to a buckled state (unstable). This premature failure mode was not considered in the door-closing stage, which requires adjustments to the optimisation in future studies.

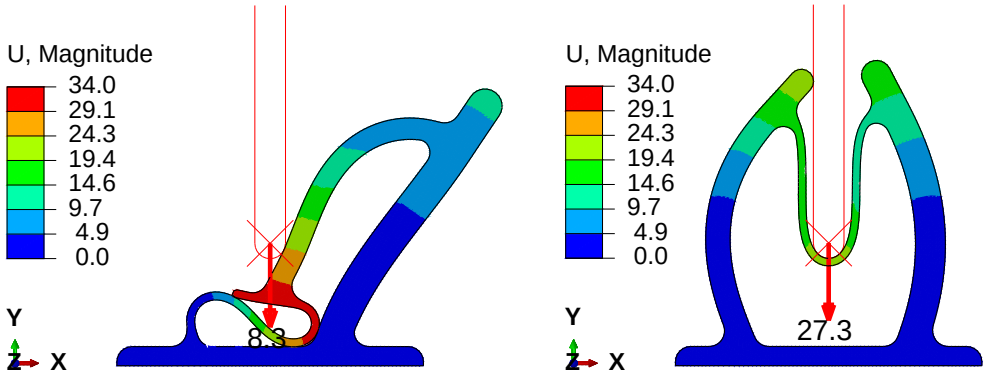

Figure 6.7. – Variants B* (left) and C* (right) at the maximum seal compression.

Figure 6.8 depicts the two variants respecting the collapse conditions for the critical load case 2, just after the maximum manoeuvrer displacement. Although the collapsing condition is respected, since the seals are in contact with the striker, variant B* has self-contact with its external walls on the bottom left side. Once the seal is inflated, the buckled wall pops out due to the differential pressure. This can lead to undesirable consequences, i. e. noise due to cavity volume change, as well as potential damage of the seal. Despite the magnitude of the absolute principal stresses (S) being within the limits admissible for seal failure, the high-stress amplitudes must be controlled to avoid fatigue problems.

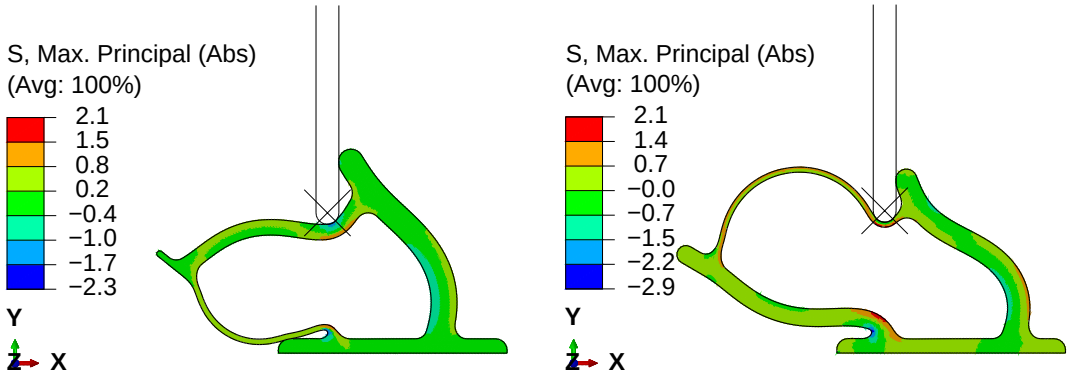

Figure 6.8. – Variants B* (left) and C* (right) respecting the collapse.

Figure 6.9 illustrates how both variants were able to keep the cabin airtightness with reduced leakage index at load case 3. In this case, the manoeuvre is carried out to the cabin side in the positive global x-axis or in the negative direction referring to the U_x coordinate system. The PPRESS contour plot in Figure 6.9 indicates where the maximum differential pressure is bounded by the contact striker interface due to the lip feature located on the right-hand side of the profile.

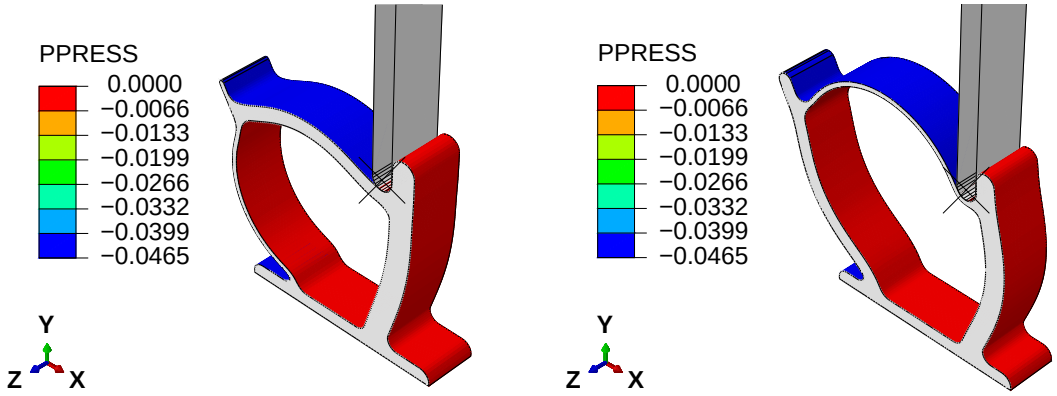

Figure 6.9. – Variants B* (left) and C* (right) with a reduced leakage index.

6.3. 'Best' seal design

According to the optimisation results in the previous section, it is possible to elect a single candidate as the 'best' design to improve seal efficiency regarding the 500 runs of the DOE. Based on engineering judgement, the last C* variant should be able to improve the seal's efficiency regarding leakage while ensuring structural integrity in critical loading cases and providing a minimum force for door operations. Thus, only the seal geometry is changed according to the tasks described in Chapter 5. Essentially, the 'best' design is compared to the first seal concept regarding the occurrences of leakage and collapse in the simulations. Despite the lack of validation of the analysis methods presented up to this point, either through component or system qualification tests, improvements in the sealing performance for applications in aircraft doors are expected. Furthermore, it is anticipated that the other sources that may impair the seals' functioning could be highlighted by the correlation table.

After completing the DOE rerun for variant C* employing the input protocol in Table A.1, the results are presented side by side with those of the conceptual design according to the survey of relevant performance indicators. Even if the initial main interest was to reduce the chances of leakage and collapse, it is possible to contrast other performance indicators obtained by virtual experiments to highlight design trade-offs that were not foreseen by the optimisation tasks. Minimum and maximum limits for force, displacement, and safety factor values are identified for every seal geometry, as well as average operational values, which may depend on the door system specifications. Table 6.6 displays the summary of the DOE comparisons:

Table 6.6. – Comparisons between 'best' and concept designs with DOE runs.

Performance indicators		**'Best' design**	**Concept design**
Force [daN/m]	Maximum	44.8	33.5
	Minimum	16.9	11.9
	Average	28.1	20.4
Safety	Maximum	83.4%	88.1%
	Minimum	47.2%	44.3%
Displacement [mm]	Maximum	9.4	16.9
	Minimum	0.2	0.6
	Average	2.3	2.7
DOE runs		**Occurrences**	
Valid runs		495	478
Leakage/Collapse		34/32	244/216
Sealed runs		461	234
Sealing efficiency		**93.1%**	**49.0%**

Correlation table

The improvements yield by the optimisation process are evident when examinating the sealing efficiency comparisons. In addition, more valid rounds occurred due to better convergence of results. Before discussing the results, Spearman's correlation coefficients are recalculated for the second DOE trial by only considering the valid simulations. Table 6.7 displays a different distribution of correlation coefficients r_s:

Table 6.7. – Spearman's correlation of the DOE trial with the 'best' design.

Spearman's	**Rigging**		**Striker displacements**				**Material**		**Temperature**		
rank (r_s)	R_x	R_y	P_x	P_y	M_x	M_y	SH_A	μ	T_1	T_2	T_3
Force	-0.19	0.09	-0.08	-0.08	-0.04	0.01	0.13	-0.02	0.09	-0.01	0.05
Leakage	-0.20	-0.15	-0.02	-0.10	-0.29	-0.03	0.44	-0.03	-0.01	0.18	0.01
Collapse	0.02	-0.57	-0.06	0.02	-0.29	-0.04	0.32	-0.24	-0.22	0.01	0.05
Safety	0.18	0.08	0.04	-0.04	0.15	0.02	-0.05	0.43	0.01	0.00	-0.06
Residual	-0.02	-0.09	-0.02	0.01	0.02	0.01	-0.01	0.00	-0.01	-0.03	-0.49

For a population of $N = 495$ and a confidence level of 99.9%, the $|r_s|$ values must be greater than 0.147 to reject that there is no correlation. Table 6.8 highlights the inputs that are strongly correlated to the performance indicators.

Table 6.8. – Confidence levels based on Spearman's ranks with $N = 495$.

Confidence	**Rigging**		**Striker displacements**				**Material**		**Temperature**		
interval [%]	R_x	R_y	P_x	P_y	M_x	M_y	SH_A	μ	T_1	T_2	T_3
Force	99.9	96.1	91.0	90.8	62.3	13.7	99.5	32.8	95.6	18.0	77.1
Leakage	99.9	99.9	36.2	97.4	99.9	47.2	99.9	50.3	19.4	99.9	21.2
Collapse	33.2	99.9	78.6	28.7	99.9	63.2	99.9	99.9	99.9	10.2	71.6
Safety	99.9	93.6	65.2	57.6	99.9	31.7	68.4	99.9	17.0	6.3	82.3
Residual	35.4	95.8	32.9	20.3	26.9	19.8	21.6	2.5	22.0	45.3	99.9

From these brief results, it is possible to draw new conclusions regarding the efficiency of the seal. From the conceptual design, points that were not previously apparent from the first correlation are discussed with regard to the optimised design.

6.3.1. Design discussion

As previously mentioned, the improvements to seal by the C* variant are remarkable. Because of the Parametric Optimisation based on the multi-objective problem, a considerable increase in the closing reaction force to ensure an improvement in seal efficiency is observed. On average, a 37% increase in force is expected, which is related to the thicker side walls. However, a maximum force of 44.8 daN per meter of sealing line must be considered depending on the door specifications. Despite the lower occurrence, the leakage cases that incorporated the seal collapse are still prone to deliver negative safety factors. Due to the high stresses resulting from the critical failure mode, seal rupture is a major issue that was not completely covered by the optimisation tasks. A distinct improvement stems from the reduction of the maximum residual displacement. Arguably, raising the overall stiffness of the design allows a seal to be more resilient in recovering its original configuration. In this case, there is still a high correlation with the ground temperature T_3 coming from the material modelling and it is possible to highlight that the ground temperatures before (T_1) and during the flight (T_2) have shown correlations with the seal leakage and collapse. For the 'best' design, the temperature should be employed to counteract unforeseen failures.

In fact, the term 'best' is written in quotation marks, because it is still possible to exhaust additional design candidates if further critical conditions are considered for the optimisation tasks. The range of input variables was mitigated in order to reduce the number of simulations and optimise the design for a couple of hypothetically severe scenarios. Despite the increasing sealing efficiency, the critical loading cases mainly took the effects of the relative striker displacements from fuselage deformation and rigging tolerances into account. Furthermore, it is still possible to evidence strong correlations with the lateral displacements R_x and M_x, which became smaller for displacements in the y direction, by comparing Tables 5.3 and 5.4 with Tables 6.7 and 6.8. The correlation coefficients reveal a manufacturing dependence in failure modes that were also as pronounced as the conceptual design. Confidence levels related to material inputs such as the coefficient of friction and the shore hardness of the elastomer are still present since they affect the structural stability. However, for the 'best' design, the increase in stiffness is directly related to leakage and collapse when looking at the SH_A column. Even in a linear analysis, buckling problems are challenging to be circumvented by simply increasing stiffness when the boundary conditions are unknown. An overall increase in stiffness does not prevent a lateral buckling, as the top wall (t_T) of the profile becomes less flexible to the cabin pressure outboard movement. In combination with a low coefficient of friction, the elastic behaviour might be constantly involved in the seal's performance, regardless of the design. It is important to recall that the material modelling relying on temperature effects was exaggerated so that the thermal boundary conditions would have some influence on the seal relaxation. Whereas studies apart from silicon rubber address the dependence of the Mooney-Rivlin parameters on the temperature [119] as well.

Even though material modelling is essential for FEM simulations of seals, the boundary conditions related to the striker displacement can be highlighted as the main sources of failure in the conceptual design. An increase from 49.0% to 93.1% of the sealing efficiency arises from the lower occurrence of leakage and collapse occurrences during valid runs. As much as the 'best' and original designs are highly similar in terms of aspect ratios, heights, and angles, minor changes to the wall thicknesses are very effective to improve the sealing efficiency against leakage. Ideally, the seal could be as rigid as possible to maintain cabin pressure. However, trade-offs between reaction forces and structural stability are important for the door operation as reducing the door closure force is reflected in decreasing the weight of the adjacent door and fuselage structures, which is crucial to an airliner's maximum take-off weight. Furthermore, as the seal design was based on solutions employed for PAX and CARGO doors, that are mostly operated by crew and ground staff, the forces must be within the operating limits. Thus, only inflatable seals were targeted for the design investigations to balance force and leakage. For a pure lip seal, contrasted with a hollow design in figure 1.2, the optimisation should be carried out without any problem due to the reduced number of design variables. Another possibility, instead of dealing with geometric parameters, could be to consider local reinforcements in parts of the cross-section of the seal. Figure 6.10 presents the design optimisation proposal that could also be used to modify the material stiffness based on 11 independent sections (S_i). By changing the hardness of the seal or adding fibre reinforcement, the profile could also be strengthened or weakened depending on the mechanical response.

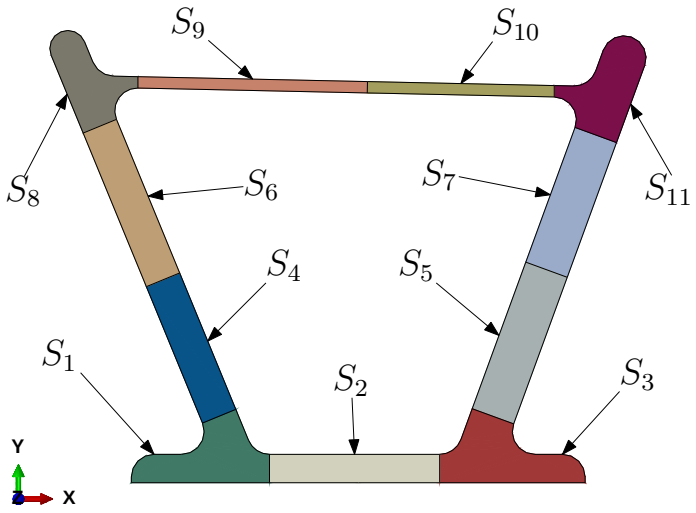

Figure 6.10. – Proposal for local reinforcements based on sections.

One topic that is not addressed in this work is the aspect of the corner and radii of the aircraft door seals. The load path is changed directly by the door contour and hence the striker interface frequently does not remain constant as it does in straight sections of the sealing line. A 2D plane-strain modelling approach provides a good representation of straight sections, which covers most of the interface between the door and fuselage. Previous studies with different types of striker geometries demonstrated that the contact pressures are disturbed simply by the seal profile sweep [74]. The modelling of curved sections can be realised with explicit analyses considering 3D FEM elements. However, this prevents the prescription of the internal cabin pressure with FPP interaction as discussed in Chapter 4. To demonstrate the complexity of these analyses, the seal geometry used in civil aircraft doors was simulated by only considering the striker closure kinematics. Figure 6.11 shows the contour plot of the seal deformation in the latched position, highlighting buckling areas along the seal.

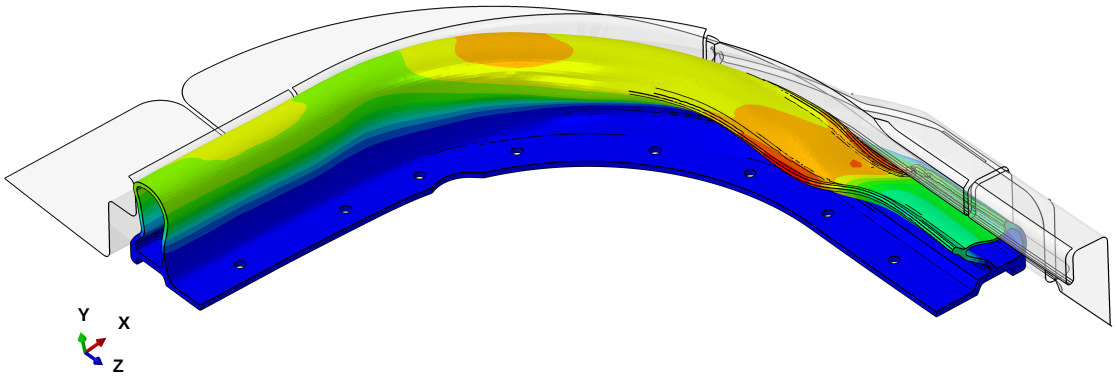

Figure 6.11. – Seal corner simulation employing the dynamic explicit solution.

From the computational cost perspective, an explicit dynamic simulation takes days to weeks to be concluded due to the number of elements and the small increments of time required by the scheme. As an informative note, the result of the 3D seal analysis presented took 2 days to complete using a 120-core cluster on a supercomputer. This type of analysis requires additional attention regarding material properties, as anisotropy might play an important role in the modelling of the elastomer component. The aircraft door seal specimens used in the characterization tests in Chapter 3 were extracted from the seal component shown in Figure 6.11. Due to confidentiality restrictions and agreements with the project partner, the seal's dimensions, the door type, and the aircraft model on which this component is employed are not mentioned in this work. Nevertheless, it is possible to grasp the number and complexity of the design features considered in a real seal and either in the seal geometry or the striker surface there should be manifold contact interactions that are not captured by 2D.

6.3.2. Method considerations

The applied method proved to be capable of generating quick solutions that can help in the development of seals with a robust design. Clearly, the presented work was focused on aircraft door sealing problems. However, the CAE tools employed in a combination of FEM with Parametric Optimisation can be extended to several types of elastomeric components. Tyres, dampers, shock absorbers, medical equipment and more sensitive seals used in nuclear power plants [120] are all suitable case studies for the development of safer designs using current commercial CAE tools. The level of automation and integration between analysis tools, along with user-friendly interfaces, allows structural engineers to analyse components more rapidly and systematically. Although not used to its full potential, the modules of the ISIGHT features include a range of optimisation techniques mostly based on model parametrisation. The justification behind avoiding the use of nonparametric optimization methods [121] lies in the difficulty to implement the process with nonlinear problems. Preliminary studies have been carried out with the TOSCA software [122] to evaluate the capabilities for obtaining a conceptual seal geometry with topology optimisation. Starting from a delimited design space using a fixed striker interface, the main problem is that convergence is not always reached, which yields to intermediary or unfeasible solutions from the manufacturing perspective. Figure 6.12 depicts a couple of trials with TOSCA using the topology optimisation process with different striking interfaces for an elastomeric seal enclosed in an initial design space of 40×40mm attached on the bottom. Both attempts display the contour plots with elements density varying between 0 and 1, to normalise the hyperelastic model parameters. The idea was to minimise the reaction force by compressing the seal across the section by 1mm with 50% of the initial mass as a constraint. However, both solutions are incomplete due to the divergence.

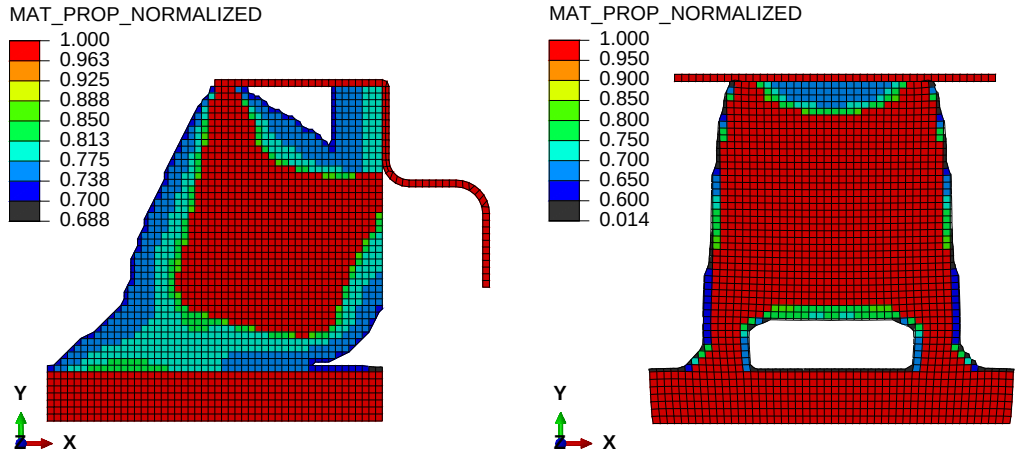

Figure 6.12. – Topology optimisation attempts with TOSCA.

Even though new 3D printing technologies with silicone are currently in development to produce complex geometries [123], it is hard to consider topology optimisation solutions as feasible designs. To ensure the seal's robustness, it is necessary to investigate the seal under various loading scenarios as done in the parametric studies. From boundary conditions that are not easily determined to nonlinear material modelling with contact problems, Multi-Parametric Optimisation operates in a more congruent and realistic manner with the design philosophies employed by seal manufacturers. On the other hand, designers have to start from an initial concept, which is based on the seal developer's experience. Neither genetic nor gradient-based algorithms are able to generate solutions from scratch; they can only provide suitable modifications to the design to increase the efficiency of sealing systems. Another aspect is that leakage and collapse indicators as part of the objective function are not easy to implement in the TOSCA tool as this software is not compatible with the CPRESS model outputs, which prevents seal efficiency improvements. Thus, considerations for optimisation tasks based on contact outputs may not be tangible.

The freedom of using various FEM inputs and outputs in the parametric process encourages different approaches to further optimise seal geometries while considering other objectives and design constraints. Safety factors and residuals were not given to the optimisation tasks but could be used as part of the multi-objectives to be, respectively, maximised and minimised by inserting additional optimisation loops. From previous studies using ISIGHT for designing the 'best' seal [77], the collapse constraint was formulated based on displacements instead of contact outputs. Material density integrated through the cross-section was also employed for the weight reduction of the sealing component. Apart from the option of effortlessly updating multi-objectives for nonlinear and discontinuous design spaces, various optimisation techniques can be used in parallel. A library of exploratory (DOE), evolutionary (NSGA-II) and numerical (LSGRG) techniques facilitates to balancing algorithm capabilities. In fact, DOE could also be employed to optimise the seal geometry, although it would require too many simulations to cover the completeness of design spaces. Neither a factorial combination nor a Latin Hypercube would select small design nuances to improve the seal's efficiency. A DOE should thus be the method of choice to start surface based approximations. However, as seen by the optimisation runs with NSGA-II, the number of unfeasible runs does not allow fitting representative meta-models with polynomial order functions. Despite not being well-suited for long simulations since all the runs are not fully independent, NSGA-II is faster than standard genetic techniques. The main issue is that the start population can influence the 'best' design candidates for a reduced number of simulations, resulting in different solution variants each time the process is randomly initiated, and hence discretion is advised when comparing multiple results to select a single candidate. On the other hand, while LSGRG is faster than the other techniques, it is even more dependent on the initial design due to the convergence criteria of the method. Despite having different philosophies, genetic algorithms combined with gradient-based methods may achieve satisfactory results.

7. Summary and outlook

This work presented relevant topics to contribute to the development of door seals essentially applied in civil aircraft. The main idea was to derive the methods for the analyses and to understand the physical quantities that govern the seal performance based on CAE tools. Despite superficially covering research topics of FEM modelling to structural optimisation, the commercial tool ABAQUS was employed to highlight the analysis capabilities using stress, displacements and contact pressure from different solutions, such as static, dynamic, and temperature coupling. Each chapter was structured to add elements for the quantification of variables towards the goal of finding the 'best' seal solution from a conceptual design. The efficiency improvement of an elastomeric seal using 2D simulations was restricted to a virtual environment, that still requires validations on a component level. Nevertheless, material investigations served as a fundament to start the simulations from the analytical formalism of continuum mechanics. By means of uniaxial tests, hyper-viscoelastic material models were fitted according to the loading conditions of elastomeric door seals. Due to a lack of experiments with temperature and load conditions, the gaps to be filled should be covered by future research on reinforced silicone seals. Subsequently, a recapitulation of the key findings is presented in the following.

Chapter 1 discusses the thematic aspects of aircraft door seals. The requirements are basically related to leakage and operability, with a strong dependency on the boundary conditions and design philosophy. Due to the cabin pressure in cruise flights, the motivations arise from the necessity for a robust solution against external disturbances, to avoid air leakage and cabin depressurisation. In Section 1.2 a strategy was developed to understand the physical quantities that can play a role in the mechanical behaviour of seals. For this purpose, the planning of experiments, tools, and working points was outlined in an analysis process diagram. Based on references on the current state of the art regarding elastomers and material modelling, it is indispensable to formalise the motion and deformation description of an elastic body. Chapter 2 introduces the basics of continuum mechanics. By assuming the existence of a deformation gradient, the constitutive relations are described in current and original configurations under a mechanical process. Free-energy models based on the first two invariants from the deformation gradient were envisaged given their suitability in FEM tool ABAQUS. Incomperssibility and isotropy aspects were supported by tests and known phenomena concerning elastomers. Furthermore, the linear viscoelastic theory was proposed under assumptions only considering temperature effects of stress relaxation based on Prony series.

Chapter 3 supports the material theory regarding hyper- and viscoelastic modelling based on experimental findings from uniaxial load conditions. The limit of 50% of strain was employed for parametric identification in quasi-static and relaxation processes. Furthermore, an ultimate strength of 8MPA in engineering stress was estimated for the silicone samples with a single rupture test. The generalised form of the Mooney-Rivlin free-energy was employed, resulting in a conservative representation by model 4 with two parameters (C_{10} and C_{02}). Another fit was done for the relaxation test by adding multiple series of Prony as a kernel function for the fading memory functional depending on two parameters in each summation term. Therefore, it was concluded that at least seven Maxwell elements in parallel were necessary. By fixing the relaxation times (τ_i), the dimensionless coefficients (g_i) were fitted to represent the transient dissipative behaviour of the seal. Some hypotheses were made to incorporate the material and process changes of the silicone, as well as the temperature behaviour. Mostly driven by the Shore hardness A, the first hyperelastic material parameter may affect the linear elastic moduli, while the WLF function was introduced using an exaggerated glass transition temperature of -60° for the silicone.

Chapter 4 evokes the FEM analysis principles for the model using a conceptual door seal design. By assuming the relevant boundary conditions in a flight mission, the simulation steps were constructed to cover different ground and flight conditions, including manoeuvrers during a long-range mission. Therefore, the models inputs were parametrised in ABAQUS to be managed by the ISIGHT tool. Basic control options are explained, notably by highlighting the importance of pressure load definition by contact interactions. Due to the necessity of using an implicit scheme for the FPP, a combination of transient static and dynamic solutions was exploited to apply the pressure load while avoiding divergence problems. Mesh size and test comparisons with FEM models were made to increase the level of confidence in the numerical solutions. The outputs coming from FEM analysis were post-processed to obtain the performance indicators: force, leakage, collapse, safety factors and residual displacement. These results were further combined with DOE and Parametric Optimisation in Chapters 5 and 6 for design improvements. These last two analysis chapters explored different techniques in the design space of boundary conditions (displacement and temperature) and material and geometry of the seal. The goal of increasing seal efficiency started by understanding the influencing factors on seal performance. By using the DOE with 500 simulations from an Optimised Latin Hypercube sampling technique, the critical loading cases were filtered using of Spearman's correlation coefficients. With a confidence interval of 99.9%, a mitigation of the input variables was performed to assume three scenarios for the optimisation whereby the genetic algorithm NSGA-II was considered for the first optimisation rounds to minimise the leakage and force together, within a fixed design space while avoiding collapse occurrences. Additionally, two design candidates were refined by using LSGRG gradient-based technique in a 'best' design choice, after an evaluation of the results and a DOE re-run.

Open points concerning the material modelling, simulations, and optimisation techniques are recalled in this last paragraph. This work combined research topics to improve a seal design in a superficial but meaningful way. Concerning the material modelling topic, it is still necessary to look deeper into the behaviour of fibre-reinforced elastomers. Experiments in multiple directions as well as in other loading modes are necessary for the consideration of anisotropy and at least shear or biaxial tests should be employed to identify the material model parameters of the elastic behaviour in multiple directions. In addition, the effect of temperature may also play an important role in the elastic mechanical characteristics of elastomers as previously mentioned. A modelling approach that takes at least two flight cycles of the aircraft into account would be ideal for capturing the influence of the deformation history from one flight to another. Considering the long time span of an aircraft's structural goal, damage and ageing effects should not be neglected for understanding the behaviour of the seal and these may be incorporated in further research by means of user defined subroutines for transient models. In fact, time was an important aspect of this work in the attempt to reduce the number of simulations for the calculations. Although 2D models were easily parametrised for the optimisation rounds, this simplification that was made to increase the data acquisition does not cover problematic parts of the seal on the door corner areas. Further development of optimisation tools with nonparametric methods may be important to develop robust seals, even for complex 3D nonlinear simulations. Nevertheless, a reduced number of computational experiments based on DOE is a good starting point to understand the influencing variables on seal performance.

List of Figures

1.1. Running loads of an aircraft. 2
1.2. Seal and striker design philosophies: lip (left) and hollow (right). 3
1.3. Diagram with tools, analysis topics and working points. 6

2.1. Representation of the reference and current configurations. 9
2.2. Polar decomposition of the deformation gradient. 11
2.3. Internal forces acting on an infinitesimal surface element vectors. 15
2.4. Free-body on reference and current configurations. 17
2.5. Generalised Maxwell model and rheological elements. 28
2.6. Constrained minima under linear constraints. 34
2.7. *Pareto* optimal solutions are located within points P and Q. 35
2.8. General process with controlled and uncontrolled inputs. 37
2.9. *Latin square* example for the generalisation of the Latin hypercube. . . 38

3.1. Diagram with the test levels considered for aircraft certification. 41
3.2. Sample cutting directions and main dimensions in mm. 42
3.3. Average stress from 2×5 samples based on the cutting direction. 43
3.4. Fitted material models with MSE values obtained with *NMinimize*. . . 46
3.5. Stress-strain results to rupture (left) based on one sample (right). . . . 47
3.6. Relaxation process with a deformation step of $\lambda = 1.5$ for 12 hours. . . 48
3.7. Relaxation modulus from test data to fitted kernel functions. 49
3.8. Gent's relationship between Young's modulus and hardness. 50
3.9. Stress curves based on different hardness degrees for door seals. 51
3.10. Relaxation modulus employing the WLF shift function. 52

4.1. Seal prototype (solid) and rigid striker (dashed) cross sections [77]. . . 54
4.2. Contact interactions with 3 slave surfaces on the seal and 1 master rigid striker surface (Pairs: $M_1 - S_1$ (FPP) and $M_1 - S_2$; Self contact: $S1$ and S_3). 56
4.3. Mission profile of a civil aircraft. 58
4.4. Unit cube element outputs from the relaxation step. 62
4.5. Comparison of the stress from the FEM and relaxation test data. . . . 62
4.6. Logarithmic strain (LE) and reaction force (RF) on the rigid striker. . . 64
4.7. Contact pressure (CPRESS) close-up view showing the refinement. . . . 64
4.8. Reaction force measured over 30min with peaks at first 10s. 67

4.9. Reaction force influences of rigging tolerances. 67
4.10. First instants after the cabin pressure starts to increase. 69
4.11. Cabin pressure that is reached with the maximum differential. 69
4.12. Seal profile (about to collapse) that is part of a leakage scenario. 70
4.13. First instants of the seal without contact with the striker. 71
4.14. Fully collapsed seal in an irreversible configuration. 72
4.15. Two stress measurements from for safety evaluation. 73
4.16. Residual displacement due to creeping process. 74

5.1. Process components in the ISIGHT interface for the DOE. 77
5.2. Sampling concepts illustrated for a DOE configuration with two variables and four design points employing different techniques from ISIGHT. 78
5.3. Striker displacement envelope in U_y used for optimisation runs. 85

6.1. Components of the ISIGHT interface for the Optimisation. 88
6.2. Optimisation results for three random seeds with NSGA-II. 91
6.3. *Pareto*-optimal front from NSGA-II between objectives. 92
6.4. Seal design candidates compared to the original concept profile. 93
6.5. Design refinement with selected variants using LSGRG. 95
6.6. Variants B* (left) and C* (right) at the initial compression stage. 96
6.7. Variants B* (left) and C* (right) at the maximum seal compression. . . 96
6.8. Variants B* (left) and C* (right) respecting the collapse. 97
6.9. Variants B* (left) and C* (right) with a reduced leakage index. 97
6.10. Proposal for local reinforcements based on sections. 101
6.11. Seal corner simulation employing the dynamic explicit solution. 102
6.12. Topology optimisation attempts with TOSCA. 103

List of Tables

2.1. Optimisation techniques according to operation research methods. . . . 35

3.1. Identified parameters for the four material models. 46
3.2. Identified coefficients for the linear viscoelasticity models. 49

4.1. Initial design values for the seal prototype. 55
4.2. Analysis sequence of a flight mission with time step durations. 59
4.3. FEM material model parameters given to ABAQUS. 61
4.4. Mesh convergence results from FEM outputs used for seal analysis. . . 65
4.5. Seal performance indicators summary for the next chapters. 74

5.1. Maximum and minimum ranges of the design matrix for the DOE. . . . 76
5.2. Efficiency calculated from sealed runs categorised by valid samples. . . 80
5.3. Spearman's rank correlation between the inputs and outputs. 82
5.4. Confidence levels based on Spearman's ranks with $N = 478$. 83

6.1. Design parameters' range of the door seal optimisation. 87
6.2. NSGA-II standard parameters employed for optimisation in ISIGHT. . 90
6.3. Design parameters extracted from each NSGA-II optimisation round. . 91
6.4. LSGRG custom parameters employed for the optimisation algorithm. . 94
6.5. Design parameters refined with the LSGRG optimisation algorithm. . . 95
6.6. Comparisons between 'best' and concept designs with DOE runs. . . . 98
6.7. Spearman's correlation of the DOE trial with the 'best' design. 99
6.8. Confidence levels based on Spearman's ranks with $N = 495$. 99

A.1. Design matrix containing all 500 samples for DOE simulations. 120

References

[1] FAA. *14 CFR 25.365 - Pressurized compartment loads.* Tech. rep. 1. Washington, D.C., United States: Federal Aviation Administration, 2011, pp. 414–415.

[2] EASA. *Certification Specifications and Acceptable Means of Complience for Large Aeroplanes CS-25.* Tech. rep. June. European Aviation Safety Agency, 2016, pp. 73 –74.

[3] ATSB. *Aircraft Depressurisation - Report AR-2008-075(2).* Tech. rep. January. Aviation Research and Analysis, 2009, pp. 1–8.

[4] M Lacagnina. "Losing the Cabin - Insights on civil aircraft depressurization". In: ed. by Aviation Safety World. October. Aviation Safety World, 2006, pp. 33–41.

[5] K. Hibbitt. "ABAQUS/Standard: User's Manual: Version 5.6". In: (1996).

[6] D. Feldman. "Polymer history". In: *Designed Monomers and Polymers* 11.1 (2008), pp. 1–15.

[7] ASTM D1418-21a. *Standard Practice for Rubber and Rubber Latices—Nomenclature.* West Conshohocken, PA, 2021.

[8] C. A. and others Subcommittee, A. M. Association, and A. S. Committee. "Cabin cruising altitudes for regular transport aircraft". In: *Aviation Space and Environmental Medicine* 79.4 (2008), pp. 433–439.

[9] J. T. Bauman. *NoFatigue, stress, and strain of rubber components: guide for design engineers.* Carl Hanser Verlag GmbH Co KG, 2012.

[10] D. Young, W.A., Shaw, D.B. and Bates. "Presence of ozone in aircraft flying at 35,000 feet". In: *Aerospace Medicine* (1962), pp. 311–318.

[11] G. Simons. *Comet! The World's First Jet Airliner.* Pen and Sword, 2013.

[12] W. Rogers, N. Armstrong, and E. Al. *Report of the Presidential Commission on the Space Shuttle Challenger Accident, The Cause of the Accident. R. Commission.* Tech. rep. Washington, DC, United States: NASA, 1986.

[13] F. Sidoroff. *Cours sur les grandes déformations.* 51. Sophia-Antipolis, 1982.

[14] G. Holzapfel. *Nonlinear Solid Mechanics: A Continuum Approach for Engineering Science.* 2000.

[15] L. Treloar. “The elasticity of a network of long-chain molecules. I”. In: *Transactions of the Faraday Society* 36 (1942), pp. 36–41.

[16] L. Treloar. *The elasticity of a network of long-chain molecules—II*. 1943.

[17] L. R. Treloar. *Mechanics of Rubber Elasticity*. 1976.

[18] M. Mooney. “A theory of large elastic deformation”. In: *Journal of Applied Physics* 11.9 (1940), pp. 582–592.

[19] W. Coleman, Bernard D and Noll. “Foundations of linear viscoelasticity”. In: *Reviews of modern physics* 33.2 (1961), p. 239.

[20] B. D. Coleman and M. E. Gurtin. “Thermodynamics with internal state variables”. In: *The Journal of Chemical Physics* 47.2 (1967), pp. 597–613.

[21] W. Coleman, Bernard D and Noll. *The thermodynamics of elastic materials with heat conduction and viscosity*. 1974.

[22] J. G. Oldroyd. “On the formulation of rheological equations of state”. In: *Proceedings of the Royal Society of London. Series A. Mathematical and Physical Sciences* 200.1063 (1950), pp. 523–541.

[23] R. Renaud, Franck and Dion, Jean-Luc and Chevallier, Gaël and Tawfiq, Imad and Lemaire. *A new identification method of viscoelastic behavior: Application to the generalized Maxwell model*. 2011.

[24] A Haupt, P and Lion. “A generalisation of the Mooney-Rivlin model to finite linear viscoelasticity”. In: *Constitutive Models for Rubber* 2 (2001), pp. 57–64.

[25] A. Lion. “On the large deformation behaviour of reinforced rubber at different temperatures”. In: *Journal of the Mechanics and Physics of Solids* 45.11-12 (1997), pp. 1805–1834.

[26] J. D. Williams, Malcolm L and Landel, Robert F and Ferry. *The temperature dependence of relaxation mechanisms in amorphous polymers and other glass-forming liquids.* 1955.

[27] A. V. Tobolsky. “Stress relaxation studies of the viscoelastic properties of polymers”. In: *Journal of Applied Physics* 27.7 (1956), pp. 673–685.

[28] V. Sivakumar and R. Palaninathan. “FE Analysis of Contact Pressure Prediction on O-Rings Used in Solid Rocket Booster Segment Joints”. In: *International Journal of Science and Engineering Applications* 1.1 (2012), pp. 8–16.

[29] M. Marc. *Nonlinear finite element analysis of elastomers*. 2005.

[30] R. S. Rivlin. *Large elastic deformations of isotropic materials IV. Further developments of the general theory*. 1948.

[31] R. S. Rivlin. *Large elastic deformations of isotropic materials. V. The problem of flexure*. 1948.

[32] R. S. Rivlin. *Large elastic deformations of isotropic materials VI. Further results in the theory of torsion, shear and flexure.* 1949.

[33] R. W. Ogden. "Large Deformation Isotropic Elasticity - on the Correlation of Theory and Experiment for Incompressible Rubberlike Solids." In: *Rubber Chemistry and Technology* 46.2 (1973), pp. 398–416.

[34] W. Zhu, J. Wang, and P. Lin. "Numerical analysis and optimal design for new automotive door sealing with variable cross-section". In: *Finite Elements in Analysis and Design* 91 (2014), pp. 115–126.

[35] Q. Liu et al. "Elastic leak of a seal". In: *Extreme Mechanics Letters* 1 (2014), pp. 54–61.

[36] B. N. Persson et al. "Elastic contact mechanics: Percolation of the contact area and fluid squeeze-out". In: *European Physical Journal E* 35.1 (2012).

[37] Y. Dong et al. "Effect of stress relaxation on sealing performance of the fabric rubber seal". In: *Composites Science and Technology* 151 (2017), pp. 291–301.

[38] N. Morrison, Y. Gorash, and R. Hamilton. "Comparison of single-solver fsi techniques for the FE-prediction of a blow-off pressure for an elastomeric seal". In: *ECCM – ECFD 2018 CONFERENCE* June (2018).

[39] B. Zhao et al. "Sealing performance analysis of P -shape seal with fluid pressure penetration loading method". In: *IOP Conference Series: Materials Science and Engineering* 397.1 (2018).

[40] Y. Gorash, A. Bickley, and F. Gozalo. "Improvement of leak tightness for swellable elastomeric seals through the shape optimization". In: *Constitutive Models for Rubber X - Proceedings of the 10th European Conference on Constitutive Models for Rubber, ECCMR X 2017* 2013 (2017), pp. 453–458.

[41] S. M. Myers, Raymond H and Montgomery, Douglas C and Vining, G Geoffrey and Borror, Connie M and Kowalski. *Response surface methodology: a retrospective and literature survey.* 2004.

[42] K. Sigmund, Ole and Maute. *Topology optimization approaches.* 2013.

[43] D. C. Montgomery. *Design and analysis of experiments.* John wiley & sons, 2017.

[44] J. De Winter, Joost CF and Gosling, Samuel D and Potter. "Comparing the Pearson and Spearman correlation coefficients across distributions and sample sizes: A tutorial using simulations and empirical data." In: *Psychological methods* 21.3 (2016), p. 273.

[45] T. Deb, Kalyanmoy and Pratap, Amrit and Agarwal, Sameer and Meyarivan. *A fast and elitist multiobjective genetic algorithm: NSGA-II.* 2002.

[46] J. R. Kennedy, Graeme J and Martins. *A parallel finite-element framework for large-scale gradient-based design optimization of high-performance structures*. 2014.

[47] P. Van der Velden, Alex and Koch. "Isight design optimization methodologies". In: *ASM handbook* 22 (2010), p. 79.

[48] C. Bucher and J. Will. "Multidisciplinary non-linear optimization with Optimizing Structural Language OptiSLang". In: *19th CAD-FEM Users' Meeting International Congress on FEM Technology* (2001), pp. 1–11.

[49] P Haupt. *Continuum Mechanics and Theory of Materials*. Berlin: Springer-Verlag, 2000.

[50] P Haupt and A Lion. "On finite linear viscoelasticity of incompressible isotropic materials". In: *Acta Mech.* 159 (2002), pp. 87–124.

[51] S. S. Rao. *Engineering optimization: theory and practice*. John Wiley & Sons, 2019.

[52] S. J. Nocedal, Jorge and Wright. *Numerical optimization*. Springer, 1999.

[53] J. Antony. "Introduction to Industrial Experimentation". In: *Design of Experiments for Engineers and Scientists* (2014), pp. 1–6.

[54] P. Haupt. *Continuum Mechanics and Theory of Materials*. 2002.

[55] P Germain. *Mécanique 1&2. Cours de l'Ecole Polytechnique*. 1986.

[56] C. Truesdell and R Toupin. *The classical field theories*. In S. Flügge (Herausgeber), Handbuch der Physik III/1, Springer-Verlag, Berlin, 1960, pp. 2226–2793.

[57] B. Coleman and W Noll. "The thermodynamics of elastic materials with heat conduction and viscosity". In: *Arch. Rat. Mech. Anal.* 13 (1963), pp. 167–178.

[58] S Hartmann et al. "Large Deformations of a Carbon Black-Filled Rubber; Experiment, Optical Measurement and Parameter Identification Using Finite Elements". In: *Eur. J. Mech., A/Solids* 22 (2003), pp. 309–324.

[59] M Šilhavý. *The Mechanics and Thermodynamics of Continuous Media*. Springer-Verlag, Berlin, 1997.

[60] P. Flory. "Thermodynamic relations for hight elastic materials". In: *T. Faraday Soc.* 57 (1961), pp. 829–838.

[61] O.H. Yeoh and P.D. Flemming. "A new attempt to reconcile the statistical and phenomenological theories of rubber elasticity". In: *Journal of Polymer Science Part B: Polymer Physics* 35 (1997), pp. 1919–1931.

[62] S. Hartmann. "Numerical studies on the identification of the material parameters of Rivlin's hyperelasticity using tension-torsion tests". In: *Acta Mechanica* 148 (2001), pp. 129–155.

[63] D. C. Drucker. “A definition of stable inelastic material”. In: *American Society of Mechanical Engineers* (1959).

[64] P. Steinmann, M. Hossain, and G. Possart. “Hyperelastic models for rubber-like materials: Consistent tangent operators and suitability for Treloar’s data”. In: *Archive of Applied Mechanics* 82.9 (2012), pp. 1183–1217.

[65] B. Coleman and W Noll. “Foundations of linear viscoelasticity”. In: *Reviews of Modern Physics* 33 (1961), pp. 239–249.

[66] P Haupt and A Lion. “A generalisation of the Mooney-Rivlin model to finite linear viscoelasticity”. In: *Constitutive Models for Rubber II: Proceedings of the 2th European Conference on Constitutive Models for Rubber*. Ed. by D Besdo, R. Schuster, and J Ihlemann. London: Swets and Zeitlinger, 2001, pp. 57–64.

[67] M. L. Williams, R. F. Landel, and J. D. Ferry. “The Temperature Dependence of Relaxation Mechanisms in Amorphous Polymers and Other Glass-forming Liquids”. In: *J Am Chem Soc* 77.14 (1955), pp. 3701–3707.

[68] M. W. Lasdon, Leon S and Fox, Richard L and Ratner. “Nonlinear optimization using the generalized reduced gradient method”. In: *Revue française d’automatique, informatique, recherche opérationnelle. Recherche opérationnelle* 8.V3 (1974), pp. 73–103.

[69] M. Barton, Russell R and Meckesheimer. *Metamodel-based simulation optimization*. Vol. 535–574. 2006. Elsevier, 13.

[70] J. A. Authorities. “Joint aviation requirements. JAR-25. Large aeroplanes”. In: *Civil Aviation Authority Printing & Publication Services, Greville House* 37 (1994).

[71] A. FAA. “AC 20-107B, Composite Aircraft Structure”. In: *US Department of Transportation Federal Aviation Administration* (2009).

[72] D. D. I. für Normung. *Testing of rubber - Determination of tensile strength at break, tensile stress at yield, elongation at break and stress values in a tensile test (DIN 53504:2017-03)*. Berlin, 2017.

[73] D. D. I. für Normung. *Linear viscoelastic materials; concepts, constitutive equations, basic functions (DIN 13343:1994-04)*. Berlin, 1994.

[74] B. Franke Goularte et al. “Elastomeric door seal analysis under aircraft cabin pressure”. In: *Journal of Rubber Research*. Vol. 24. 2. Springer Singapore, 2021, pp. 301–318.

[75] S. Lejeunes. “Modélisation de structures lamifiées élastomère-métal à l’aide d’une méthode de réduction de modèles”. PhD thesis. Université de la Méditerranée-Aix-Marseille II, 2006, pp. 38–43.

[76] D. D. I. für Normung. *Plastics - Determination of tensile properties - Part 1: General principles (ISO 527-1:2019)*. Berlin, 2012.

[77] B. F. Goularte; V. M. Bruère; A. Lion; M.Johlitz. “Multiparametric design optimisation of 3D printed aircraft door seals”. In: *Munich Symposium on Lightweight Design 2021*. 2021.

[78] A. Champion, Brett and Strzebonski. “Wolfram Mathematica Tutorial Collection CONSTRAINED OPTIMIZATION”. In: *United States of America* (2008).

[79] F. Bueche. “Mullins effect and rubber-filler interaction”. In: *J. Appl. Polymer Sci.* 5 (1961), pp. 271–281.

[80] A Haupt, P and Lion. “Finite viscoelasticity: a physical approach based on relaxation spectra, fractional derivatives and process-dependent viscosities”. In: *CONSTITUTIVE MODELS FOR RUBBER* 2 (2001), pp. 65–72.

[81] J. Warrick, EL and Pierce, OR and Polmanteer, KE and Saam. “Silicone elastomer developments 1967–1977”. In: *Rubber chemistry and Technology* 52.3 (1979), pp. 437–525.

[82] K. Larson. “Can you estimate modulus from durometer hardness for Silicones?” In: *Dow Corning Corporation* (2016), pp. 1–6.

[83] A. N. Gent. “On the relation between indentation hardness and Young’s modulus”. In: *Rubber Chemistry and Technology* 31.4 (1958), pp. 896–906.

[84] A. R. Babu and N. Gundiah. “Role of Crosslinking and Entanglements in the Mechanics of Silicone Networks”. In: *Experimental Mechanics* 54.7 (2014), pp. 1177–1187.

[85] P Meier et al. “Uniaxial and equi- biaxial tension tests of silicone elastomer”. In: *Constitutive Models for Rubber III* (2003), pp. 99–106.

[86] N. Elango et al. “Determination of non-linear material constants of RTV silicone applied to a soft actuator for robotic applications”. In: *Key Engineering Materials* 594-595 (2014), pp. 1099–1104.

[87] D. J. Charlton, J. Yang, and K. K. Teh. *Review of methods to characterize rubber elastic behavior for use in finite element analysis*. 1994.

[88] F. Fan and Y. H. Roos. “Glass Transition-Associated Structural Relaxations and Applications of Relaxation Times in Amorphous Food Solids: a Review”. In: *Food Engineering Reviews* 9.4 (2017), pp. 257–270.

[89] D.-I. H. Domininghaus. *Kunststoffe: Eigenschaften und Anwendungen*. Springer-Verlag, 2013.

[90] V. Cowie, John Mackenzie Grant and Arrighi. *Polymers: chemistry and physics of modern materials*. CRC press, 2007.

[91] D. R. Brandrup, Johannes and Immergut, Edmund H and Grulke, Eric A and Abe, Akihiro and Bloch. *Polymer handbook*. Vol. 89. Wiley New York, 1999.

[92] P. Ehrenstein, Gottfried W and Riedel, Gabriela and Trawiel. *Thermal analysis of plastics: theory and practice*. Carl Hanser Verlag GmbH Co KG, 2012.

[93] S Kaisersberger, E and Knappe, S and Möhler, H and Rahner. "TA for polymer engineering". In: *NETZSCH annual for science and industry* 2 (1993).

[94] S. Atmosphere. "International organization for standardization". In: *ISO* 2533 (1975), p. 1975.

[95] S. ho Yoon and C. R. Siviour. "Application of the Virtual Fields Method to a relaxation behaviour of rubbers". In: *Journal of the Mechanics and Physics of Solids* 116.2003 (2018), pp. 416–431.

[96] S. A. Ashter. *Thermoforming of Single and Multilayer Laminates: Plastic Films Technologies, Testing, and Applications*. William Andrew, 2013.

[97] P. J. Roache. "Perspective: A method for uniform reporting of grid refinement studies". In: *Journal of Fluids Engineering, Transactions of the ASME* 116.3 (1994), pp. 405–413.

[98] P. Wriggers. *Nonlinear finite element methods*. Springer Science & Business Media, 2008.

[99] H. Hilber, T. Hughes, and R. Taylor. "Improved numerical dissipation for time integration algorithms". In: *Earthquake Engineering and Structural Dynamics* 5 (1977), pp. 283–292.

[100] J. M. Belytschko, Ted and Ong, Jame Shau-Jen and Liu, Wing Kam and Kennedy. *Hourglass control in linear and nonlinear problems*. 1984.

[101] T. J. R Hughes. *The Finite Element Method, Linear Static and Dynamic Finite Element Analysis*. New Jersey:Prentice-Hall, 1987.

[102] L. F. Richardson. "The approximate arithmetical solution by finite differences with an application to stresses in masonry dams". In: *Philosophical Transactions of the Royal Society of America* 210 (1911), pp. 307–357.

[103] EASA. *Modelling and Simulation – CS-25 Structural Certification Specifications*. Tech. rep. European Aviation Safety Agency, 2020, CM–S–014 Issue 01.

[104] J. Ordieres-Meré et al. "Finite element analysis of the hyper-elastic contact problem in automotive door sealing". In: *Journal of Non-Crystalline Solids* 354.47-51 (2008), pp. 5331–5333.

[105] Parker. *ParFab TM Design Guide - Extruded and Hot Vulcanized Gaskets*. 2014.

[106] Q. Zhang et al. "An experimental study of the leakage mechanism in static seals". In: *Applied Sciences (Switzerland)* 8.8 (2018), pp. 1–15.

[107] E. F. Bruhn. *Analysis and design of flight vehicle structures*. Tri-state offset company, 1965.

[108] R. J. Boulbes. *Troubleshooting Finite-Element Modeling with Abaqus*. Lyon, France: Springer, 2020.

[109] T. J. Morris, Max D and Mitchell. *Exploratory designs for computational experiments*. 1995.

[110] A. B. Owen. "Orthogonal arrays for computer experiments, integration and visualization". In: *Statistica Sinica* (1992), pp. 439–452.

[111] A. Jin, Ruichen and Chen, Wei and Sudjianto. *An efficient algorithm for constructing optimal design of computer experiments*. 2005.

[112] M. E. Johnson, L. M. Moore, and D. Ylvisaker. "Minimax and maximin distance designs". In: *Journal of Statistical Planning and Inference* 26.2 (1990), pp. 131–148.

[113] D. J. Croxton, Frederick E and Cowden. "Applied general statistics." In: *Prentice-Hall, Inc* (1939).

[114] P. H. Ramsey. "Critical Values for Spearman's Rank Order Correlation". In: *Journal of Educational Statistic* 14.3 (1989), pp. 245–253.

[115] J. I. Hahn, Youngwon and Cofer IV. "Study of parametric and non-parametric optimization of a rotor-bearing system". In: *Turbo Expo: Power for Land, Sea, and Air*. American Society of Mechanical Engineers, 2014, V07AT28A001.

[116] S. Nayak. *Fundamentals of Optimization Techniques with Algorithms*. Academic Press, 2020.

[117] K. N. Dutta, Saykat and Das. *Problems, A survey on pareto-based eas to solve multi-objective optimization*. 2019.

[118] H. Du et al. "Elitism and distance strategy for selection of evolutionary algorithms". In: *IEEE Access* 6 (2018), pp. 44531–44541.

[119] T. L. Smith. "Large Deformation Tensile Properties of Elastomers. I. Temperature Dependence of C1 and C2 in the Mooney-Rivlin Equation". In: *Rubber Chemistry and Technology* 41.5 (1968), pp. 1231–1243.

[120] S Wittich, KC and Wensel, R and Larose, R and Kuran. *Upgrading elastomer seals for nuclear service*. Tech. rep. Atomic Energy of Canada Ltd., 1995.

[121] G. and others Krog, Lars and Tucker, Alastair and Rollema. "Application of topology, sizing and shape optimization methods to optimal design of aircraft components". In: *Proc. 3rd Altair UK HyperWorks users conference*. 2002.

[122] F. Saleem, Waqas and Lu, Hu and Yuqing. "Topology Optimization-Problem Formulation and Pragmatic Outcomes by integration of TOSCA and CAE tools". In: *Proceedings of the World Congress on Engineering and Computer Science*. 2008, p. 24.

[123] M. J. Vivianne M Bruere, Alexander Lion, Jens Holtmannspötter. “An Overview on the 3D Printing of Elastomers and the Influence of Printing Parameters on their Mechanical Properties”. In: *Lectures Notes on Advanced Structured Materials*. 2022.

A. Appendix 1

Table A.1. – Design matrix containing all 500 samples for DOE simulations.

Run#	R_x	R_y	P_x	P_y	M_x	M_y	SH_A	μ	T_1	T_2	T_3
1	2.2	1.9	-6.1	-0.3	-4.9	-3.1	53.0	0.3	-9.7	-16.6	19.3
2	-2.7	3.5	-3.6	-2.0	-5.7	-3.5	56.0	0.3	37.6	-37.5	38.4
3	-3.7	3.6	-3.3	-0.3	1.4	-3.6	55.5	0.2	-22.0	-19.5	-8.4
4	-1.6	-1.0	-4.5	-0.1	-6.1	-3.8	55.1	0.3	-28.1	-18.3	-35.2
5	2.9	3.2	-0.9	-1.8	-4.3	-3.9	54.6	0.3	-6.8	-15.7	-21.4
6	0.6	-1.1	-0.5	-0.7	-6.6	-3.9	52.8	0.2	22.4	-43.8	20.0
7	-0.5	3.6	-6.2	-3.2	-3.4	-3.8	51.6	0.2	23.2	-17.9	7.0
8	2.2	-1.3	-6.6	-1.8	2.5	-3.2	52.8	0.2	-33.0	-37.2	26.4
9	0.3	3.0	-1.9	-2.7	3.4	-3.0	53.4	0.2	38.9	-31.8	15.0
10	1.6	0.2	-2.4	-1.9	-0.3	-3.1	60.0	0.2	-30.5	-48.9	3.8
11	-3.0	-1.2	-3.2	-0.2	-1.0	-3.2	51.3	0.4	-32.1	-35.5	-20.4
12	0.7	2.9	-0.4	-3.2	-1.8	-3.5	53.3	0.2	-35.8	-42.5	-28.3
13	3.1	1.0	-1.7	-3.8	1.4	-3.1	52.0	0.2	4.4	-28.2	-33.3
14	3.2	1.2	-0.3	-3.7	-5.0	-3.4	55.4	0.3	5.1	-39.6	38.6
15	-2.5	1.0	-5.9	-1.7	-5.3	-3.8	58.4	0.1	-30.2	-30.7	2.8
16	-3.0	-0.5	-1.8	-2.3	1.9	-3.2	50.5	0.2	-31.2	-45.0	-5.2
17	0.4	2.9	-4.1	-2.6	-7.1	-3.6	53.8	0.4	22.7	-48.1	-27.5
18	-3.1	2.6	-3.8	-3.1	2.0	-3.2	51.4	0.3	18.8	-48.5	-0.1
19	-0.5	2.2	-0.6	-0.3	-0.2	-3.4	53.4	0.3	-34.9	-49.0	11.9
20	-3.3	3.4	-0.9	-1.0	1.9	-3.2	52.9	0.3	-2.7	-36.8	-33.6
21	2.0	0.8	-5.1	-1.4	-5.3	-3.0	57.7	0.4	-37.3	-33.0	6.2
22	-2.4	1.3	-3.9	-1.8	4.7	-3.0	55.0	0.4	-4.1	-23.7	-11.0
23	3.2	1.2	-6.4	-2.1	3.0	-3.8	58.2	0.4	11.3	-37.4	12.3
24	2.7	-2.0	-3.3	-2.6	-2.4	-3.7	58.5	0.3	37.9	-47.0	-31.2
25	-2.6	2.3	-0.7	-3.5	3.0	-3.3	57.0	0.2	4.3	-18.6	-31.3
26	-2.9	-1.4	-2.7	-3.4	-3.3	-3.5	53.5	0.3	32.5	-16.3	36.0
27	-1.1	2.1	-2.7	-3.7	4.4	-3.6	52.5	0.1	16.9	-42.2	-7.9
28	2.7	3.0	-6.3	-2.4	3.5	-3.6	53.9	0.2	-9.2	-22.0	40.0
29	2.4	-2.2	-1.9	-3.4	3.6	-3.6	55.5	0.2	-38.2	-46.9	10.3
30	3.3	-3.0	-6.8	-2.3	-3.5	-3.5	59.4	0.4	3.6	-26.0	-7.8
31	2.6	-1.1	-3.9	0.0	-0.4	-3.9	57.8	0.3	-1.7	-31.0	-30.9

Run#	R_x	R_y	P_x	P_y	M_x	M_y	SH_A	μ	T_1	T_2	T_3
32	1.7	0.5	-3.5	-3.5	1.3	-3.7	51.5	0.2	36.3	-31.4	39.4
33	-2.7	2.0	-1.3	-0.6	-7.7	-3.3	56.7	0.3	3.3	-48.6	-0.2
34	3.1	-2.8	-4.1	-2.0	4.1	-3.8	51.7	0.1	-4.9	-31.6	13.6
35	-0.7	-0.5	-6.7	-3.0	-3.8	-3.9	56.8	0.3	39.2	-28.4	23.7
36	-3.9	-2.5	-6.9	-0.7	-4.2	-3.2	55.1	0.2	28.1	-34.7	4.4
37	-2.4	3.6	-4.3	-2.1	-6.2	-3.2	52.7	0.3	-33.1	-43.5	0.4
38	1.6	-3.7	-0.7	-0.8	-0.7	-3.3	50.8	0.2	-5.1	-46.8	4.7
39	0.3	-1.9	-5.3	-0.8	-3.9	-3.1	51.6	0.1	11.6	-42.6	-35.8
40	1.5	-2.9	-4.3	-1.3	2.8	-3.8	53.4	0.2	-14.5	-12.6	-36.2
41	3.4	-0.8	-0.6	-2.9	2.1	-3.8	50.6	0.3	-23.2	-25.9	-18.0
42	3.7	-0.6	-5.3	-1.7	-7.8	-4.0	54.4	0.2	13.1	-36.5	-18.8
43	0.0	-1.4	-3.9	-3.5	-6.4	-3.6	58.1	0.4	-11.1	-34.0	-39.5
44	0.8	1.0	-3.1	-4.0	-4.7	-3.1	52.5	0.3	38.2	-33.9	9.2
45	2.9	0.1	-4.6	-0.2	-1.9	-3.8	51.4	0.2	-22.7	-47.4	23.8
46	-1.7	0.5	-3.2	-1.4	-3.8	-3.1	50.4	0.2	37.4	-18.8	26.7
47	-0.6	-1.9	-6.1	-0.2	2.0	-3.8	52.3	0.2	33.8	-30.1	25.1
48	0.3	-1.5	-3.2	-0.7	-7.7	-3.5	59.5	0.1	12.4	-38.0	-29.1
49	-0.8	2.3	-6.7	-2.0	-7.3	-3.7	55.9	0.4	-11.0	-38.0	21.2
50	-1.9	-2.3	-5.5	-0.4	-3.9	-3.8	58.6	0.2	27.3	-17.0	5.2
51	-1.8	1.5	-5.9	-0.8	-1.3	-3.3	58.1	0.1	3.1	-49.2	-14.7
52	3.3	-0.8	-2.5	-1.5	0.1	-4.0	51.5	0.3	34.9	-25.2	-0.4
53	3.3	-3.9	-6.8	-1.7	2.1	-3.8	54.1	0.3	17.2	-41.5	-15.0
54	-2.2	-1.9	-0.8	-1.7	2.3	-3.0	51.7	0.3	10.5	-35.1	34.2
55	-2.2	-4.0	-2.5	-1.0	0.2	-3.2	56.8	0.2	-12.8	-48.7	-28.0
56	-3.2	-0.9	-4.6	-1.8	4.2	-3.0	58.9	0.3	15.8	-44.3	5.1
57	-2.1	-2.8	-2.9	-0.2	-1.2	-3.4	56.1	0.3	33.9	-46.6	28.6
58	3.1	-0.5	-5.7	-1.6	2.3	-3.6	59.0	0.2	26.9	-25.9	-39.2
59	-3.3	-0.4	-6.0	-2.6	-5.4	-3.2	51.8	0.3	3.9	-37.7	37.6
60	-1.1	-3.9	-4.9	-1.7	-4.4	-3.8	55.9	0.2	38.4	-45.3	-7.0
61	-2.0	-3.7	-3.1	-3.5	-7.4	-3.6	57.2	0.1	-13.9	-36.0	-11.6
62	2.6	-1.1	-4.3	-0.9	-7.8	-3.7	54.8	0.4	-2.0	-13.7	4.1
63	0.9	-0.2	-4.2	-3.0	4.8	-3.4	50.1	0.2	26.2	-14.1	-10.8
64	-1.6	0.6	-0.1	-2.1	0.4	-3.2	53.1	0.3	35.5	-15.1	-6.7
65	1.2	-2.6	-5.9	-3.9	-1.1	-3.9	50.8	0.3	5.4	-24.6	-20.1
66	-0.9	2.5	-3.0	-1.1	4.9	-3.7	59.0	0.3	-15.6	-20.8	35.4
67	3.6	-0.9	-2.7	-3.2	-4.8	-4.0	51.9	0.2	-24.0	-37.9	23.3
68	-1.0	0.4	-5.5	-3.3	-0.7	-3.2	50.0	0.3	-23.7	-33.2	-33.4
69	3.2	3.7	-4.4	-2.4	1.7	-3.1	53.0	0.3	-33.3	-24.8	-1.4
70	1.4	-0.9	-3.1	-1.3	-2.8	-3.6	57.5	0.4	-29.7	-49.2	39.8
71	3.2	-0.6	-5.0	-0.7	3.5	-3.1	58.3	0.3	24.3	-21.3	2.2
72	-1.1	3.1	-2.2	-3.4	-0.4	-3.6	50.4	0.3	17.1	-26.9	-36.6

Run#	R_x	R_y	P_x	P_y	M_x	M_y	SH_A	μ	T_1	T_2	T_3
73	-3.5	2.0	-0.1	-2.5	-1.3	-4.0	54.1	0.2	-10.0	-25.6	-21.2
74	-2.3	1.6	-4.0	-3.3	-2.8	-3.7	50.4	0.1	-28.0	-34.2	9.4
75	4.0	1.6	-2.4	-1.0	-1.2	-3.7	51.0	0.2	-19.3	-13.6	23.5
76	3.6	2.0	-2.1	-2.5	1.7	-3.3	50.8	0.2	-11.9	-44.4	19.2
77	-3.8	-0.7	-1.7	-3.3	-4.1	-3.1	52.0	0.4	-10.2	-27.9	1.5
78	2.7	3.1	-3.0	-1.5	3.8	-3.7	52.0	0.1	-3.3	-35.5	-38.7
79	-1.0	-3.0	-4.4	-3.9	3.1	-3.3	50.2	0.3	3.8	-35.8	17.2
80	0.0	-1.0	-2.5	-2.2	2.2	-3.6	50.1	0.3	-39.7	-29.8	37.1
81	-3.2	-2.9	-4.2	-3.3	-0.2	-3.8	54.9	0.4	-30.1	-39.0	29.9
82	1.8	-1.1	-1.2	-0.1	-2.2	-3.6	50.9	0.4	-8.4	-32.3	17.9
83	3.5	1.1	-2.9	-3.5	0.9	-3.9	54.5	0.1	16.4	-18.9	-13.7
84	-3.3	0.2	-1.8	-2.0	-1.7	-3.7	56.3	0.4	6.8	-17.0	-38.9
85	-0.3	-3.8	-1.7	-0.4	-1.4	-3.6	57.5	0.4	14.4	-16.5	24.5
86	-0.7	-3.5	-5.5	-0.6	-4.5	-3.3	56.3	0.1	-30.1	-19.4	5.7
87	-0.9	2.2	-3.7	-1.6	4.9	-4.0	51.3	0.2	1.0	-20.4	7.6
88	-2.1	2.6	-4.2	-0.1	-3.3	-3.4	59.1	0.3	-28.8	-34.5	32.3
89	-0.4	-3.9	-1.0	-3.4	-2.5	-3.4	51.9	0.3	-33.9	-39.4	-23.2
90	0.7	2.8	-3.5	-0.6	1.8	-3.5	52.6	0.2	29.9	-47.8	36.2
91	2.8	-3.0	-5.7	-0.1	-5.6	-3.4	55.4	0.2	15.5	-19.5	-29.3
92	-0.3	0.2	-2.9	0.0	4.8	-3.1	53.5	0.1	6.3	-36.4	-1.2
93	0.2	-0.3	-5.3	-1.3	-4.0	-3.1	59.5	0.3	11.9	-44.1	-36.0
94	-3.9	3.7	-1.8	-3.5	-3.7	-3.5	57.4	0.3	5.9	-37.6	-13.2
95	-3.9	-0.1	-2.9	-3.8	-4.6	-3.5	55.2	0.2	-39.0	-21.5	-30.2
96	2.1	-3.2	-0.1	-3.6	0.6	-3.4	52.2	0.1	-1.2	-27.4	21.6
97	2.3	-1.3	-1.2	-3.1	-5.2	-3.1	57.8	0.3	22.0	-14.3	15.2
98	1.3	3.2	-1.4	-3.4	1.6	-3.9	55.4	0.2	-35.2	-25.3	20.3
99	-3.4	-1.7	-3.3	-1.2	-0.3	-3.6	51.3	0.1	11.5	-44.7	30.9
100	3.6	0.3	-5.7	-0.1	3.5	-3.5	50.9	0.3	-0.4	-27.8	-8.6
101	0.9	1.1	-2.4	-3.7	1.0	-3.3	59.8	0.4	25.3	-32.2	-14.8
102	-1.3	-2.0	-5.9	-0.1	3.2	-3.4	56.2	0.3	30.2	-39.5	-30.5
103	0.6	-3.2	-1.4	-0.4	4.0	-3.3	54.3	0.4	7.6	-24.3	-26.1
104	2.8	-0.2	-0.3	-2.4	-4.8	-3.4	53.7	0.4	29.3	-27.7	-36.5
105	1.5	-2.5	-3.1	-3.5	3.1	-3.5	59.9	0.1	0.1	-32.6	-10.7
106	-3.2	3.0	-3.5	-3.6	1.6	-3.3	50.8	0.3	-2.3	-19.7	24.0
107	0.6	0.6	-0.5	-1.4	4.7	-3.5	50.2	0.3	24.9	-40.6	-8.9
108	2.8	-2.8	-2.8	-0.1	1.4	-3.2	59.1	0.2	-15.5	-28.9	-18.4
109	0.8	0.7	-3.5	0.0	4.4	-3.6	59.3	0.3	-0.9	-48.8	10.2
110	-3.3	2.5	-5.2	-1.1	1.5	-3.5	51.8	0.1	38.1	-33.3	-9.1
111	-0.3	-1.6	-0.6	-4.0	-3.1	-3.5	56.8	0.1	40.0	-28.1	-7.6
112	2.4	-2.6	-2.3	-1.1	-3.6	-3.4	57.6	0.3	-35.7	-18.5	-30.1
113	1.6	-3.3	-4.9	-3.3	3.3	-4.0	58.5	0.3	-16.1	-24.6	-16.8

Run#	R_x	R_y	P_x	P_y	M_x	M_y	SH_A	μ	T_1	T_2	T_3
114	2.7	3.1	-6.1	-1.3	-6.3	-3.7	59.5	0.3	-17.7	-28.3	-23.7
115	-2.3	1.1	-0.6	-3.6	0.9	-3.1	58.0	0.3	10.3	-29.1	35.2
116	-2.5	0.4	-4.5	-1.5	-6.9	-3.4	50.6	0.3	-36.8	-16.0	7.1
117	2.5	-2.2	-3.1	-1.3	0.3	-3.1	50.6	0.1	-18.0	-19.9	-10.5
118	-0.2	-0.4	-3.0	-1.6	4.5	-3.5	54.9	0.4	39.0	-26.7	36.5
119	0.1	-0.3	-3.7	-0.1	3.0	-3.2	54.4	0.3	-39.4	-14.9	13.2
120	-3.2	1.4	-4.2	-1.1	-6.9	-3.2	58.3	0.2	-11.5	-13.8	-16.1
121	1.1	3.7	-2.4	-3.2	5.0	-3.5	57.3	0.3	-5.9	-47.1	16.1
122	1.4	1.4	-4.7	-3.6	-2.7	-3.3	56.6	0.1	25.4	-15.0	27.2
123	1.3	-3.1	-6.2	-2.2	-1.6	-3.2	51.3	0.2	37.3	-40.1	24.6
124	0.6	-3.6	-1.6	-0.5	-7.6	-3.6	56.2	0.4	11.8	-38.5	-20.1
125	4.0	-0.2	0.0	-1.6	-3.4	-3.3	54.6	0.3	-39.8	-32.0	14.7
126	-1.9	2.7	-4.1	-3.9	0.3	-3.2	59.7	0.2	18.5	-37.1	-0.9
127	-3.0	2.2	-3.5	-1.0	-5.9	-3.9	52.7	0.2	-20.9	-41.9	37.3
128	3.9	-3.1	-5.4	-0.9	-4.4	-3.3	56.7	0.3	-8.9	-49.7	1.7
129	0.5	-2.7	-5.6	-1.8	-0.1	-3.7	55.2	0.4	36.8	-14.0	-26.4
130	-0.2	-3.1	-0.4	-2.9	1.8	-3.9	54.6	0.3	19.5	-12.5	-15.6
131	0.6	-1.2	-2.0	-3.9	-0.1	-3.9	59.0	0.3	8.7	-42.8	18.8
132	-1.6	-2.2	-5.6	-2.0	-3.9	-3.9	59.2	0.3	-26.4	-17.6	15.8
133	0.8	0.8	-4.0	-0.6	-5.6	-3.8	59.4	0.3	28.6	-44.9	10.8
134	1.8	-2.6	-4.8	-3.7	-5.9	-3.1	55.0	0.3	-27.8	-15.2	-3.5
135	-1.4	-2.4	-2.5	-0.2	-3.5	-3.8	58.6	0.2	-24.5	-45.6	12.4
136	1.8	-0.4	-5.4	-0.3	3.9	-3.7	57.1	0.1	1.2	-14.4	14.8
137	-2.4	-3.7	-4.5	-1.6	0.1	-3.8	58.8	0.4	13.7	-38.3	-9.4
138	-1.3	-3.7	-0.3	-0.4	-0.4	-3.5	56.6	0.1	23.7	-29.1	2.3
139	0.2	-2.8	-2.8	-2.5	-0.4	-3.1	57.9	0.2	37.1	-30.3	39.7
140	-3.8	1.5	-0.8	-1.4	3.5	-3.5	56.7	0.2	30.9	-43.7	8.7
141	-3.7	-1.7	-5.0	-2.6	-7.1	-3.9	53.2	0.2	14.7	-27.5	22.2
142	-0.3	-2.4	-6.4	-2.2	-7.7	-3.3	54.5	0.2	19.0	-13.1	22.5
143	-2.8	-3.2	-1.1	-2.3	-7.7	-3.6	56.0	0.3	-7.5	-13.1	0.1
144	3.5	3.2	-4.7	-2.5	0.7	-4.0	54.7	0.2	6.5	-46.7	10.7
145	0.5	0.3	-4.7	-0.6	-2.8	-3.1	57.4	0.1	34.7	-20.0	-3.9
146	1.2	-0.3	-1.0	-1.9	-1.3	-3.2	50.3	0.3	-24.3	-13.8	-19.2
147	-0.4	-1.7	-1.2	-0.2	-0.8	-3.0	57.6	0.4	-12.6	-38.7	9.5
148	4.0	2.4	-4.3	-3.2	-0.6	-3.4	57.7	0.2	-3.9	-45.7	-36.8
149	2.1	2.0	-5.7	-1.5	3.3	-3.8	56.4	0.3	-36.5	-16.0	-15.3
150	2.5	2.5	-1.9	-0.7	2.9	-3.1	55.3	0.3	-7.1	-31.9	39.5
151	1.9	-3.8	-0.3	-2.3	3.7	-3.7	55.1	0.2	9.5	-41.1	-31.8
152	-4.0	3.3	-4.3	-2.8	0.1	-3.8	57.5	0.1	8.9	-21.9	25.6
153	0.4	0.7	-1.6	-4.0	-2.2	-3.0	53.1	0.2	-40.0	-26.9	14.5
154	-2.9	-1.0	-5.4	-1.1	3.8	-3.3	58.8	0.2	-39.5	-33.6	-3.6

Run#	R_x	R_y	P_x	P_y	M_x	M_y	SH_A	μ	T_1	T_2	T_3
155	-2.1	-1.5	-0.3	-3.0	-2.8	-3.9	54.9	0.2	-27.2	-42.3	29.3
156	2.0	3.5	-0.2	-3.0	-0.7	-3.7	55.4	0.2	34.4	-41.5	-17.9
157	-1.9	3.0	-2.0	-0.7	-6.7	-3.8	51.4	0.2	5.7	-14.8	7.3
158	2.5	1.8	-3.8	-0.5	-2.9	-3.9	51.0	0.1	31.2	-29.7	7.5
159	-4.0	-0.2	-3.5	-2.1	-6.6	-3.9	57.1	0.3	-23.5	-44.6	-15.2
160	-2.7	-1.7	-2.0	-2.5	3.2	-3.1	52.8	0.2	31.5	-36.1	-32.0
161	2.1	1.9	-3.2	-3.4	-2.9	-3.2	58.3	0.2	33.0	-17.9	-36.3
162	-1.4	4.0	-1.1	-0.8	1.3	-3.3	59.0	0.4	23.0	-31.6	8.4
163	2.1	3.5	-6.9	-1.6	-0.5	-3.4	57.4	0.3	-23.8	-47.6	17.4
164	-2.3	-3.5	-5.5	-1.4	4.8	-3.4	50.5	0.2	-9.5	-30.0	-11.1
165	3.4	1.2	-2.1	-2.6	4.3	-3.5	55.9	0.4	7.0	-15.0	-28.5
166	2.6	-1.5	-3.4	-2.6	-7.8	-3.6	59.7	0.2	-37.1	-32.0	5.9
167	-1.4	1.7	-3.4	-2.1	-2.9	-3.4	54.7	0.1	-35.0	-12.0	32.5
168	-1.7	0.5	-5.2	-0.9	-6.7	-3.6	50.7	0.3	31.0	-48.9	3.5
169	-3.6	-2.8	-5.7	-2.9	4.4	-3.8	54.2	0.3	19.6	-21.7	13.7
170	-1.3	3.3	-2.0	-3.4	4.1	-3.8	55.6	0.3	37.0	-22.1	6.3
171	0.9	2.8	-2.0	-3.1	-6.6	-3.9	54.0	0.4	28.9	-27.5	16.0
172	-3.0	-2.2	-3.9	-2.3	4.2	-3.6	54.7	0.3	-32.5	-31.0	-37.0
173	2.4	-3.0	-3.4	-1.2	2.6	-3.9	59.0	0.2	35.4	-32.4	18.4
174	2.7	2.1	-6.5	-3.9	3.0	-3.2	55.7	0.3	29.1	-28.7	-2.0
175	-1.4	3.1	-7.0	-3.2	-1.6	-3.3	53.3	0.1	13.2	-44.8	20.8
176	0.5	-2.5	-2.6	-1.2	-8.0	-3.0	53.8	0.2	-32.8	-36.3	-14.2
177	-1.4	1.7	-6.2	-1.2	4.6	-3.4	53.0	0.3	-18.2	-47.9	-24.1
178	1.7	2.8	-2.8	-0.3	-5.1	-3.4	50.9	0.2	-31.8	-27.2	-25.6
179	-0.2	2.6	-2.9	-2.2	-6.7	-3.8	51.1	0.1	10.0	-36.9	-37.4
180	-0.5	0.4	-2.9	-3.9	-6.7	-3.2	51.9	0.2	-0.6	-46.3	-13.6
181	-1.5	-3.5	-3.8	0.0	-5.4	-3.5	50.3	0.2	7.5	-23.3	1.4
182	1.0	-0.1	-1.2	-0.5	-2.3	-3.4	59.6	0.3	27.2	-16.2	-29.6
183	-2.6	-1.6	-6.6	-2.9	1.7	-3.1	54.0	0.3	-32.0	-18.2	9.7
184	3.8	1.0	-6.4	-1.5	-2.1	-3.6	55.2	0.2	38.7	-15.4	13.9
185	-2.4	2.0	-5.1	-2.9	-7.2	-3.6	57.3	0.1	36.2	-31.5	-15.8
186	1.5	1.5	-6.5	-2.8	-0.3	-3.7	50.4	0.2	35.8	-42.5	-22.0
187	-0.8	-2.7	-6.0	-3.1	0.3	-3.0	56.7	0.4	26.5	-24.0	13.1
188	-2.2	3.2	-1.9	-2.7	1.2	-3.6	52.5	0.4	-38.4	-33.2	-4.3
189	1.5	-3.4	-3.5	-0.7	2.4	-3.5	51.1	0.2	39.5	-28.0	-25.9
190	-2.5	0.1	-6.6	-0.8	3.6	-4.0	58.1	0.2	-6.7	-26.4	-17.1
191	-1.7	2.7	-4.0	-3.6	-5.1	-3.7	59.2	0.2	-21.1	-36.7	38.2
192	0.5	2.0	-0.4	-1.5	3.2	-3.3	58.7	0.3	-36.6	-27.2	-13.9
193	3.6	-3.8	-1.7	-2.1	-2.4	-3.9	55.8	0.4	-16.9	-33.9	3.1
194	0.5	3.4	-5.3	-0.8	-3.6	-3.7	56.1	0.2	14.0	-16.3	-31.5
195	-1.2	-2.1	-6.3	-0.9	2.8	-3.4	58.1	0.4	-11.3	-30.8	34.4

Run#	R_x	R_y	P_x	P_y	M_x	M_y	SH_A	μ	T_1	T_2	T_3
196	-2.9	0.6	-2.4	-3.8	-7.9	-3.2	55.9	0.2	8.4	-25.4	26.2
197	1.9	0.5	-4.5	-2.8	-3.3	-4.0	55.7	0.2	-38.1	-26.6	-38.1
198	-0.7	-0.2	-0.9	-0.2	-0.6	-3.9	51.5	0.1	-23.3	-30.4	8.3
199	-3.9	0.6	-3.1	-0.5	4.8	-3.6	53.0	0.3	-9.4	-37.7	21.1
200	3.0	2.7	-1.0	-3.4	2.2	-3.2	58.7	0.2	-6.3	-22.6	13.4
201	2.9	-0.7	-5.9	-1.5	4.0	-3.7	57.5	0.1	-27.5	-43.5	-19.8
202	-1.6	1.8	-5.7	-0.7	2.3	-3.5	59.3	0.2	37.8	-29.4	28.3
203	-2.0	-1.9	-2.4	-2.1	-4.4	-3.1	58.2	0.3	-36.3	-19.6	33.8
204	3.0	2.8	-1.8	-0.4	0.5	-3.1	53.2	0.3	17.9	-23.1	-22.7
205	-2.2	-2.7	-5.1	-1.0	0.8	-3.3	59.2	0.3	-9.1	-12.3	-20.0
206	-3.4	-1.0	-5.1	-3.5	-5.1	-3.4	57.3	0.3	31.7	-47.7	-0.1
207	3.9	0.0	-0.2	-1.2	0.1	-3.5	57.5	0.4	24.0	-40.9	7.9
208	-3.5	0.1	-2.3	-0.8	-5.8	-3.4	53.9	0.1	-25.4	-39.9	-25.1
209	2.9	3.4	-2.2	-3.2	-4.1	-3.7	57.6	0.4	-22.9	-41.2	-1.7
210	-0.1	2.4	-3.2	-1.4	-3.1	-3.9	54.2	0.4	-29.4	-18.4	38.7
211	3.9	2.3	-2.8	-1.0	-1.8	-3.4	59.2	0.3	-15.0	-12.2	12.8
212	3.7	-1.8	-0.2	-0.1	-2.4	-3.7	53.0	0.2	1.5	-22.8	-24.6
213	1.4	0.8	-2.1	-0.6	-7.3	-4.0	54.3	0.3	-38.9	-37.4	-2.8
214	2.9	-0.7	-5.6	-4.0	-3.1	-3.3	50.1	0.2	-6.2	-26.1	6.7
215	-1.5	-0.6	-1.2	-3.6	-6.4	-3.3	57.2	0.3	-27.3	-48.0	11.1
216	-2.2	0.8	-3.9	-2.4	2.1	-3.1	55.0	0.3	-34.6	-44.1	34.6
217	-0.7	2.8	-6.9	-1.6	-7.2	-3.1	58.8	0.2	15.2	-33.7	10.0
218	1.1	1.2	-0.8	-0.4	-2.7	-3.3	59.1	0.2	19.2	-43.1	28.8
219	0.4	2.6	-1.6	-3.9	-5.8	-3.7	58.8	0.1	-10.7	-22.9	-14.0
220	0.1	-1.0	-3.3	-3.0	-3.2	-3.9	53.1	0.4	-37.6	-16.6	-17.6
221	-1.7	0.8	-2.3	-3.4	2.6	-3.1	56.4	0.3	-20.6	-46.0	-35.4
222	-1.5	-0.3	-3.6	-3.8	5.0	-3.4	56.4	0.2	-18.7	-28.5	37.0
223	-3.7	0.9	-2.7	-0.2	-0.3	-3.5	59.9	0.3	-7.9	-35.3	-32.3
224	-0.4	-0.2	-4.8	0.0	-3.6	-3.0	53.3	0.2	-7.8	-47.3	26.1
225	0.8	0.8	-6.4	-3.2	-5.2	-3.8	60.0	0.2	4.1	-46.5	-6.5
226	3.6	1.5	-1.3	-0.8	-3.2	-3.8	51.9	0.3	6.7	-48.2	-28.8
227	-0.1	3.4	-4.2	-0.5	-1.6	-3.9	56.5	0.2	-28.6	-45.1	-30.4
228	-2.0	-3.2	-1.8	-2.7	3.7	-3.4	54.5	0.4	-16.6	-13.9	19.0
229	2.3	-2.6	-2.1	-1.2	-4.2	-3.7	54.0	0.2	-32.6	-45.4	-35.5
230	-1.2	-0.1	-3.3	-3.1	-1.5	-3.7	58.7	0.1	22.5	-47.6	32.1
231	-1.8	1.6	-5.8	-2.5	4.9	-3.2	56.5	0.1	10.8	-13.2	-7.1
232	-1.9	0.0	-1.2	-0.9	2.8	-3.1	59.9	0.2	-1.8	-17.3	11.5
233	-2.4	-3.1	-5.0	-3.5	1.4	-3.1	54.4	0.1	1.4	-43.9	9.9
234	3.5	1.9	-2.2	-1.1	4.1	-3.8	54.3	0.3	-29.1	-38.6	12.9
235	0.3	-0.5	-6.5	-1.0	-4.2	-4.0	52.3	0.2	-14.8	-14.2	15.3
236	0.0	0.0	-3.5	-3.8	-7.9	-3.6	53.2	0.3	18.4	-13.0	-25.7

Run#	R_x	R_y	P_x	P_y	M_x	M_y	SH_A	μ	T_1	T_2	T_3
237	-2.2	4.0	-0.9	-1.3	-3.5	-3.3	58.3	0.1	13.9	-31.2	-18.7
238	3.5	3.8	-4.8	-3.7	-7.3	-3.5	54.4	0.2	20.0	-35.2	-4.6
239	1.3	-0.9	-1.0	-2.5	-6.8	-3.7	52.2	0.1	-23.0	-16.7	-10.3
240	1.9	-2.2	-0.5	-0.9	3.8	-3.8	57.0	0.2	-29.3	-19.2	8.6
241	2.4	-3.7	-6.7	-2.6	1.7	-3.2	55.3	0.2	13.4	-17.7	-6.8
242	-1.6	-1.8	-5.9	-0.5	1.1	-3.8	51.6	0.4	-14.7	-18.0	-0.6
243	2.7	-3.9	-0.9	-2.2	-4.5	-3.6	58.2	0.2	7.8	-45.4	18.2
244	-1.0	-4.0	-0.1	-2.8	-1.7	-3.3	55.8	0.4	24.8	-36.4	6.8
245	-0.4	-1.5	-6.8	-2.9	0.4	-3.9	51.2	0.2	-4.3	-46.3	27.7
246	2.5	-0.1	-2.7	-3.8	1.0	-3.6	52.1	0.4	2.3	-49.4	-22.9
247	-0.3	-0.7	-0.4	-1.7	-1.1	-3.7	56.6	0.4	-26.2	-49.5	-27.3
248	2.6	0.6	-3.6	-2.0	-8.0	-3.0	51.9	0.2	18.2	-20.9	-20.8
249	-3.8	-1.2	-6.0	-2.7	-5.0	-3.0	56.2	0.2	-12.4	-37.1	-28.6
250	3.8	3.9	-3.6	-2.3	1.0	-3.5	52.1	0.4	28.5	-34.6	11.8
251	-3.1	-1.3	-4.2	-3.8	-2.3	-4.0	58.3	0.2	16.0	-23.4	-22.4
252	2.6	-3.4	-5.4	-3.8	-4.6	-3.8	56.9	0.2	16.1	-29.5	23.0
253	0.2	4.0	-4.4	-2.4	-0.6	-3.1	56.7	0.3	21.1	-13.4	24.1
254	1.2	-1.3	-6.7	-0.4	-4.0	-3.3	54.2	0.4	30.5	-34.1	14.0
255	-1.3	1.0	-7.0	-3.6	-7.9	-3.7	52.9	0.2	-15.2	-35.9	-19.5
256	-2.0	-2.3	-2.7	-3.1	-4.5	-3.9	52.6	0.4	39.4	-35.6	-17.4
257	-0.6	0.0	-0.4	-1.3	4.5	-4.0	57.7	0.4	12.3	-31.3	-6.2
258	-2.1	3.9	-1.0	-3.0	-1.6	-3.3	54.3	0.2	-7.0	-45.9	30.2
259	3.5	1.2	-2.8	-3.2	-7.8	-3.4	51.6	0.3	-26.9	-33.5	-21.7
260	2.3	-0.7	0.0	-2.3	-3.4	-3.1	55.9	0.1	-5.4	-36.7	-23.0
261	-4.0	-0.6	-4.7	-2.1	-1.5	-3.8	50.9	0.2	9.9	-12.7	-24.9
262	-2.7	-3.5	-3.8	-3.6	-0.2	-3.3	59.9	0.3	-22.4	-32.6	-5.4
263	-2.5	0.0	-1.4	-1.6	1.0	-3.4	56.6	0.4	36.6	-46.1	-30.7
264	-2.8	-0.6	-0.5	-1.9	-1.0	-3.9	50.0	0.4	-1.0	-20.5	6.5
265	-3.8	-2.5	-4.7	-2.9	-2.6	-3.6	50.8	0.2	7.3	-45.1	-29.7
266	3.2	2.6	-5.6	-0.3	-2.6	-3.4	55.6	0.2	33.3	-43.3	-16.9
267	-2.5	2.5	-0.9	-2.3	-5.3	-3.6	58.0	0.2	32.3	-12.8	2.0
268	-1.2	2.9	-3.8	-2.5	-6.0	-3.3	59.7	0.2	-31.5	-39.7	-33.8
269	2.9	1.3	-4.5	-3.9	-2.6	-3.4	57.1	0.1	-24.8	-40.4	22.7
270	3.9	0.6	-0.7	-2.1	-0.5	-3.9	59.7	0.2	-14.0	-37.3	-16.6
271	1.7	-3.0	-2.0	-1.9	-5.3	-3.7	53.4	0.2	35.2	-15.6	26.9
272	0.4	-3.4	-1.6	-2.5	4.9	-3.0	55.5	0.2	-27.0	-29.0	-8.3
273	2.8	-1.9	-4.9	-2.6	4.6	-3.2	52.4	0.2	9.7	-45.5	-22.5
274	0.2	2.7	-5.0	-1.5	-7.4	-3.7	58.5	0.2	4.9	-14.6	33.4
275	-2.6	0.4	-5.2	-3.8	0.5	-3.6	57.0	0.2	-34.4	-49.6	-5.1
276	-1.3	-3.8	-4.1	-2.5	-6.3	-3.3	58.7	0.3	36.0	-24.0	-23.5
277	0.1	0.9	-1.1	-1.5	-7.0	-3.3	50.2	0.2	-19.0	-33.8	31.7

Run#	R_x	R_y	P_x	P_y	M_x	M_y	SH_A	μ	T_1	T_2	T_3
278	1.4	-1.6	0.0	-4.0	-0.9	-3.5	58.0	0.3	-26.5	-21.2	-9.2
279	-1.5	-3.1	-2.2	-3.8	-5.0	-3.5	52.3	0.2	22.9	-45.7	30.5
280	3.6	1.2	-5.9	-1.2	-5.8	-3.2	57.2	0.1	-20.8	-31.1	-16.3
281	2.1	-1.5	-6.0	-3.1	-4.4	-3.1	57.8	0.1	27.5	-41.9	-10.2
282	-1.4	-0.8	-6.7	-2.3	1.2	-3.5	51.2	0.1	7.9	-18.9	35.8
283	0.7	3.3	-2.1	-3.3	-4.7	-3.2	56.6	0.3	-17.9	-15.9	-27.8
284	-2.7	3.9	-4.4	-2.4	-5.7	-4.0	56.5	0.3	-16.4	-17.8	-14.4
285	-1.8	2.2	-6.4	-0.9	-7.4	-3.4	52.0	0.1	-0.1	-28.4	0.7
286	1.3	1.7	-1.5	-1.5	4.5	-3.2	58.9	0.2	20.3	-38.2	-33.0
287	0.4	3.3	-3.8	-3.1	-0.8	-3.6	50.5	0.2	-30.4	-12.4	-21.1
288	-1.5	2.9	-2.5	-0.5	-3.1	-3.1	50.4	0.4	16.8	-35.7	16.4
289	-3.6	-3.2	-1.1	-1.1	-5.4	-3.4	52.9	0.3	-20.1	-42.1	24.9
290	1.9	0.2	-6.6	-0.9	-5.5	-3.7	57.1	0.1	17.4	-39.6	31.0
291	3.7	-2.7	-5.5	-1.3	-4.8	-3.6	50.7	0.3	-35.5	-25.8	-6.3
292	-3.1	-3.4	-3.3	-2.4	3.7	-3.9	56.9	0.1	-1.5	-41.4	-3.1
293	-2.0	0.7	-0.2	-1.6	-7.6	-3.6	51.8	0.3	-16.3	-30.7	-34.6
294	-3.9	3.0	-4.9	-0.8	-3.0	-3.8	50.5	0.3	-13.6	-35.4	-24.3
295	-2.6	0.2	-1.3	-1.1	-0.1	-4.0	55.2	0.2	27.0	-24.9	38.9
296	0.0	2.9	-4.1	-2.7	2.9	-3.0	55.3	0.1	-28.3	-36.1	-16.0
297	-2.3	-2.7	-0.7	-1.8	3.7	-3.5	59.1	0.3	-13.4	-40.7	29.6
298	0.3	2.3	-1.5	-2.9	-6.2	-3.9	54.4	0.1	15.6	-28.8	33.3
299	-3.2	1.9	-5.4	-2.2	-0.5	-3.3	58.8	0.3	35.7	-21.8	-30.1
300	-3.4	3.8	-3.9	-2.8	0.7	-3.2	58.8	0.3	-33.4	-21.4	8.1
301	-0.1	-0.1	-6.9	-2.8	2.7	-3.9	56.3	0.1	32.8	-31.3	3.3
302	-0.9	-1.6	-3.0	-3.9	-0.8	-3.9	52.6	0.2	-11.6	-12.8	25.7
303	-1.2	-0.6	-3.4	-2.7	-6.5	-3.7	50.0	0.4	-17.6	-46.4	3.9
304	-3.7	-3.6	-6.4	-2.9	-5.2	-3.6	53.5	0.4	-5.7	-23.3	-9.7
305	0.9	-0.9	-6.5	-2.9	-6.0	-3.6	59.2	0.2	-3.8	-13.4	-20.3
306	2.8	0.5	-0.3	-2.7	0.7	-3.8	55.5	0.3	8.1	-14.7	35.7
307	1.5	3.9	-5.8	-2.8	1.5	-3.7	59.8	0.2	-12.1	-24.3	-4.9
308	3.0	3.2	-2.6	-0.5	0.9	-3.5	57.1	0.1	-30.7	-32.7	11.0
309	1.1	3.3	-4.6	-3.9	-2.3	-3.5	51.5	0.3	-18.5	-41.6	33.1
310	0.4	1.3	-7.0	-1.0	1.2	-3.5	53.1	0.1	-37.9	-21.7	-20.6
311	3.7	-3.3	-3.0	-3.8	2.6	-3.5	55.2	0.3	31.8	-28.8	4.3
312	-1.6	-3.1	-5.8	-2.2	-0.9	-3.2	53.9	0.4	-10.8	-49.8	-5.7
313	3.3	-1.5	-1.1	-1.8	3.4	-3.3	56.2	0.2	29.7	-15.8	-1.0
314	1.0	-3.3	-4.9	-1.9	-7.6	-3.6	51.8	0.1	-8.7	-42.4	11.3
315	1.4	-1.2	-5.1	-2.3	1.2	-4.0	58.6	0.2	-25.3	-35.8	37.9
316	0.0	0.9	-0.3	-1.7	-6.4	-3.6	59.6	0.4	-7.3	-27.8	20.9
317	2.3	-2.7	-3.6	-3.1	-4.1	-3.2	51.8	0.3	-26.1	-47.3	31.2
318	-2.3	-0.3	-3.1	-2.7	2.9	-3.8	58.6	0.2	-33.6	-12.9	-11.9

Run#	R_x	R_y	P_x	P_y	M_x	M_y	SH_A	μ	T_1	T_2	T_3
319	-0.2	-1.5	-6.2	-3.3	-6.4	-3.6	53.8	0.2	-37.4	-26.3	37.8
320	-2.1	0.9	-5.1	-3.6	-6.6	-3.4	59.3	0.4	2.8	-16.9	8.9
321	-3.7	-0.1	-0.5	-3.0	-1.0	-3.3	58.9	0.1	-27.7	-34.4	1.0
322	-0.1	-4.0	-6.1	-0.8	2.4	-3.4	57.7	0.1	6.0	-41.0	20.4
323	0.1	0.1	-4.9	-0.5	1.5	-3.9	52.7	0.4	16.3	-49.3	-4.7
324	-0.5	3.1	-6.6	-3.6	-4.7	-3.1	54.9	0.2	-20.0	-18.7	-2.7
325	-3.4	-0.5	-2.8	-1.1	-4.8	-3.0	58.0	0.3	28.8	-23.2	20.6
326	3.4	1.4	-5.3	-3.7	-4.3	-3.9	56.1	0.3	-12.3	-16.8	14.2
327	-1.1	0.5	-2.7	-2.2	2.9	-4.0	51.0	0.2	-24.9	-48.4	-12.6
328	-0.6	-1.4	-1.6	-1.7	-4.3	-3.1	50.7	0.3	14.8	-49.5	-26.2
329	0.7	-0.8	-0.5	-0.2	-4.9	-3.1	54.5	0.2	-2.8	-14.5	9.1
330	2.4	3.2	-5.5	-2.1	-2.1	-4.0	50.7	0.3	-15.8	-32.9	-16.4
331	-1.5	3.7	-5.1	-2.0	2.2	-3.8	58.5	0.3	28.3	-46.2	-18.2
332	0.6	-3.9	-4.1	-0.3	3.1	-3.7	54.2	0.3	-35.4	-40.6	0.2
333	-0.9	-2.3	-2.6	-3.3	-2.5	-3.0	57.3	0.1	-5.5	-12.5	-12.1
334	-2.3	-3.8	-2.9	-2.1	-3.7	-4.0	51.7	0.2	-34.1	-29.7	-12.9
335	-3.6	-0.2	-3.3	-0.6	-7.3	-3.8	54.1	0.4	17.6	-27.3	15.5
336	-1.7	1.4	-0.7	-2.3	-1.1	-3.6	54.0	0.4	11.0	-47.5	33.0
337	-0.4	2.3	-2.3	-3.6	3.4	-3.9	58.1	0.3	-16.8	-34.8	-35.0
338	-2.0	1.1	-5.2	-0.7	0.3	-3.1	51.1	0.2	3.0	-15.5	-26.9
339	-1.1	3.9	-4.6	-0.7	0.9	-3.3	50.1	0.2	-24.1	-30.4	25.4
340	3.0	-0.9	-6.6	-0.1	-2.3	-3.7	57.7	0.3	-34.2	-26.8	18.7
341	0.0	2.3	-0.1	-1.9	4.7	-3.3	52.1	0.2	-21.6	-20.1	3.0
342	-3.8	-0.4	-6.5	-1.4	-1.4	-3.8	57.8	0.3	5.2	-46.6	29.4
343	-3.4	-2.4	-4.3	-1.3	0.5	-3.3	50.6	0.4	33.6	-30.2	-5.5
344	1.2	0.3	-6.2	-1.9	0.0	-3.1	59.7	0.2	-17.4	-21.1	32.6
345	-1.0	3.5	-2.6	0.0	-4.9	-3.4	55.5	0.4	-17.2	-20.3	-11.5
346	-1.7	3.8	-1.4	-0.6	-1.7	-3.9	53.3	0.3	34.6	-34.2	-14.5
347	-1.8	2.2	-0.9	-3.7	-7.5	-3.7	52.7	0.3	-25.6	-24.7	18.5
348	1.2	3.6	-1.9	-1.9	-7.1	-3.1	57.9	0.2	-20.4	-27.1	19.6
349	2.5	-1.4	-6.5	-3.0	-2.5	-3.8	55.0	0.4	-37.0	-44.5	-6.0
350	-1.5	-1.8	-5.4	-2.3	-6.2	-3.2	58.4	0.2	-20.1	-45.8	31.5
351	-2.8	2.4	-5.3	-2.0	0.0	-3.8	50.3	0.4	25.9	-32.1	28.1
352	-1.2	-2.1	-6.6	-3.6	2.7	-3.4	57.2	0.2	14.5	-38.3	-37.3
353	-3.1	0.3	-2.5	-0.2	-5.7	-3.3	54.1	0.2	36.5	-29.3	-32.1
354	-0.5	-1.1	-6.2	-0.5	-1.0	-3.9	51.7	0.1	-0.7	-38.9	-27.2
355	-0.8	-2.4	-5.6	-2.5	-6.0	-3.3	51.4	0.2	-21.7	-18.2	-37.1
356	-0.9	-2.0	-2.3	-3.7	2.5	-3.5	52.2	0.1	-18.4	-24.9	-34.2
357	-3.0	-2.3	-4.6	-1.4	0.0	-3.5	56.9	0.1	10.7	-23.8	-37.9
358	1.9	0.3	0.0	-2.0	4.3	-3.8	55.6	0.2	9.4	-39.1	32.0
359	3.5	-2.7	-3.4	-1.4	-2.1	-3.2	51.0	0.3	30.7	-17.4	2.7

Run#	R_x	R_y	P_x	P_y	M_x	M_y	SH_A	μ	T_1	T_2	T_3
360	-3.6	2.9	-6.1	-0.4	-1.4	-3.3	55.8	0.4	12.1	-43.0	-1.8
361	-3.6	-1.0	-1.2	-2.8	2.5	-3.4	53.6	0.1	21.9	-17.3	16.3
362	2.3	-1.7	-2.2	-2.7	-5.4	-3.9	59.6	0.3	26.7	-19.1	-4.1
363	-2.5	0.0	-1.7	-2.9	-2.0	-3.6	57.6	0.2	13.6	-49.1	-39.0
364	-3.0	-1.6	-1.3	-0.4	-1.1	-3.8	56.9	0.4	-38.7	-25.5	3.6
365	3.4	1.3	-5.8	-1.9	-3.6	-3.0	50.5	0.3	3.5	-43.4	-0.7
366	1.0	-3.3	-1.8	-0.9	-6.2	-3.7	53.9	0.2	-30.9	-21.1	37.4
367	1.1	-1.3	-0.8	-3.7	2.0	-3.1	56.1	0.2	19.3	-49.9	5.4
368	3.0	-2.5	-3.9	-1.1	4.1	-3.2	52.9	0.3	8.3	-46.0	22.0
369	3.0	3.4	-5.6	-1.8	0.8	-3.2	51.7	0.1	15.0	-22.4	-2.3
370	1.0	-1.1	-0.1	-3.5	-7.0	-3.9	54.7	0.3	0.2	-40.8	-19.3
371	-3.3	3.6	-5.0	-2.4	-7.0	-3.3	52.4	0.3	21.4	-22.1	-8.7
372	3.3	0.9	-1.9	-0.3	-3.3	-4.0	57.6	0.2	-1.4	-29.9	35.5
373	3.8	-1.9	-3.6	-0.1	-1.3	-3.3	53.5	0.2	15.3	-29.4	34.7
374	-0.8	-1.6	-4.4	-1.3	-6.3	-3.0	53.8	0.4	6.2	-19.2	-28.1
375	2.2	0.0	-0.4	-3.3	3.4	-3.2	52.6	0.4	-9.9	-32.9	17.1
376	-3.8	-2.2	-6.1	-3.0	-1.9	-3.4	59.5	0.2	8.6	-22.2	22.4
377	3.2	3.3	-2.6	-0.4	4.0	-3.8	56.4	0.2	26.4	-25.6	-3.8
378	3.4	-2.6	-3.0	-2.6	-6.9	-3.1	55.6	0.1	-11.8	-23.7	27.5
379	0.7	1.3	-6.2	-0.9	0.2	-3.4	51.3	0.4	-31.7	-39.0	22.9
380	2.0	-0.4	-2.4	-0.6	1.1	-3.8	56.0	0.1	25.7	-48.3	-17.2
381	3.8	-2.3	-2.1	-3.2	-4.1	-3.1	57.0	0.4	-6.0	-40.6	-12.8
382	1.8	1.7	-2.0	-1.5	-0.5	-3.3	56.9	0.1	-25.1	-13.3	-38.6
383	1.7	-2.1	-1.4	-1.4	-7.5	-3.1	53.2	0.3	21.7	-38.8	31.3
384	0.2	3.6	-1.8	-0.9	0.5	-3.5	55.3	0.1	20.4	-17.6	34.1
385	-0.1	-1.9	-1.1	-2.7	-2.7	-3.7	59.8	0.2	-5.2	-18.1	33.6
386	0.7	0.7	-6.6	-3.1	-2.2	-3.4	50.9	0.4	5.5	-17.5	12.1
387	-2.9	-2.0	-1.5	-1.8	-5.5	-3.0	55.8	0.1	24.1	-45.3	4.9
388	1.3	3.7	-0.2	-2.5	-3.2	-3.0	54.1	0.3	-2.5	-42.8	-7.3
389	0.9	-0.8	-4.8	-3.2	3.2	-3.6	59.8	0.3	18.7	-12.1	23.2
390	1.8	0.7	-4.9	-1.7	-7.5	-3.7	50.1	0.3	12.9	-28.1	39.2
391	-0.2	-3.8	-4.0	-2.9	-7.2	-3.5	57.8	0.4	4.6	-34.3	35.0
392	-0.7	3.5	-6.8	-1.4	3.6	-3.6	53.1	0.3	20.9	-21.4	-25.4
393	-0.6	1.4	-0.5	-0.6	-5.9	-3.7	58.6	0.2	-29.6	-20.2	-2.2
394	-0.2	1.9	-0.8	-1.5	-0.1	-3.5	52.1	0.1	32.1	-17.1	-32.8
395	2.1	1.8	-6.0	-2.2	-3.2	-3.5	51.1	0.1	-28.9	-48.6	-22.2
396	3.3	3.7	-3.2	-0.6	-6.8	-3.4	54.5	0.3	-3.5	-42.7	25.3
397	1.6	1.9	-1.5	-0.3	-4.6	-3.5	54.6	0.3	39.7	-19.8	28.0
398	4.0	-1.4	-1.9	-2.7	-4.2	-3.5	51.2	0.2	35.0	-41.2	-8.1
399	-1.1	0.1	-0.7	-1.1	4.6	-3.6	56.8	0.1	-28.5	-39.8	-27.0

Run#	R_x	R_y	P_x	P_y	M_x	M_y	SH_A	μ	T_1	T_2	T_3
400	-0.3	2.7	-1.4	-1.6	-6.3	-3.9	59.3	0.3	14.2	-35.2	-38.2
401	1.6	3.8	-3.7	-1.2	1.5	-3.5	56.0	0.4	-4.4	-40.3	-35.7
402	2.2	-0.7	-3.7	-2.8	2.2	-3.0	52.6	0.2	-0.2	-14.7	38.1
403	1.9	-0.5	-5.0	-2.2	2.4	-3.2	52.9	0.4	33.1	-36.2	-34.9
404	-3.3	-1.8	-6.7	-1.1	-3.0	-3.5	52.3	0.2	-39.2	-42.0	6.0
405	-2.7	1.0	-6.3	-3.3	0.8	-3.8	53.7	0.4	0.7	-42.2	-23.3
406	-0.9	-3.2	-2.8	-3.7	0.6	-3.2	54.0	0.3	9.1	-19.0	-38.4
407	-3.5	-2.9	-4.0	-0.8	1.6	-3.8	55.3	0.2	-22.2	-20.7	32.8
408	-1.0	-2.1	-1.2	-2.7	-0.9	-4.0	50.3	0.1	23.8	-33.4	-4.4
409	-2.1	-1.1	-0.2	-2.2	-4.8	-3.1	58.4	0.3	-3.0	-29.6	-33.1
410	-1.9	-3.6	-4.6	-0.6	2.8	-3.1	54.8	0.2	21.6	-15.7	19.8
411	0.3	3.8	-6.5	0.0	-1.2	-3.9	54.8	0.3	2.0	-32.3	17.6
412	-2.9	2.1	-3.4	-0.2	-4.5	-3.9	56.5	0.1	22.2	-39.3	-1.5
413	0.2	2.4	-6.3	-4.0	-2.9	-3.1	56.8	0.4	-10.5	-41.3	-9.5
414	-2.7	-0.8	-2.5	-0.4	-7.5	-3.4	56.5	0.1	7.1	-26.2	36.6
415	-3.2	3.1	-5.7	-3.0	0.6	-3.6	54.7	0.2	-7.6	-30.5	-39.4
416	-2.8	2.7	-1.6	-2.6	-4.6	-3.1	51.6	0.1	-10.3	-20.1	-19.0
417	-2.6	1.7	-6.9	-1.7	-2.7	-3.4	56.3	0.4	-32.3	-25.1	-32.6
418	3.9	0.6	-6.3	-3.2	-5.6	-3.2	56.2	0.3	4.7	-30.0	36.3
419	0.8	0.4	-3.7	-3.6	4.3	-4.0	52.5	0.4	-3.1	-29.2	18.0
420	-0.1	-3.6	-5.8	-0.7	-6.1	-3.9	53.7	0.3	-8.1	-39.9	20.1
421	-2.8	-0.6	-5.8	-3.9	-2.2	-3.2	52.5	0.2	32.6	-23.0	-11.3
422	-1.9	1.8	-5.0	-1.8	1.8	-3.7	59.4	0.4	-34.7	-41.8	0.6
423	-3.9	1.6	-6.3	-0.8	-1.5	-3.4	54.8	0.3	2.2	-14.1	27.3
424	3.7	1.1	-6.7	-2.4	-2.6	-3.4	53.5	0.3	-3.6	-18.5	-39.7
425	-3.5	-2.4	-0.6	-1.0	0.4	-3.4	53.4	0.2	-22.5	-17.2	-21.6
426	3.6	-3.5	-2.3	-1.9	1.6	-3.3	58.9	0.3	-13.2	-27.0	31.8
427	-1.3	-0.4	-3.6	-2.2	4.2	-4.0	53.7	0.2	32.0	-33.1	-40.0
428	-1.8	3.5	-0.6	-1.6	-0.7	-3.9	58.9	0.2	-12.9	-43.2	14.4
429	-0.2	-4.0	-1.6	-1.8	2.3	-3.9	52.1	0.3	10.2	-41.7	27.8
430	-3.1	0.3	-2.7	-0.1	3.6	-3.6	55.1	0.3	30.4	-15.3	-11.8
431	2.2	3.0	-0.7	-3.3	-3.7	-3.4	51.4	0.2	16.6	-15.4	12.6
432	1.2	-2.4	-6.9	-0.7	0.8	-3.0	55.0	0.3	-21.2	-31.0	-26.5
433	-3.6	-1.2	-0.4	-3.8	3.3	-3.7	53.6	0.3	2.7	-38.4	-7.5
434	0.0	-2.1	-1.4	-1.2	0.6	-3.2	55.7	0.1	-31.0	-34.9	36.8
435	1.6	-3.3	-5.9	-3.1	-7.2	-3.3	52.4	0.3	17.7	-38.1	-21.9
436	1.1	1.3	-1.5	-3.0	-7.9	-3.2	59.5	0.2	27.8	-43.1	-5.9
437	1.9	2.8	-5.3	-3.4	-1.9	-3.9	57.0	0.3	30.1	-26.5	-32.5
438	-2.3	0.2	-6.8	-1.2	-6.0	-3.8	56.1	0.3	25.1	-32.8	-34.4
439	-1.8	1.4	-5.5	-4.0	2.7	-3.6	55.7	0.3	-6.5	-12.2	-18.5

Run#	R_x	R_y	P_x	P_y	M_x	M_y	SH_A	μ	T_1	T_2	T_3
440	-4.0	1.8	-4.3	-1.6	-0.2	-3.0	55.6	0.1	0.6	-30.9	28.9
441	-0.6	2.3	-4.8	-0.9	-0.9	-3.8	59.3	0.4	19.8	-16.4	2.5
442	1.3	1.8	-4.6	-0.5	-5.5	-3.6	50.2	0.3	28.0	-21.6	-26.7
443	2.3	-1.8	-4.0	-0.4	-7.0	-3.2	60.0	0.3	11.1	-26.5	24.3
444	0.9	2.6	-0.8	-0.4	-3.9	-3.2	51.5	0.1	20.8	-44.2	-9.9
445	-2.4	2.5	-3.5	-3.7	-3.4	-4.0	53.6	0.2	18.0	-47.0	5.5
446	2.6	-3.5	-5.6	-2.0	0.4	-3.8	53.6	0.3	-0.1	-19.8	39.0
447	-0.6	-3.4	-6.8	-1.5	-3.5	-3.7	58.4	0.2	-21.4	-40.2	-34.1
448	1.1	4.0	-0.4	-1.9	-2.0	-3.9	50.2	0.3	-4.7	-37.0	17.7
449	-0.8	-1.4	-4.5	-2.9	4.6	-3.6	55.1	0.3	39.8	-50.0	11.6
450	0.6	-2.3	-1.0	-0.6	3.9	-3.6	50.7	0.2	12.6	-16.1	25.9
451	1.0	-3.3	-3.7	-1.3	-1.8	-3.7	50.3	0.4	-2.2	-34.8	-39.8
452	1.0	1.5	-4.2	-2.0	-1.7	-3.1	57.9	0.4	24.5	-47.9	29.7
453	-0.6	3.8	-4.8	-2.3	-2.5	-3.0	53.8	0.2	23.5	-39.2	-37.8
454	2.0	-2.9	-5.3	-3.5	-2.1	-3.2	55.7	0.2	-37.8	-39.3	-25.3
455	3.1	-2.8	-5.1	-2.8	3.9	-3.4	52.4	0.4	-25.9	-23.9	-10.0
456	-2.9	2.1	-6.8	-2.6	1.3	-3.9	53.3	0.3	-36.0	-26.2	16.6
457	1.7	0.2	-5.2	-3.2	2.4	-3.1	59.6	0.3	-21.9	-20.5	-27.7
458	-3.7	2.4	-0.1	-1.2	-2.0	-3.3	54.3	0.3	-16.0	-22.3	30.4
459	-0.4	1.6	-1.5	-0.3	2.6	-3.8	52.4	0.3	-24.6	-23.6	-33.9
460	-2.8	2.4	-6.3	-3.4	2.7	-3.5	57.4	0.3	12.8	-33.6	30.7
461	3.8	1.7	-1.3	-1.3	-6.8	-3.5	57.2	0.1	24.6	-22.7	-2.5
462	2.7	3.2	-3.2	-2.8	-1.9	-3.7	59.9	0.3	33.4	-31.7	28.5
463	0.5	3.6	-5.8	-0.2	2.0	-3.2	58.4	0.2	-8.3	-25.7	-17.7
464	3.1	1.9	-1.3	-0.2	-5.2	-3.3	58.2	0.3	-14.4	-38.7	-29.4
465	2.2	2.1	-3.7	-2.1	-5.9	-3.1	53.9	0.1	27.7	-40.5	33.9
466	2.3	-2.3	-4.0	-2.0	4.5	-3.4	59.1	0.4	-13.1	-43.8	-24.0
467	2.8	-3.2	-3.8	-1.1	-3.8	-3.9	57.4	0.1	-8.6	-24.1	-3.0
468	-0.8	-1.7	-1.7	-1.0	-6.5	-4.0	54.6	0.2	29.4	-20.6	-31.7
469	-1.9	2.5	-4.7	-1.4	4.2	-3.7	55.4	0.1	-20.3	-44.4	24.8
470	3.2	2.7	-4.4	-1.7	-6.5	-3.2	57.3	0.4	29.6	-24.4	-12.4
471	3.4	-1.2	-4.4	-2.7	-4.0	-3.7	53.6	0.4	26.1	-48.2	27.0
472	-3.6	0.9	-1.3	-3.4	0.2	-3.9	58.2	0.3	-13.7	-19.3	19.5
473	-1.2	-3.6	-1.0	-1.7	-2.0	-3.8	59.6	0.2	-17.1	-27.6	-34.7
474	-1.1	-3.4	-7.0	-3.3	0.2	-3.8	55.0	0.1	-26.7	-25.0	-3.3
475	2.5	3.9	-5.4	-1.9	-6.5	-3.7	53.7	0.2	-36.2	-28.6	16.9
476	-3.5	1.6	-0.2	-2.6	-5.0	-3.5	51.0	0.2	31.3	-36.6	1.8
477	3.9	-3.6	-2.6	-3.1	-4.0	-3.5	55.8	0.2	2.5	-22.4	-37.6
478	3.7	1.1	-4.8	-1.9	3.9	-3.3	57.9	0.1	20.6	-40.9	21.4
479	3.1	-0.3	-2.2	-1.2	2.1	-3.2	52.3	0.3	-31.3	-43.6	-31.0

Run#	R_x	R_y	P_x	P_y	M_x	M_y	SH_A	μ	T_1	T_2	T_3
480	0.8	0.4	-6.0	-0.3	-6.9	-3.5	53.2	0.3	-19.8	-44.0	-28.9
481	1.7	-2.6	-6.4	-3.7	1.9	-3.3	58.0	0.3	-4.6	-44.7	26.5
482	-0.7	1.1	-1.7	-1.7	1.8	-3.9	59.8	0.1	23.3	-22.5	-13.4
483	3.8	-1.3	-4.1	-3.0	1.1	-3.5	56.0	0.2	-38.6	-14.4	7.8
484	-1.0	-3.6	-0.6	-2.4	-5.6	-3.3	51.2	0.2	21.2	-23.5	-23.8
485	1.5	2.2	-2.1	-1.8	-7.6	-3.7	56.4	0.1	-14.2	-49.8	4.6
486	1.8	-2.0	-4.5	-3.8	-1.5	-3.9	54.2	0.1	1.7	-47.2	-24.8
487	1.1	-2.0	-6.0	-2.4	-5.1	-3.7	52.2	0.1	34.1	-21.0	-20.9
488	-2.6	-2.9	-2.0	-2.5	4.3	-3.4	59.4	0.3	34.2	-24.5	-12.3
489	1.5	0.7	-4.3	-3.5	1.1	-3.4	57.9	0.4	-33.8	-24.2	30.1
490	-3.1	-3.7	-3.0	-2.8	-3.8	-3.2	51.1	0.2	-19.2	-22.7	21.7
491	2.0	-3.0	-1.5	-3.4	-5.8	-3.6	50.6	0.3	0.4	-23.0	16.8
492	2.4	-2.9	-2.3	-0.8	-1.5	-3.0	56.3	0.2	38.6	-40.0	-15.5
493	1.4	2.1	-2.2	-2.4	-6.1	-3.2	52.7	0.4	-15.3	-20.8	34.9
494	-3.2	-2.5	-5.2	-0.5	-7.1	-3.3	58.5	0.3	-19.5	-35.0	1.2
495	0.1	-3.9	-4.7	-1.0	-3.0	-3.1	52.0	0.4	-18.8	-25.3	29.1
496	2.0	1.5	-6.1	-3.9	4.7	-3.7	52.8	0.2	-25.7	-34.5	-13.1
497	-3.5	-1.8	-0.8	-2.1	-5.7	-3.8	59.4	0.3	25.6	-37.8	10.5
498	0.2	3.4	-2.6	-1.0	3.3	-3.5	51.2	0.4	1.8	-13.5	15.6
499	-3.4	-2.1	-1.1	-0.3	-0.8	-3.8	52.8	0.3	9.2	-42.9	-24.5
500	-0.5	1.5	-6.9	-1.3	4.0	-3.1	52.2	0.3	20.1	-32.5	21.9